Ground-penetration radar wave velocities and their uncertainties

Dissertation zur Erlangung des akademischen Grades
"doctor rerum naturalium" (Dr. rer. nat.)

eingereicht als kumulative Arbeit an der
Mathematisch-Naturwissenschaftlichen Fakultät in der
Wissenschaftsdisziplin "Angewandte Geophysik"

Universität Potsdam

Göran Hamann

Golm, 23. Januar 2014

Published online at the
Institutional Repository of the University of Potsdam:
https://doi.org/10.25932/publishup-43680
https://nbn-resolving.org/urn:nbn:de:kobv:517-opus4-436807

Contents

Chapter 1

Introduction

1.1 GPR for environmental research

For matter which is opaque to look into with our eyes (such as subsurface environments), technical devices have to be used to gain information about internal structures and properties. Invasive or destructive methods like excavation, drilling and soil sample analysis can be combined or replaced by non-destructive geophysical methods to establish subsurface site expertises. How we will see in the following, an elegant device is ground penetrating radar (GPR) method, that offers the opportunity to explore near surface environments, fast and secure, with electromagnetic waves with frequencies in the range of MHz (like a radio) to GHz. Thus, GPR is a well established technique to obtain various informations for further studies (e.g., geological, archaeological, mine/cable/pipe/boulder/rock detection, concrete quality screening, environmental remediation evaluation). The approved usage of GPR in glacial and permafrost explorations, for dike monitoring or bathimetric mapping are not the last examples on the list of applications from which our society can profit from this smart technical device. The variety of applications in geotechnics, geoscience, geophysics, civil engineering and environmental science are discussed in literature (e.g., Conyers & Goodman [1997], Vereecken *et al.* [2006], Knödel *et al.* [2006], Allred *et al.* [2008], Annan [2009], Jol [2009a], Miller *et al.* [2010]). According to this literature, GPR is one of the most efficient techniques in near surface geophysics to image lateral and vertical

subsurface structures down to depths of several meters (e.g., sandy soils).
Due to fast data recordings thousands of measurements can be done at one day at thousand different measuring points in survey areas extending over several tenth of square meters. Thus, GPR fills the informational gap between remote sensing, air borne explorations and point measurements like soil probing (Hillel [1998], Butler [2005]). Those mappings can be done with rolling or sliding GPR systems shown in Fig. 1.1.

1.2 Principle of GPR

Maxwell's equations are the general mathematical formalism to calculate the propagation of electromagnetic fields like GPR waves with coupled functions and parameters (e.g., conductivity, dielectric permittivity) Maxwell [1891]. In the high frequency range (MHz to GHz) of GPR, the electrical conductivity (σ) governs wave attenuation, whereas the dielectric permittivity (ε) controls the electromagnetic wave propagation influenced by material properties (e.g., grain size, porosity, water content, mineralogical and chemical composition). The electromagnetic waves velocity in earth materials is in the range between the velocity in water ($\sim$0.033 m/ns) and the velocity in air (i.e., in free space $\sim$0.2998 m/ns). As a detailed discussion of the fundamentals of electrodynamics (e.g., Lehner [2006], Jackson & Fox [1999] and Fliesbach [2008]) is beyond the scope of this thesis, the interested reader is referred to the literature where a number of excellent textbooks discuss the principles of GPR in detail (e.g., Daniels [2004], Butler [2005], Knödel *et al.* [2006] and Jol [2009b]).
A standard cart-mounted GPR system, with a transmitting and receiving antenna and batteries mounted under the cart and a control unit with a screen for direct data visualization is shown in Fig. 1.1. On top of the cart a prism is mounted for position tracking with a laser from a total station (Böniger & Tronicke [2010]). A electronic device (digital video logger) controls the excitation and recording of waves signals of the antennae. Spherical electromagnetic wave pulses (i.e., wave package, wavelet, short temporal variation of energy) are radiated from a transmitter antenna and propagate through the environment. A wave spreading from the antenna will be refracted and reflected by spatial matter variations that

Figure 1.1: A common offset (CO) GPR, with red antennae under the cart, digital video logger with screen in front of the operator and prism for position tracking mounted on top of the cart (standard measurements for bathimetric mapping and sedimentation rate estimation on a frozen lake).

changes direction, velocity, amplitude and frequency content of the moving electromagnetic wave before they are received by the second antenna. The inducted electrical potential in the receiving antenna is recorded by the digital control unit as amplitude during a time (timewindow) of several hundreds of nano seconds after the transmitting antenna was excited. Measurements of time series (traces) at different spatial positions are composed as wiggle plots or images with columns as color-coded amplitudes and a time scale as y-axes and measurement positions as x-axes, formally known as radargram (see e.g., Bjelm *et al.* [1982]). Changes of direction, traveltime, amplitude and frequency content between radiated and received signal gives information about the environment. Objects which are on or above the earth surface (e.g., field workers, fences, data-logger, cables) are also spatial matter variations in terms of electromagnetic wave propagations behavior variations. For example, this was observed during test measurements on a frozen lake (Fig. 1.1) where reflections from a person on the ice surface appeared in the data. Even with shielded antennae problematic reflection patterns from above-surface objects (fences, trees) were observed which interfered with the target signals originating from the subsurface. Thus, GPR data requires a visual data inspections before applying automated data analysis sequences such as those presented in this thesis.

Electromagnetic waves can be approximated as rays with the consequence of infinitesimal wavelength (see optics, seismics), what can be achieved with consistent phase picking of a wave event over different traces recorded with varying antennae positions (see for example Fig. 3.6b)).
Fig. 1.2 illustrates schematically the ray paths of different wave types of two antennae placed on the surface of a stratified ground. The light blue half circles (Fig. 1.2) represents a schematic wavefront emitted by the transmitting antenna. Ray paths and their reflection and refraction points at ground strata interfaces are labeled. Multiple reflections between strata boundaries are not shown. More complete full wave simulations of GPR wave propagation can be done with finite-difference time-domain (FDTD) solution of Maxwell's equations (e.g., Giannopoulos [2005]), but requires extensive computation effort. For this introduction, I used this program to give here an illustration of GPR data gathers of different antenna geometries with synthetic examples (see real data in the following chapters, e.g. Figs. 2.4a, 3.6b and 4.3).

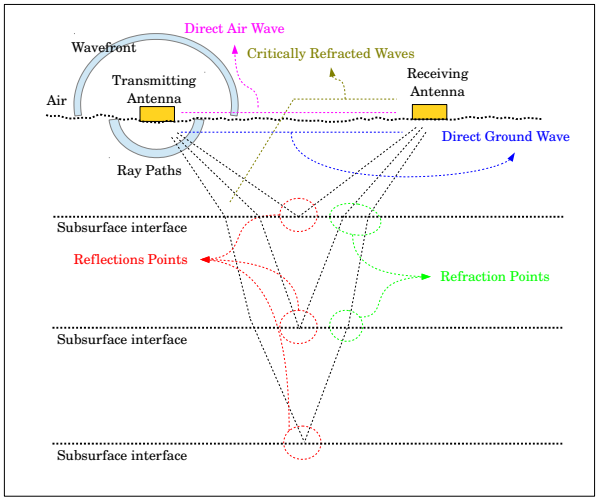

Figure 1.2: Schematic sketch of different wave types (in terms of ray paths) observed in GPR wave propagation in a layered subsurface environment and their reflection and refraction points (only two indicated for simplicity) at the interfaces, with two antennae (yellow) and schematic wavefronts emitted by the transmitting antenna.

1.3 Antenna survey arrangements

From the sens of sight or photography it is known, that a good illumination and different points of view are necessary to see or to obtain nice pictures. This is transferable to GPR measurements, where the number of transmission points, receiving points (i.e., antennae positions) have to be effectively arranged for optimal ray coverage. Therefore different GPR antenna survey geometries are commonly applied. The standard on-ground antenna survey geometries are the common offset (CO) and the common mid point (CMP) methods introduced for example by Annan & Cosway [1992]. Arrangements in boreholes like crosshole geometries are also commonly used (e.g., Olsson *et al.* [1992]). The vertical radar profiling (VRP) technique is a combination of on- and in-ground antenna configuration (e.g., Zhou & Sato [2000]) and is not yet established as standard method. This thesis focuses on data analysis for CMP and VRP antenna survey arrangements. In practice, the most common antenna configuration is the common offset (CO) antennae configuration with one transmitter and one receiver pulled over the ground with constant offset, enabling the recording of waves reflected at bounding layers in the subsurface (see Fig. 1.2). The direct air and ground wave interfere if antennae offset is small (i.e., about one dipole antenna length). Fig. 1.1 shows a conventional CO GPR survey setup during field measurements and the processed data are presented in the appendix (Figs. 2 and 3). Radargrams measured in CO configurations are interpreted in terms of a structural model of the subsurface. One has to consider that for time-to-depth conversion of a radargram the subsurface velocity field has to be known. Thus, the accuracy and reliability of the final structural model depends on the accuracy of the velocity model and methods are needed to explore subsurface velocity variations in detail. To obtain a common mid point (CMP) data gather like in Fig. 1.3, the distance between the antennae is successively increased (see Fig. 1.2). Commonly, subsurface velocities are estimated with CMP surveys with hyperbolic move-out analysis (also known as normal move-out, NMO), what allows the generation of 1D subsurface velocity model (Yilmaz [2001]). Fig. 1.3 shows a synthetic CMP gather recorded across a five layer ground, computed with the program of Giannopoulos [2005]. In Fig. 1.2 we see the direct air wave (cyan), which is the

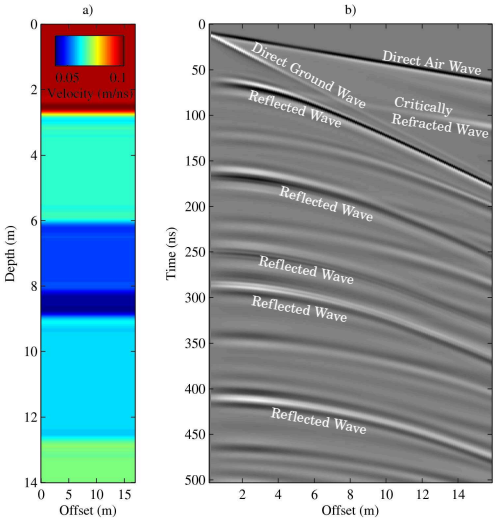

Figure 1.3: Major velocity variations of the subsurface visible in a) correspond to labeled reflection events in FDTD modeled CMP gather b)

fastest (traveling with speed of light) and the direct ground wave (blue). Due to larger and multible offsets we can follow with our eyes the direct air and ground wave in a CMP gather like in Fig. (1.3), in contrast to CO profiles (transferable from Fig. 1.2). Direct air and ground waves appear as linear events in Fig. 1.3. The reflection (black, in Fig. 1.2) of the interface between first and second layer appears as a hyperbole in Fig. 1.3 (first from top). Challenging are the waves reflected at deeper interfaces (refracted black lines in Fig. 1.2) resulting as features which only can be approximated by hyperboles in Fig. 1.3. Waves that are reflected two or more times between deeper layers (multiple reflections) appear also as hyperbola-like features (not labeled in Fig. 1.3). In the second and third chapter of this thesis, CMP gathers are used to introduce new approaches to analyze ground wave velocity and to derive 1D velocity models from reflected events, respectively.

To obtain vertical radar profiling (VRP) data gather like in Fig. 1.5 the transmitting antenna is positioned in a borehole at varying depths and the receiver is located on the earth surface with an offset in the vicinity of the borehole. Vertical radar profile (VRP) is very advantageous due to shorter ray paths and better signal transmission into the ground, in contrast to the previously described on-

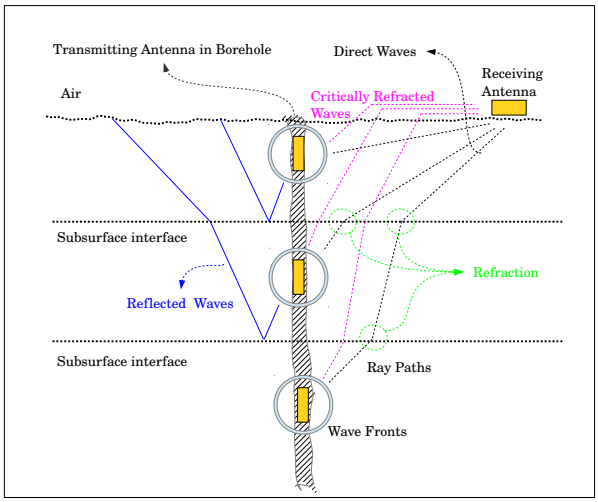

Figure 1.4: Schematic sketch of VRP GPR gather, with one antenna at the earth surface and positions of transmitter in the borehole, schematic wavefront at transmitting antenna, ray paths and reflected, direct and critically refracted waves at ground strata interfaces.

ground antennae arrangements. Fig. 1.4 sketches schematically a VRP antennae arrangement with three depths of the transmitting antenna and with ray paths of direct waves including refraction phenomena denoted by black lines, critically refracted waves as pink lines and reflected waves as blue lines. Fig. 1.5 shows a synthetic FDTD VRP gather for a five layer ground computed with the program of Giannopoulos [2005] and the different wave types are labeled. The multiple reflected wave is not sketched in Fig. 1.4, for simplicity. VRP is also used to derive 1D velocity profiles in the vicinity of a borehole, by inverting the traveltimes of direct arrivals. A global inversion approach of VRP traveltimes is presented in chapter four of this thesis.

1.4 Water content and material parameters from accurate GPR velocities

From comparison of GPR data recorded under changing conditions of soil water content at the same site, we know that GPR is sensitive to soil water content. The explanation for this sensitivity is the dependence of electromagnetic velocity

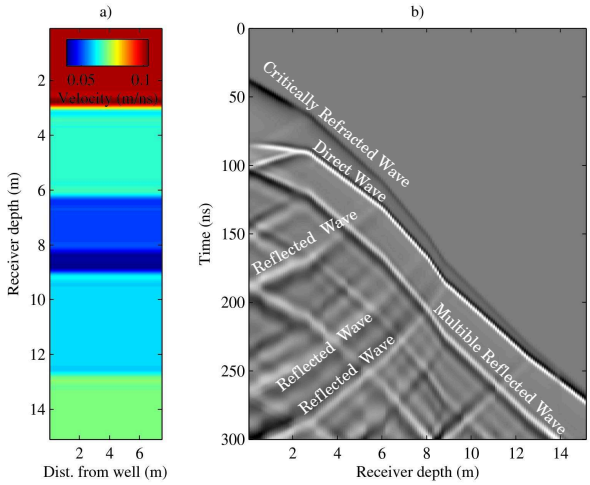

Figure 1.5: Velocity variations visible in ground model a) correspond to labeled wave type events in FDTD modeled VRP gather b)

on soil water content; i.e., slow velocities are observed in wet soil while faster velocities are observed in dry soil. Electrodynamic theory introduces the complex dielectric permittivity ($\varepsilon = \varepsilon' + i\varepsilon''$), where ε' is the real part, ε'' the imaginary part, and $i = \sqrt{-1}$. The first summand ε' expresses the ability of matter to transport electromagnetic waves and the second summand ε'', which have to be small for successful applications of GPR, associates dissipative (stretching, muting) effects of matter to electromagnetic waves. If the second summand converges to zero, a frequency independent effective dielectric permittivity called here the relative permittivity $\varepsilon_r = \varepsilon'/8.854 \times 10^{-12}$ is used.

Under the assumption of low-loss, non-magnetic media, GPR velocities can be converted to relative permittivity values $\varepsilon_r = \frac{c^2}{v^2}$, with c as electromagnetic velocity in free space (e.g., Jol [2009b]).

Then, water content or porosity (i.e. for water saturated soils) can be estimated from relative permittivity values using an appropriate petrophysical translation. A number of different petrophysical models have been proposed in the literature (for a recent review see Steelman & Endres [2011]). In general, petrophysical models are functions following the tendencies between water content values determined from gravimetric soil sampling and relative permittivity values calculated from GPR or time domain reflectometry (TDR) measurements. Different authors use different functions for different soils, to optimize the accordance of

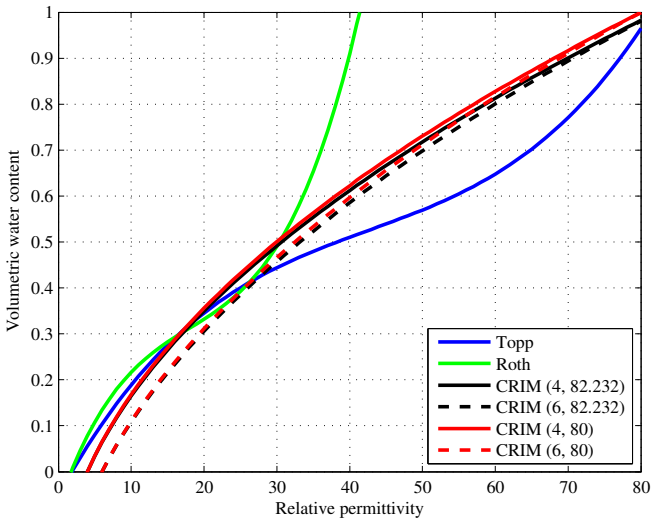

Figure 1.6: Two polynomial functions (Topp, Roth) and the complex refractive index model (CRIM) with variable permittivities of dry soil (4,6) and water (82.232, 80) as examples of petrophysical models to translate permittivities into volumetric water content.

petrophysical laws to observations (e.g., Knight & Endres [2005], Knoll [1996]). The most commonly used empirical relationship to estimate volumetric water content in the water-saturated zone (i.e., porosity) are the equation of Topp *et al.* [1980]; equation 1.1) and the complex refractive index model (CRIM; Wharton & Best [1980]; equation 1.2), which is a volumetric mixing model. Like Topp, other authors (e.g., Roth *et al.* [1992]) used also third order polynomials (like equation 1.1) with other coefficients to explain petrophysical relationships. Topp's equation gives the volumetric water content as

$$\Phi = 5.3 \times 10^{-2} + 2.92 \times 10^{-2}\varepsilon - 5.5^{-4}\varepsilon^2 + 4.3^{-6}\varepsilon^3. \tag{1.1}$$

The CRIM mixes volumetric the permittivity of dry soil ε_r^m and permittivity of water ε_r^w to calculate the volumetric water content as

$$\Phi = \frac{\sqrt{\varepsilon_r - \varepsilon_r^m}}{\varepsilon_r^w + \varepsilon_r^m}. \tag{1.2}$$

Fig. 1.6 shows examples of empirical relationships between relative permittivity (ε_r) and volumetric water content (Φ) as two polynomial functions (Topp, Roth;

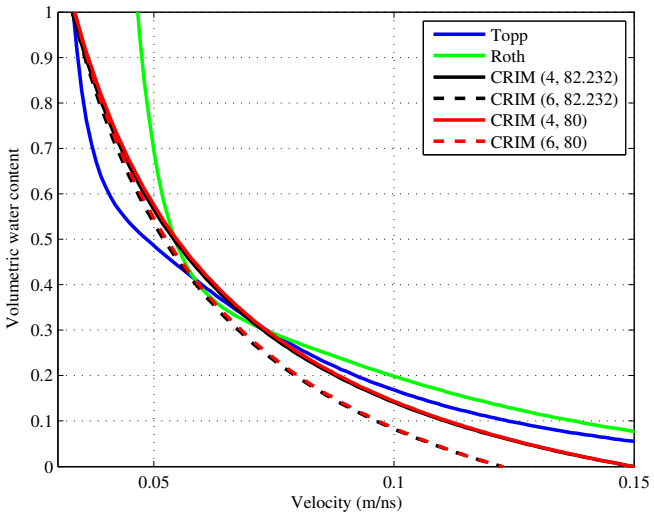

Figure 1.7: Exemplary illustration of the varying petrophysical relations to convert GPR velocities into volumetric water content, with two examples of polynomial laws (Topp, Roth) and CRIM with permittivities of dry soil (4,6) and water (82.232, 80).

equation 1.1) and a volumetric mixing model (CRIM; equation 1.2) with permittivities of dry soil (4,6) and water (82.232, 80). Fig. 1.7 shows the corresponding empirical translations from GPR velocities (v) into volumetric water content (Φ), using $v = \sqrt{\frac{c^2}{\varepsilon_r}}$ and the polynomial laws (Topp, Roth; equation 1.1) and the complex refractive index method (CRIM; equation 1.2). More advanced effective medium theory, have to be enhanced, regarding soil texture matrix, such as grain size, shape and orientation, with methods that interconnect micro quantities to bulk quantities (e.g., Sen [1984]).

1.5 Research question

The general question of this work is: Are there quantitative and reproducible approaches to get GPR wave velocities including uncertainties, to determine accurate depths and material parameters?
Due to the fact that measurements from GPR give only information in form of distorted images of subsurface structures those images have to be combined and compared with additional information from boreholes or excavations, to achieve correct length-scales (e.g., layer thickness) or soil parameters (e.g., water content,

grain size) over finite volumes. Thus, the following chapters will demonstrate that there are other possibilities to analyze GPR data from CMP and VRP data gathers, with a minimum of additional a-priori informations. Velocity results of those methods will be improved with other data such as existing GPR data analysis strategies and other more reliable data like time-domain reflectometry (TDR) and borehole logging data.

1.6 Thesis content

In the second chapter I develop a new direct ground wave velocity analysis approach based on linear moveout spectra to find the optimum ground wave velocity including uncertainties from multi-offset data gathers. I use synthetic data to illustrate the principles of the method and to investigate uncertainties in ground wave velocity estimates. To demonstrate the applicability of the approach to real data, I analyze GPR data sets recorded at field sites in Canada over an annual cycle from Steelman & Endres [2010]. My results obtained by this efficient and largely automated procedure agree well with the manual achieved results of Steelman & Endres [2010], derived by a more laborious largely manual analysis strategy.

In the third chapter I develop a new methodology to invert reflection traveltimes with a global optimization approach as an alternative to conventional spectral NMO-based velocity analysis (e.g., Greaves *et al.* [1996]). For global optimization, I use particle swarm optimization (PSO; Kennedy & Eberhart [1995]) in the combination with a fast eikonal solver as forward solver (Sethian [1996]; Fomel [1997a]; Sethian & Popovici [1999]). This methodology allows me to generate reliability CMP derived models of subsurface velocities and water content including uncertainties. I test this method with synthetic data to study the behavior of the PSO algorithm. Afterward, I use this method to analyze my field data from a well constrained test site in Horstwalde, Germany. The achieved velocity models from field data showed good agreement to borehole logging and direct-push data (Schmelzbach *et al.* [2011]) at the same site position.

For the fourth chapter I implement a global optimization approach also based on

PSO to invert direct-arrival traveltimes of VRP data to obtain high resolution 1D velocity models including quantitative estimates of uncertainty. My intensive tests with several traveltime data sets helped to understand the behavior of PSO algorithm for inversion. Integration of the velocity model to VRP reflection imaging and attenuation model improved the potential of VRP surveying. Using field data, I examine this novel analysis strategy for the development of petrophysical models and the linking between my GPR borehole and other logging data to surface GPR reflection data.

Chapter 2

Spectral velocity analysis for determination of ground wave velocities and their uncertainties in multi-offset GPR data

Göran Hamann, Jens Tronicke, Colby M. Steelman and Anthony L. Endres
Near Surface Geophysics, 2013, 11, 167-176

2.1 Abstract

In many hydrological applications, ground wave velocity measurements are increasingly used to map and monitor shallow soil water content. In this study, we propose an automated spectral velocity analysis method to determine the direct ground wave (DGW) velocity from common midpoint (CMP) or multi-offset ground-penetrating radar (GPR) data. The method introduced in this paper is a variation of the well-known spectral velocity analysis for seismic and GPR reflection events where velocity spectra are computed using different coherency measures along hyperbolas following the normal moveout model. Here, the unnormalized crosscorrelation is computed between waveforms across data gathers which are corrected with a linear moveout equation using a predefined range of

velocities. Peaks in the resulting velocity spectra identify linear events in the GPR data gathers like DGW events and allow for estimating the corresponding velocities. In addition to obtaining a DGW velocity measurement, we propose a robust method to estimate the associated velocity uncertainties based on the width of the peak in the calculated velocity spectrum. Our proposed method is tested on synthetic data examples to evaluate the influence of subsurface velocity, surveying geometry, and signal frequency on the accuracy of estimated ground wave velocities and subsequent soil water content estimates based on an established petrophysical relationship. Furthermore, we apply our approach to analyze field data, which have been collected across a test site in Canada to monitor a wide range of seasonal soil moisture variations. A comparison between our spectral velocity estimates and results derived from manually picked ground-wave arrivals shows good agreement, which illustrates that our spectral velocity analysis is a feasible tool to analyze DGW arrivals in multi-offset GPR data gathers in an objective and more automated manner.

2.2 Introduction

Many hydrological applications require detailed information about spatial and temporal variations of soil water content, which is controlled by soil composition, precipitation, evaporation, and temperature. Typical field techniques, such as gravimetric sampling, time-domain reflectometry (TDR) and neutron probing Hillel [1998], are point measurement techniques, and thus, are not efficient to investigate soil water content and its variability at the field scale. On the other hand, remote sensing approaches often do not provide the spatial resolution required for a detailed understanding of near-surface hydrological processes, especially in catchments characterized by heterogeneous soil conditions. Geophysical techniques including different GPR methodologies (Huisman *et al.* [2003]) have been shown to be more efficient at monitoring soil water content at the field scale. As such, GPR soil moisture monitoring techniques close the scaling gap between point measurements and remote sensing technologies (e.g., Vereecken *et al.* [2006]; Allred *et al.* [2008]).

When using GPR to estimate soil water content, we typically analyze variations in

the propagation velocity of GPR waves because the amount of water in a porous medium strongly controls the electromagnetic wave velocity. To determine subsurface velocity variations, different GPR surveying approaches including cross-hole tomography (e.g., Binley *et al.* [2001]), multi-offset reflection profiling (e.g., Greaves *et al.* [1996]; Brosten *et al.* [2009]; Turesson [2007]; Booth *et al.* [2010]), and direct ground wave (DGW) velocity surveying (e.g., Galagedara *et al.* [2005a]; Huisman *et al.* [2001]; Huisman *et al.* [2003]) can be used. DGW velocity surveying employing either constant or multi-offset acquisition techniques focus on integrative velocity estimation within the upper half meter of soil. For overview about penetration depth estimation by different models of DGW for GPR data the reader is referred to literature Grote *et al.* [2010]. In such surveys, the DGW velocity is usually determined by analyzing their manually determined arrival times. The translation of GPR velocities into soil water content is typically a two-step procedure. First, GPR velocities are converted to dielectric permittivities assuming low loss media (i.e., permittivities are calculated by squaring the ratio between speed of light and GPR velocity). Then, permittivities are translated into soil water content using an appropriate petrophysical model. Different models have been proposed in the literature (Steelman & Endres [2011]) and the most popular ones rely on empirical relations or mixing models. It should be noted that these relationships are generally non-linear. For example, the popular Topp equation is a third order polynomial derived from laboratory measurements (Topp *et al.* [1980]). From a practical point of view, site-specific calibration data should be taken into account to check the applicability of a certain model or for developing site-specific relations and, thus, to minimize uncertainties when translating velocities into water content (e.g., Heimovaara *et al.* [1994]; Steelman & Endres [2011]).

Another source of uncertainty, which is difficult to quantify and often ignored, arises from the straight-forward procedure of direct ground wave velocity determination. For example, in multi-offset or common midpoint (CMP) data gathers, DGW velocities are usually determined by fitting a straight line through the interpreted ground wave arrivals (e.g., Greaves *et al.* [1996]; Huisman *et al.* [2003]). However, the procedure of picking DGW arrival times and fitting a linear model are often performed in a manual fashion and, thus, this procedure is rather

subjective, often not reproducible, and provides no information on the inherent uncertainties. These uncertainties can be related to survey geometry (i.e., minimum and maximum offsets as well as trace spacing), frequency content of the data, complexity of the recorded wavefield and the subsurface velocity structure, data quality, and subjective interpretations. Another source of uncertainties are interference phenomena of direct ground wave events with shallow reflected, lateral, critically refracted and air wave events, as demonstrated with field data by Grote *et al.* [2010] and Steelman & Endres [2010], and model simulations by Galagedara *et al.* [2005b] and Yi & Endres [2006]. Thus, we beware of understanding the introduced method as over all solution for analyzing every ground wave CMP GPR data without looking on it, especially in extraordinary cases like dispersive media van der Kruk *et al.* [2009]).

In this study, we propose a DGW velocity analysis approach based on velocity spectra calculated using a linear moveout model. In addition to finding an optimum ground wave velocity from multi-offset data gathers, our method can be used to estimate the associated uncertainties. After introducing the methodological background, we use simple synthetic data to illustrate the principles of our method and investigate uncertainties in ground wave velocity estimates, including their impact on derived values of soil water content for different surveying geometries and antenna frequencies. To demonstrate the applicability of our approach to real data, we analyze GPR data sets collected at field site in Canada monitoring seasonal variations in soil water content across a wide range of nature soil moisture dynamics Steelman & Endres [2010]. Given that these field data show significant variations in DGW response using different antenna frequencies (i.e., 225, 450 and 900 MHz), and have been previously interpreted using a conventional manual analysis, these data represent an excellent opportunity to validate our spectral velocity analysis approach.

2.3 Methodology

Velocity spectra are standard tools in reflection seismic and GPR surveying to extract velocity information from reflected events observed in CMP data gathers (Yilmaz [2001];Annan [2005]). Here, normal moveout (NMO) based analyses

are used to test different predefined velocity values. The final velocity spectrum is calculated using different measures of coherency across the data gather in a predefined time window centered on hyperbolic trajectories modeled with the NMO equation. The optimum stacking or root-mean square (RMS) velocities are then selected by analyzing the maxima in the resulting velocity spectrum (i.e., calculated coherency values as a function of tested velocities and traveltime) corresponding to primary reflection events in the analyzed CMP gather, how it was done by Booth *et al.* [2011] for hyperbolic events in GPR CMP data, including Monte Carlo simulation based velocity precision establishment. However, we implement a linear moveout (LMO) model using a spectral velocity analysis approach to describe the linear dependency of direct ground wave arrival times t_d on antenna offset x in a medium characterized by a constant velocity v:

$$t_d = \frac{x}{v} \tag{2.1}$$

To calculate the velocity spectrum, we use the unnormalized crosscorrelation CC as measure of coherency. Following Yilmaz [2001], CC is calculated by:

$$CC = \frac{1}{2} \sum_t \left\{ \left(\sum_{i=1}^{M} f_{i,t(i)} \right)^2 - \sum_{i=1}^{M} f_{i,t(i)}^2 \right\} \tag{2.2}$$

$f_{i,t(i)}$ is the amplitude of the i-th trace at time $t(i)$ and M is the number of traces in the analyzed data gather. Using equation (2.1), $t(i)$ is calculated for each trace at a predefined velocity. The outer summation encompasses the time samples within a pre-defined time gate. The edges of this correlation gate are tapered using a Hamming window and the length of the gate is chosen to be in the range of the wavelet period (comparable to NMO based analyses; Sheriff & Geldart [1999]). This procedure is repeated for each time sample and a user specified testing velocities resulting in CC as a matrix depending on time and velocity. In the resulting velocity spectrum, peak values indicate optimum velocities describing the corresponding linear events in the analyzed CMP gather. Sharp maxima are associated with well-defined velocity values, while smeared and flat maxima indicate that a range of tested velocities similarly fit the data. The shape of those

maxima is governed by the fitting quality of the applied moveout function to the actual trajectory but is also influenced by wavelet shape, which is disturbed by noise and other interference with other events not corresponding to the applied moveout (e. g. NMO moveout shows smeared maxima for linear events and LMO moveout shows smeared maxima hyperbolic events). This observation offers the opportunity to derive velocity uncertainties from the calculated map of CC values and to evaluate different factors influencing uncertainty. This implies that CC has enough elements in the velocity dimension to resolve different shapes of maxima and not only maxima as pixels in the spectra. We measure the width of the maxima at 90 % of the observed peak CC value and define the corresponding velocity range to quantify the uncertainties. This measure of uncertainty has been chosen to achieve reasonable water content errors as maximal limit. Thus errors can be minimized by reducing this threshold, what is a case specific decision, respecting data quality, prevalent velocity range, water content and water content model.

2.4 Synthetic examples

To further illustrate our approach, we generated synthetic CMP gathers using time-shifted Ricker wavelets with a centre frequency of 450 Hz (Fig. 2.1a); this synthetic example is calculated using a spatial and temporal sampling of 0.02 m and 0.1 ns, respectively. The offset range is limited to 0.3 m to 1.5 m. The synthetic data gather shows two linear events with velocities of 0.1 m/ns and 0.3 m/ns simulating direct ground and air wave arrivals, respectively. Fig. 2.1b illustrates the result of our LMO based velocity analysis. Maximum CC values are found around 0.1 m/ns and 0.3 m/ns corresponding to the velocities of the two linear events in Fig. 2.1a. Furthermore, we see that the CC maximum associated with the steep ground wave event (0.1 m/ns) is significantly sharper compared to the maximum associated with the relatively flat air wave event (0.3 m/ns). Using the defined uncertainty criterion (90% of the peak CC values associated with the velocity of a certain event), we obtained a velocity error of $\sim$0.006 m/ns and 0.05 m/ns for the ground and air wave velocity, respectively. From this simple example, we found that the velocity step size used in the analysis should be suf-

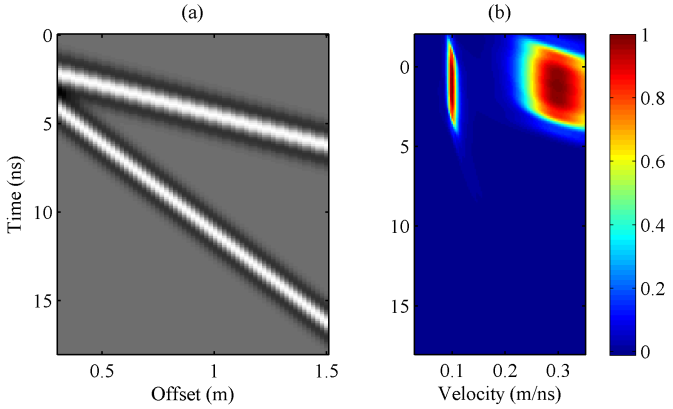

Figure 2.1: (a) Synthetic 450 MHz CMP gather with two linear events simulating direct ground and air wave arrivals. (b) Corresponding velocity spectrum calculated using our LMO based velocity analysis approach. In (b), the correct velocity values of 0.1 m/ns and 0.3 m/ns are indicated by maximum *CC* values.

ficiently small (<10-4 m/ns) to adequately sample the shape of the maxima and, thus, to reliably estimate the uncertainty. If velocity step size is too large (e.g., 5 velocities) no differences of errors will be detected because the 90% threshold has the size of a velocity step (fifths of velocity range) for any velocity. In Fig.2.1b the lower velocity is sampled with a view velocity steps (∼5), and the corresponding error resulting from the threshold of 90% maximum width of this peak is one velocity sample, consequently lower velocity errors are equal and no error behavior is detectable. Thus velocity range has to be sufficiently sampled to see the shape of maxima in the spectra even when they are very thin and sharp, especially in the case of low velocities. Furthermore, Fig. 2.1 indicates that for a given CMP survey geometry (defined by the trace spacing as well as the minimum and maximum offset within a data gather) the uncertainty of the velocity estimate depends on the steepness (i.e., velocity) of the analyzed direct event. To systematically analyze ground wave velocity uncertainties and the influence of subsurface velocity, data frequency and surveying geometry, we have generated a variety of synthetic CMP gathers (comparable to Fig. 2.1a) and have analyzed these gathers using our spectral velocity analysis technique. Using the procedure outlined above, we have determined the best-fitting velocity including an estimate of uncertainty (absolute and relative error) for each synthetic CMP gather. Furthermore, we have investigated the impact of this velocity error on water content

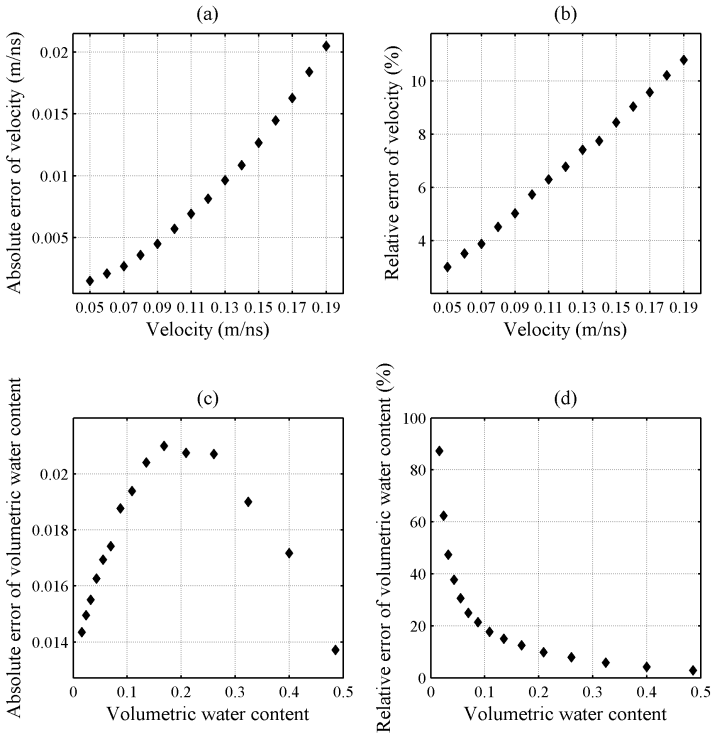

Figure 2.2: Errors derived from analyzing synthetic CMP gathers generated using a fixed wavelet frequency (450 MHz), a fixed maximum offset (1.5 m), a fixed antenna step-size increment (0.01 m) and varying DGW velocities between 0.05 m/ns and 0.2 m/ns. (a) Absolute, (b) relative error of velocity, (c) absolute, and (d) relative error of derived water content values.

estimates derived from ground wave velocities using a standard two-step transformation. Here, we assume low loss media and the validity of Topp's equation (Topp et al. 1980) to compute the range of water contents corresponding to the velocity values derived from our above defined uncertainty criterion. Fig.2.2 illustrates the results of this procedure for synthetic CMP gathers generated using a fixed wavelet frequency (450 MHz), a fixed offset range (0.3 m to 1.5 m), a fixed trace spacing interval (0.02 m), and DGW velocities varying between 0.05 m/ns and 0.2 m/ns. Fig.2.2a shows the absolute velocity errors derived from the velocity spectra, while Fig.2.2b shows the corresponding relative errors. These plots illustrate increasing uncertainty with increasing DGW velocity and demonstrate that the relative errors show a linear dependency on velocity. In Fig.2.2c and Fig. 2.2d, we show the absolute and relative errors of water content. While the abso-

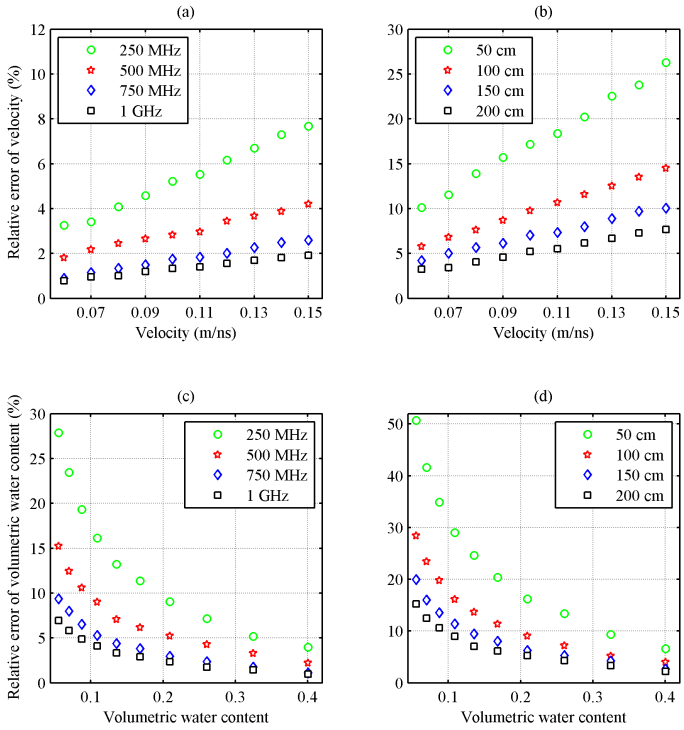

Figure 2.3: Relative errors in velocity derived from analyzing synthetic CMP gathers generated (a) using a fixed survey geometry (maximum offset 2.0 m, trace spacing 0.01 m) and four different wavelet frequencies, and (b) using a fixed frequency (250 MHz), a fixed antenna step-size increment (0.01 m) and four different maximum offsets. (c) Relative errors of water content derived from relative velocity errors shown in (a). (d) Relative errors of water content derived from relative velocity errors shown in (b).

lute error in water content shows a clear maximum around 0.2, the relative error shows an exponential-like decrease with increasing velocity. These observations are related to the non-linear, two-step procedure used to calculate water content from DGW velocity measurements. The offset range is chosen for this example, because it will reveal in the field data example to be sufficient for reasonable results and reduces measuring effort.

We also systematically investigated the influence of varying survey parameters on the accuracy of DGW velocity estimates. In Fig.2.3a, we illustrate the influence of wavelet frequency on the accuracy of derived ground wave velocity values (relative error) using a fixed survey geometry with an antenna offset range 0.3 m to 2.0 m and trace spacing interval of 0.02 m. Again, subsurface velocities are varied between 0.05 m/ns and 0.2 m/ns while wavelet frequency is varied between

250 MHz and 1 GHz. For each frequency, the relative errors are smaller due to lower velocities following a linear relation (comparable to Fig.2.2b). Furthermore, we observe a clear dependency on wavelet frequency, whereby smaller uncertainties result from higher wavelet frequencies. The influence of the maximum offset recorded in a CMP gather on the relative velocity error is illustrated in Fig.2.3b. Here, a fixed wavelet frequency of 250 MHz and a fixed trace spacing of 0.02 m have been used, while the maximum offsets considered for velocity analysis are varied between 0.5 m and 2.0 m. Comparable to Fig.2.3a, a linear decrease in the relative velocity errors with decreasing subsurface velocities is observed for each maximum offset. Furthermore, increasing the maximum offset will decreases the relative error in measured DGW velocity. Figures 2.3c and 2.3d illustrate the corresponding relative errors in water content showing an exponential-like decrease with increasing velocity for all frequencies and maximum offsets, respectively (comparable to Fig. 2.2d). Similar tendencies for velocity precision for NMO analysis for reflected events were described by Booth *et al.* [2011]. In Fig. 2.3c, we observe increasing errors with decreasing frequency, while in Fig. 2.3d we see that increasing the maximum offset resulted in decreased relative errors in water content.

2.5 Field data examples

To evaluate the applicability of our method to real data, LMO based velocity spectra are computed for CMP data gathers collected at a field site near Woodstock, Ontario, Canada (Steelman & Endres [2010]). Core and borehole data collected at the site shows that the upper 0.5 to 0.7 m is composed of silt loam soil with a water table that varies between 2 m and 3 m below ground surface (Steelman & Endres [2010]). CMP data were recorded between May 2006 and September 2007 with intervals on the order of a few weeks to analyze seasonal variations in soil moisture. During this time period, precipitation, freezing and melting events caused major variations in soil conditions and, thus, the GPR data are well suited to performed in an automated fashion.
Using three different frequencies (225 MHz, 450 MHz, 900 MHz), the data sets were recorded with a total time window of 100 ns, a sampling interval of 0.1 ns,

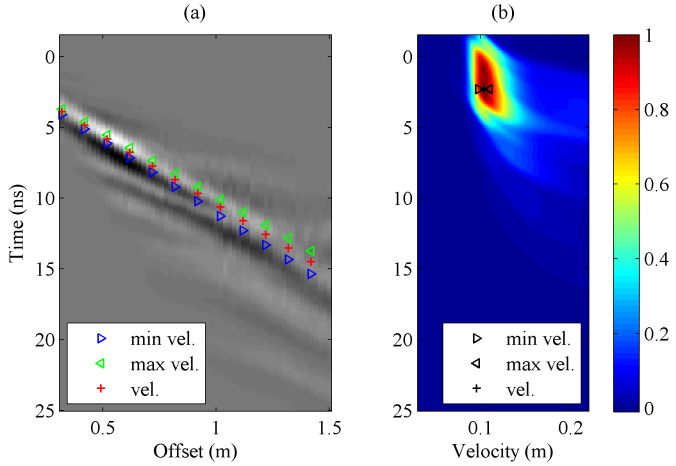

Figure 2.4: (a) Example of pre-processed 450 MHz CMP gather recorded on May 25, 2007 and (b) the velocity spectrum resulting from LMO based velocity analysis. In (b) the crosses identify the best-fit velocity while the triangles indicate estimated velocity uncertainties (i.e., minimum and maximum velocities). In (a) the same symbols are used to illustrate the slope of the corresponding linear events.

and 64 stacks per trace. CMP offsets range between 0.3 and 3.0 m, 0.2 and 2.5 m, and 0.2 and 2.0 m for the 225, 450, and 900 MHz data, respectively, with an antenna step-size of 0.02 m for all data sets. In this study, we limit the maximum offset to 1.5 m to improve the quality of the computed velocity spectra (i.e., avoid potential interference with shallow reflections that may smear out peaks in the spectrum). Pre-processing of the CMP data includes zero-time correction. It should be noted that this correction does not alter the results of LMO based velocity analysis. Then, we apply a dewow and a low-pass filter (using a cutoff-frequency of about four times the antenna working frequency) to suppress low and high-frequency noise. To attenuate unwanted events (such as shallow reflections) the data gathers are muted using a cone shaped muting window. Considering the first arrivals and the frequency content of the data, this window is designed to focus on DGW events with typically observed velocities ($\sim$0.05 m/ns to $\sim$0.2 m/ns). Furthermore, an offset-dependent amplitude scaling is applied to balance the amplitudes over the analyzed offset range. After applying this pre-processing sequence (an example of a pre-processed CMP gather is illustrated in Fig. 2.4a), we calculate velocity spectra using our LMO based approach. Three hundred equally spaced velocity values ranging from 0.04 m/ns to 0.22 m/ns are tested in the spectral velocity analysis procedure. Comparable

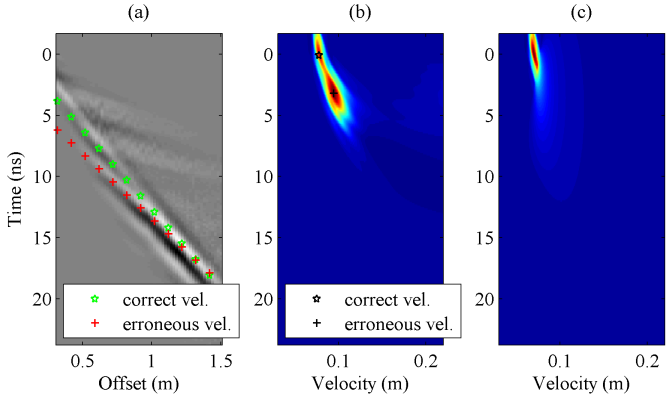

Figure 2.5: (a) Example of pre-processed 900 MHz CMP gather recorded on October 22, 2006, (b) the velocity spectrum resulting from LMO based velocity analysis, and (c) the same as (b) after identifying and isolating the corresponding DGW event. In (b) the symbols identify two local maxima corresponding to the linear DGW event (star) and an interference event mainly associated with a strong shallow reflection (cross). In (a) the same symbols are used to illustrate the slope of the corresponding linear events.

to the synthetic examples, maxima in the spectra are interpreted as optimum velocities, while uncertainties are estimated from the velocities measured at 90% of the peak CC value. In Fig. 2.4b, we illustrate the outcome of this analysis using the example CMP gather shown in Fig. 2.4a where we also overlay direct ground wave arrivals calculated using the derived best fit velocity value and its estimated uncertainty. In this example, the maximum in the calculated spectrum is well defined, although some interference phenomena of the ground wave arrivals with a shallow reflection event are visible around 1 m offset. For such data gathers where the ground wave arrivals are well defined by an isolated maximum in the corresponding velocity spectrum, the entire analysis can be performed in an automated fashion.

In Fig. 2.5, we illustrate a second example of a pre-processed CMP gather including the results of spectral velocity analysis. In this example, interference of the DGW event with a strong shallow reflection event is obvious (Fig. 2.5a), resulting in two local maxima in the corresponding velocity spectrum (Fig. 2.5b). In such cases, the user must select and isolate the maximum CC value corresponding to the ground wave event (Fig. 2.5c) to avoid erroneous DGW velocity and uncertainty estimates. In the Woodstock data, such phenomena are evident and related to highly dynamic freezing and thawing events (Steelman & Endres [2009]; Steelman & Endres [2010]). The two examples (Figs. 2.4 and 2.5) illustrate that

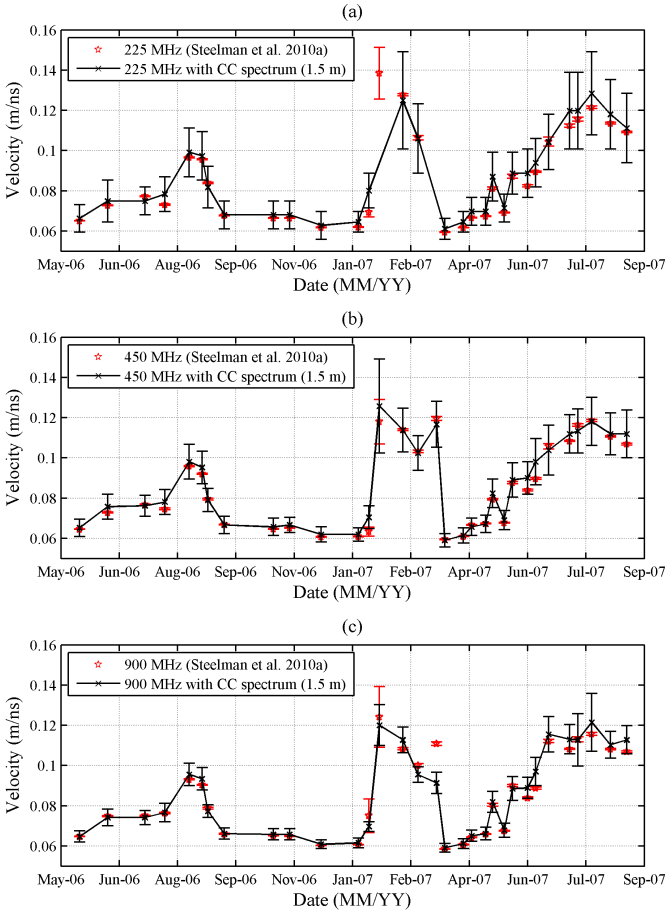

Figure 2.6: Field example illustrating temporal variations in DGW velocity between May 2006 and September 2007 for GPR data recorded using (a) 225 MHz, (b) 450 MHz and (c) 900 MHz antennae. The red symbols identify the best-fit velocities and error bounds derived from manual picks of DGW arrival times, while the black symbols identify the corresponding values derived from LMO based spectral velocity analysis. CMP data recorded on January 31, 2007 did not show any clear maximum in the velocity spectrum and, thus, are excluded from further analyses.

under favorable conditions (clear ground wave events, i.e., no dispersion or interferences) the proposed method can be implemented in a largely automated fashion. However, a re-examination of the results, especially in the presence of strong interference phenomena, is advisable to ensure that the spectral maxima corresponding to DGW arrivals are appropriately identified.

Using the procedure outlined above, we have analyzed all available CMP gathers collected at the Woodstock field site. In Fig. 2.6a, Fig. 2.6b, and Fig. 2.6c, we show the results as time series for the 225 MHz, 450 MHz, and 900 MHz antennae, respectively. Furthermore, we compare the DGW velocities and uncertainties de-

rived from spectral velocity analysis (black symbols) with the results obtained by Steelman & Endres [2010] based on a manual linear least squares traveltime picking analysis including standard errors (red symbols). In such a manual analysis, the user specifies the optimum offset range for each individual CMP gather to obtain an optimum result. When comparing the results, we see that both analysis methods show the same time-dependent trends for all frequencies; for example, the effects of soil freezing (increasing velocities) and thawing (decreasing velocities) during winter 2007 or the increasing velocities during spring and summer 2007. Furthermore, the derived velocity values are in good agreement for all analyzed frequencies; however, some discrepancies are observed in late January and early February 2007 (data point from our method is ejected). Such discrepancies might be related to relatively thin layers developing during freezing and thawing events that could lead to ambiguous or dispersive ground wave arrivals (e.g., van der Kruk *et al.* [2009]). In addition, we notice that the estimated uncertainties are significantly larger for the error bars derived from velocity spectra compared to those resulting from least squares fitting of manually picked arrival times. In addition to the conceptual differences between the two analysis methods, the different offset ranges used for the analyses may also be considered to explain these differences in uncertainty estimates. While a fixed offset range (0.3 m to 1.5 m) is used to calculate the velocity spectra, a user-specified optimum window has been subjectively identified for each individual CMP gather during manual analyses. Thus subsurface heterogeneities might have different influences on the derived velocity values and uncertainties. Finally, we interpret the uncertainties from the spectral analyses as upper 'conservative' error bars, and the uncertainties from manual analyses as optimum 'idealized' error bounds and conclude that the velocity spectra are powerful tool to analyze large data sets in an objective and time efficient manner.

To further analyze and evaluate the uncertainties estimated from the velocity spectra, we now compare the estimates from field data to estimates derived from synthetic examples. In Fig. 2.7, we plot the relative velocity error versus the derived best matching velocity value for all CMP gathers (Figs. 2.6a-c). In Fig. 2.7, we show data points from synthetic examples (comparable to Fig. 2.3), which have been computed using the offset range and data frequency content of our field

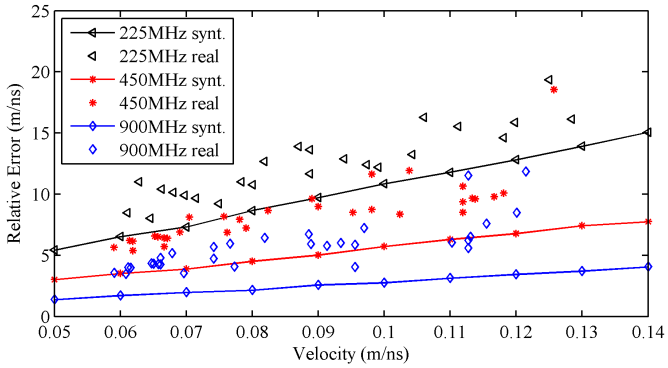

Figure 2.7: Comparison of relative uncertainties of velocities derived from field experiments (Fig. 2.6ac) to uncertainties derived from synthetic CMP calculated using the same dominant frequencies and offset ranges.

examples. Although some discrepancies are visible (due to noise, subsurface heterogeneities, data scaling), the observed trends (increasing error with increasing velocity) and magnitude of the uncertainties are comparable for all frequencies. In Fig. 2.8 we show the results for water content derived with the Topp's equation from the time series of the DGW velocities shown in Fig. 2.6a-c. In Fig. 2.9

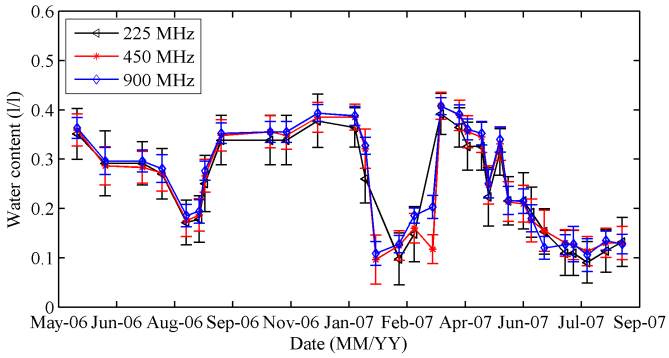

Figure 2.8: Temporal water content and uncertainties variation derived with Topp's equation from the velocities of the field examples from Fig. 2.6(ac), between May 2006 and September 2007.

we compare the uncertainty behaviour of the relative water content of all data points from Fig. 2.8 with synthetic results generated with the same frequencies and offset ranges. Water content uncertainties from real data follow the trend of the synthetic values (see Fig. 2.3). Uncertainties increase with decreasing water content but are <30% for water contents >0.15 l/l. These uncertainties can again be regarded as an upper limit and absolute values may change when choosing a

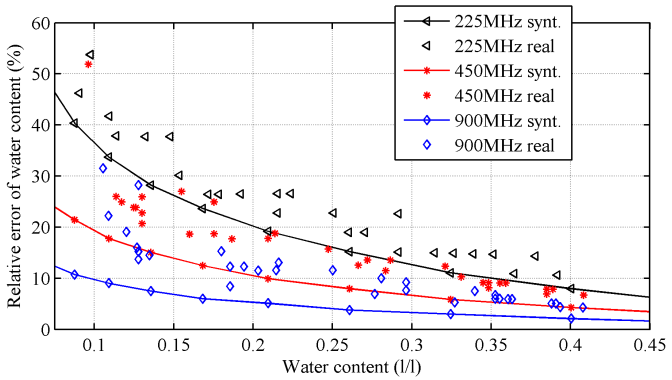

Figure 2.9: Comparison of relative uncertainties of water content derived from the field examples (Fig. 2.6a-c) with Topp's equation to uncertainties derived from synthetic CMP data similar to Figs 2.2 and 2.3 by using the dominant frequencies and offset ranges from field examples.

different threshold for measuring velocity uncertainties. These results readily illustrate the overall applicability of our spectral velocity analysis approach to measuring DGW velocities from multi-offset GPR data sets.

2.6 Conclusions

A LMO based spectral velocity analysis method has been proposed to estimate DGW velocities from multi-offset GPR data. In contrast to common practice, which is largely based on manually fitting DGW arrivals, our method allows a more objective and reproducible analysis of DGW velocity. Furthermore, it can be used to quantify uncertainties in determining DGW velocities by measuring the width of the maxima in the calculated velocity spectra. This allows us to analyze uncertainties related to survey design and subsurface conditions in a systematic manner.

The shown synthetic examples have demonstrated that the accuracy of DGW velocity determination depends on the true subsurface velocity, the antenna frequency, and the survey geometry (offset range and maximum offset used in the analysis). For typical surveying parameters and signal frequencies, our examples demonstrate that relative errors in velocities can be greater than 5%. These findings have important implications for survey design and might be critical when DGW velocities are translated into water content. Assuming low loss soil con-

ditions where Topp's equation is valid, our synthetic studies have demonstrated that the relative error in water content increases exponentially with decreasing water content. To demonstrate the applicability of our approach to real data, LMO based velocity spectra have been calculated for field data collected across a silt loam soil at a well-constrained field site in Canada. We found that when using a well-adapted pre-processing sequence the spectral velocity analyses can be performed in a largely automated manner, thus, allowing us to effectively analyze large data sets in an efficient manner. Comparing our results to a detailed manual analysis of the available CMP gathers illustrates that the detected velocity values and seasonal variations largely coincide. As the influence of the interpreter is minimized, we believe that spectral velocity analysis is a rather objective tool to derive and analyze DGW velocities including the associated uncertainties. This point is supported by a comparison of uncertainties derived from spectral analyses of field data to those of synthetic data gathers where we found comparable behavior under varying ground velocity conditions, antennae frequency measurements, and antenna offset ranges. Thus, we believe that LMO based spectral velocity analysis is a feasible tool to derive ground wave velocities from CMP data, and would be a valuable method in the analysis of multi-offset GPR data collected with modern multi-channel GPR systems.

Chapter 3

Global inversion of GPR traveltimes to assess uncertainties in CMP velocity models

Göran Hamann and Jens Tronicke accepted: Near Surface Geophysics, 2013

3.1 Abstract

Velocity models are essential to process two- and three-dimensional ground- penetrating radar (GPR) data. Furthermore, velocity information aids the interpretation of such data sets because velocity variations reflect important material properties such as water content. In many GPR applications, common midpoint (CMP) surveys are routinely collected to determine one-dimensional velocity models at selected locations. To analyze CMP data gathers, spectral velocity analyzes relying on the normal-moveout (NMO) model are commonly employed. Using Dix's formula, the derived NMO velocities can be further converted to interval velocities which are needed for processing and interpretation. Because of the inherent assumptions and limitations of such approaches, we investigate and propose an alternative procedure based on the global inversion of reflection travel-

times. We use a finite-difference solver of the Eikonal equation to accurately solve the forward problem in combination with particle swarm optimization (PSO) to find one-dimensional GPR velocity models explaining our data. Because PSO is a robust and efficient global optimization tool, our inversion approach includes generating an ensemble of representative solutions that allows us to analyze uncertainties in the model space. Using synthetic data examples, we test and evaluate our inversion approach to analyze CMP data collected across typical near-surface environments. Application to a field data set recorded at a well-constrained test site including a comparison to independent borehole and direct-push data, further illustrates the potential of the proposed approach, which includes a straightforward and understandable appraisal of nonuniqueness and uncertainty issues, respectively. We conclude that our methodology is a feasible and powerful tool to analyze GPR CMP data and allows practitioners and researchers to evaluate the reliability of CMP derived velocity models.

3.2 Introduction

In many archaeological, engineering, environmental, and geological applications, ground-penetration radar (GPR) is an important geophysical tool to investigate near- surface environments (e.g., Davis & Annan [1989]; Jol [2009b]). To accurately image subsurface structures such as geological layering or man-made objects with GPR, information regarding GPR velocity and its variations is crucial (Tillard & Dubois [1995]). For example, migration routines require an accurate velocity model to move dipping reflections to their correct position, unravel crossing events, and collapse diffractions (Yilmaz [2001]). Further processing steps whose success is closely related to the accuracy of the available velocity information include time-to-depth conversions and elevation corrections (Annan [2005]; Cassidy [2009b]). In addition, GPR velocity is increasingly used to aid the interpretation of reflection images and to quantitatively characterize the subsurface; i.e., to estimate petrophysical properties such as water content or porosity (e.g., Greaves *et al.* [1996]; Van Overmeeren *et al.* [1997]; Huisman *et al.* [2003a]; Tronicke *et al.* [2004]; Steelman & Endres [2012]; Hamann *et al.* [2013]).
To determine a GPR velocity model, different surveying approaches can be em-

ployed. Cross-hole tomography (e.g.,Binley *et al.* [2001]; Tronicke *et al.* [2002]) and vertical radar profiling (e.g., Cassiani *et al.* [2004]; Tronicke & Knoll [2005]) can provide detailed information regarding subsurface velocity variations. However, the feasibility of such borehole-based techniques is often limited due the limited number of available boreholes. Thus, the most common surveying strategies to obtain velocity information rely on surface-based common-offset (CO) or multi-offset survey geometries. When using CO data, hyperbola-shaped diffraction events, associated with isolated objects or sharp discontinuities, can be analyzed because the geometry of these events depends on the subsurface velocity distribution (e.g., Moore *et al.* [1999]; Bradford & Harper [2005];Porsani & Sauck [2007]). However, when the number and/or distribution of diffraction events is limited, the results of such analyses may not provide sufficient detail regarding velocity variations. Thus, a limited number of multi-offset CMP gathers is typically recorded to obtain one-dimensional (1D) velocity models at selected locations in the surveyed area (Annan [2005]). The analysis of such CMP data is commonly performed using reflection seismic processing tools based on the normal-moveout (NMO) model (e.g., spectral velocity analysis; Yilmaz [2001]). Here, we have to consider the fundamental assumptions of such NMO based velocity analysis, which include small offset-to-depth ratios, small velocity gradients, and plane horizontal reflectors (Al-Chalabi [1973]). Considering these assumptions, various studies have investigated the influence of different sources of errors on the derived GPR velocity estimates (Tillard & Dubois [1995]; Jacob & Hermance [2004]; Becht *et al.* [2006]; Booth *et al.* [2010]; Booth *et al.* [2011]) also considering the relevant seismic literature (e.g., Taner & Koehler [1969]; Levin [1971]; Hajnal & Sereda [1981]; Alkhalifah [1997]). For example, Booth *et al.* [2010] investigated timing errors associated with the finite duration of the GPR wavelet and their influence on the derived velocity model while Becht *et al.* [2006] studied the influence of layer dip and velocity contrast (spatial velocity changes that causes reflection and refraction). Summarizing the findings of the above cited publications illustrates that GPR interval velocity models derived from NMO based analyses may show significant errors hindering a detailed interpretation of the derived velocity variations (e.g., in terms of different petrophysical parameters). As an alternative, Harper & Bradford [2003] used the least-squares

inversion approach of Zelt & Smith [1992] to reconstruct a 1D velocity model from manually picked reflection traveltimes. Although the assumptions inherent in NMO based velocity analyses are avoided by this approach, we have to consider the limitations of applying such a linearized inversion strategy to the non-linear problem of reflected traveltime inversion (e.g., Sen & Stoffa [1995]). We desist from local optimization approaches, where a modification of an initial model is taken as result with the consequence that already a small variation of an initial model will reveal a fatal change of the result (Menke [1989]; Aster *et al.* [2013]). There is also a growing interest in multi-offset GPR surveying strategies adapting multi-fold acquisition geometries known from reflection seismics. The resulting data sets allow for generating densely-sampled, continues 2D or even 3D velocity models using techniques adapted from seismic data processing (Greaves *et al.* [1996]; Cai & McMechan [1999]; Pipan *et al.* [1999]; Becht *et al.* [2006]; Bradford *et al.* [2009]). In addition to NMO based workflows, this also includes the application of techniques known from seismic prestack migration velocity analysis which, for example, also allow for considering dipping reflectors and lateral velocity variations (Leparoux *et al.* [2001]; Bradford [2006]). Although the advantages of multi-fold data acquisition and analysis are well documented (see references above), the increased field and processing effort is often considered as a major limitation (e.g., Booth *et al.* [2008]) and, thus, also today the analysis of individual CMP gathers is crucial for extracting velocity information from surface-based GPR data.

In this study, we propose a novel workflow to analyze GPR CMP data. Our methodology is based on inverting reflection traveltimes using a global optimization approach known as particle swarm optimization (PSO). Combined with an accurate forward modeling procedure based on a fast marching eikonal solver (Sethian [1996]; Fomel [1997a]; Sethian & Popovici [1999]), our methodology avoids the fundamental assumptions of NMO based analyses and allows to directly invert for interval velocity models. We also generate representative ensembles of acceptable solutions which allows us to appraise uncertainties in the model space and, thus, to evaluate the reliability of CMP velocity models. In the following, we start by reviewing NMO based spectral velocity analysis. After that, we introduce the fundamentals of our PSO based inversion scheme which,

then, is tested and evaluated using synthetic data examples. Finally, we apply our method to GPR field data recorded across sand and gravel dominated deposits. Comparing the resulting velocity models to velocity models derived from NMO based analysis and to independent direct-push and borehole data, respectively, allows for evaluating our results including the derived uncertainty estimates.

3.3 Spectral velocity analysis

One of the standard tools for analyzing individual CMP gathers is spectral velocity analysis (Taner & Koehler [1969]; Yilmaz [2001]; Annan [2005]). Assuming a layered subsurface consisting of isotropic and homogeneous layers separated by plane interfaces, NMO based analyses are used to test a set of expected velocity values. The velocity spectrum is generated using a predefined measure of coherency (such as semblance or unnormalized cross-correlation) across the data gather in a predefined time window centered on hyperbolic trajectories calculated by

$$t_{NMO}(x) = \sqrt{t_0^2 + \frac{x^2}{\mathrm{v}_{NMO}^2}} \tag{3.1}$$

where x is the transmitter-receiver offset, t_0 the zero-offset traveltime, and v_{NMO} the normal-moveout velocity. The optimum stacking velocities are then selected by analyzing the maxima in the resulting velocity spectrum (i.e., calculated coherency values as a function of tested velocities and traveltimes) corresponding to primary reflection events in the analyzed CMP gather. Assuming horizontal interfaces and small transmitter- receiver offsets (compared to the reflector depth), the derived stacking velocities can be approximated by root-mean square (RMS) velocities which, then, can be converted to interval velocities using the classical equation developed by Dix [1955]. Dix's formulas accounts, but approximates the refracted ray paths across layer boundaries, what is valid with the small offset assumption.

To illustrate the traveltime errors associated with equation 3.1, we present a modeling example employing typical GPR offset ranges and velocity distributions (i.e., decreasing velocity with increasing depth). We compare t_{NMO} (equa-

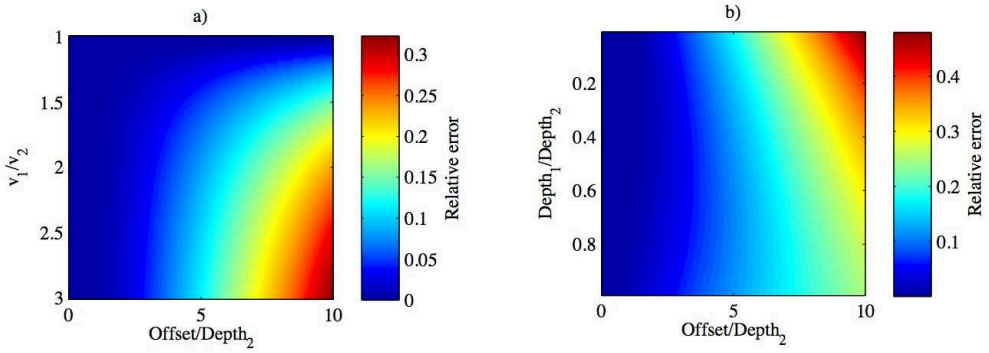

Figure 3.1: Relative errors associated with the NMO model (equation 3.1) for horizontally layered velocity models consisting of two interfaces (at Depth_1 and Depth_2) defining two homogenous layers with velocities v_1 and v_2. (a) Relative errors as a function of the offset-to-depth ratio and the velocity ratio between the upper and the lower layer for a fixed ratio of one between the thickness of the first and the second layer. (b) Relative errors as a function of the offset-to-depth ratio and the depth ratio between the upper and the lower layer for a fixed velocity ratio of $v_1/v_2 = 3$. For details see text.

tion 3.1) with traveltimes computed using a fast marching eikonal solver (t_{mod}), which is known as an accurate, stable, and computational efficient method for traveltime modeling (Sethian [1996]; Fomel [1997a]; Sethian & Popovici [1999]). For horizontally layered velocity models consisting of two interfaces, we compare the traveltime differences for the deeper reflector using relative errors calculated as $(t_{NMO} - t_{mod})/t_{NMO}$. In Fig. 3.1a, we show the resulting errors as a function of the offset-to-depth ratio (considering the depth of lowermost layer noted by Depth_2) and the velocity ratio between the upper and the lower layer (v_1/v_2). Here, the ratio between the thickness of the first and the second layer is fixed to one. The errors increase for increasing velocity contrasts and increasing offset-to-depth ratios and can be easily in the order of 5% to 10% and more. In Fig. 3.1b, we illustrate the relative errors as a function of the offset-to-depth ratio and the depth ratio between the upper and the lower layer ($\text{Depth}_1/\text{Depth}_2$) while the velocity ratio is fixed to $v_1/v_2 = 3$. Again, errors increase with increasing offset-to-depth ratios while the influence of the depth ratio between the two interfaces is more pronounced for larger values of the offset-to-depth ratio. Exemplary, we set now the depth of the second layer equal to one, what is a description for the case of a CMP gather taken with 10 m offset over a two layer case, where the second layer reaches the depth of on meter with lower end. For this case, in Fig. 3.1a) the first layer has a thickness of an half a meter and one velocity have to be

fixed an the other varied. In Fig. 3.1b) we my proceed respectively for the layer thicknesses and we set the velocities to constant.
The presented modeling exercise demonstrates the limitations of the NMO model for rather typical GPR situations and indicates that the procedure of deriving 1D velocity models from individual GPR CMP gathers using NMO based analyses is prone to errors. Especially, if we are interested in an interval velocity model, for example, to aid GPR data interpretation, we should employ techniques avoiding the assumptions inherent in NMO based approaches. Furthermore, an appropriate velocity analysis tool should allow for appraising resolution, and nonuniqueness issues and, thus, to quantify the uncertainties expected for a CMP based velocity model. With this motivation, we now introduce our methodology based on the global inversion of reflection traveltimes.

3.4 Global inversion of CMP traveltimes

In this section, we describe the methodological basics of our global inversion approach which is outlined in Fig. 3.2. We introduce the employed global optimization method which is known as particle swarm optimization (PSO) including the necessary details of our implementation to invert GPR traveltime data observed in CMP data sets.
Inspired by the social behavior of birds and fishes, PSO has been introduced by Kennedy & Eberhart [1995] as a tool to globally solve optimization problems. Due to its flexibility and computational efficiency the method has been recognized as a feasible tool in a variety of applications (Poli [2008]). PSO based inversion method is rigorous in terms implementation and shows faster convergence compared in contrast to other global optimization approaches (e.g., simulated annealing approaches), we will show that the PSO method is an elegant, fast and promising way to describe GPR CMP traveltime data plausible with more precise and completely initial state independent optimized, statistically representative subsurface velocity models with uncertainties and allows further quantitative soil parameter predictions. More recently, there is also a growing interest in using PSO to solve typical inverse geophysical problems (Shaw & Srivastava [2007]; Fernández Martínez *et al.* [2010]; Monteiro Santos [2010]; Tronicke *et al.*

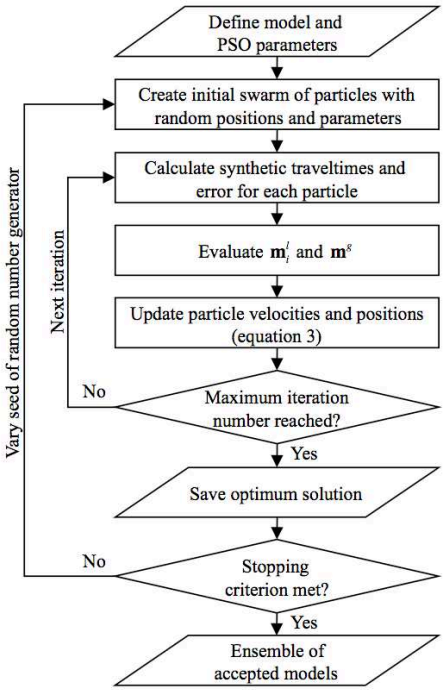

Figure 3.2: Flow diagram illustrating the key proposed PSO-based global inversion procedure of CMP reflection traveltimes. For details see text.

[2012]; Wilken & Rabbel [2012]). Here, we use PSO to globally invert traveltimes determined from GPR CMP surveys and our implementation basically follows Tronicke *et al.* [2012] who employed PSO to invert crosshole seimic traveltime data. A standard personal machine with quart core and 6 GB RAM was used to achieve results like demonstrated in this paper.

In PSO, the swarm consists of a number of particles which explore a predefined model space. The location of the i-th particle in the model space is represented by a model vector m_i. Here, we invert for a 1D velocity model parameterized using a predefined number of layers and, thus, m_i is defined by layer (interval) velocities and layer thicknesses. The fitness of a particle at its current location in the model space is evaluated using an objective function L_i which we define as

$$L_i = \frac{1}{N} \sum_{j=1}^{N} \sqrt{(t_{obs,j} - t_{mod})^2}, \tag{3.2}$$

where t_{obs} and t_{mod} are observed and forward modeled traveltimes of primary reflections, respectively, and N represents the total number of traveltimes used

for the inversion. We calculate t_{mod} using a fast marching eikonal solver because this technique is accurate (e.g., accounts for refraction across layer boundaries) and computational efficient (Sethian [1996]; Fomel [1997a]; Sethian & Popovici [1999]).

In PSO, to ensure information exchange within the swarm, the movement of an individual particle through the model space is determined by combining the history of its own fitness (cognitive component) with those of the entire swarm (social component). Combining these components with some random perturbations results in a vector Φ (known as the velocity vector in PSO terminology) that controls the movement of the particles during the iterative optimization procedure. At iteration $k+1$, the new location of the i-th particle is calculated by

$$\begin{aligned} \Phi_i^{k+1} &= w\Phi_i^k + c_1 r_1^{k+1}(m_i^l - m_i^k) + c_2 r_2^{k+1}(m^g - m_i^k), \\ m_i^{k+1} &= m_i^k + \Phi_i^{k+1}, \end{aligned} \tag{3.3}$$

where m_i is the personal best position of the i-th particle, m^g is the global best position of the entire swarm, r_1 and r_2 are randomly drawn form a uniform distribution in [0,1], $w = 0.7298$ is the inertia weight serving as a memory of previous velocities, and $c_1 = c_2 = 1.4962$ are the acceleration constants controlling the relative proportion of cognition and social interaction within the swarm. These unphysical parameters were introduced generally by Eberhart & Shi [2000] and Clerk & Kennedy [2002], to ensure efficient convergence of the algorithm. The best positions are determined in both cases with the stored best objective functions of the particles, with comparison of personal history or swarm community, respectively.

When starting the PSO optimization procedure, Φ is set to zero and the particles are randomly initialized in the predefined model space. Constraining the model space to value ranges of layer velocities for unsaturated or saturated sediment sand reasonable (to time window corresponding) thicknesses as a priori information helps to speed up the convergence behavior of the algorithm. After this initialization, the forward problem is solved for each particle, the objective function (equation 3.2) is evaluated, and m_i^l and m^g are stored. In the following

iterations, the model vectors are updated (equation 3.3) and compared to m_i^l and m^g. If the new model of the i-th particle is better than the current personal best model and the best global model, m_i^l and m^g are updated. This procedure is repeated until a predefined stopping criterion is reached (inner loop in Fig. 3.2). The final m^g represents the optimum solution; i.e., a 1D velocity model explaining our traveltime data set.

Before starting the PSO optimization procedure, we have to define the number of particles and reasonable stopping criteria (maximum number of iterations and/or acceptable value of the objective function). To find optimum parameters in terms of desired error level as well as computational effort for a specific problem, some initial parameter testing is required. For the CMP examples presented in this study, generally 20 particles and 300 iterations are sufficient to explain our data. Furthermore, our parameter tests have shown that not to strong variations (i.e., one digit) of these PSO parameters (e.g., number of particles) have no critical impact on the obtained results, but on computation time. The number of layers for the searched subsurface solution, is achieved by inspection of the presence of picked reflection events in the CMP gather.

3.5 Generating a Representative Ensemble

As indicated by the outer loop in Fig. 3.2, we repeat the above described PSO optimization procedure with different randomly generated starting models and different seeds of the random number generator. Herewith, we generate an ensemble of models explaining the data equally well (Fernández Martínez *et al.* [2010]; Tronicke *et al.* [2012]). Analyzing such an ensemble allows us to assess uncertainty and nonuniqueness issues in the formulated inverse problem; for example, to appraise how well a layer boundary or the velocity of a certain layer is resolved. To evaluate the representativeness of the generated ensemble, we follow Sen & Stoffa [1995] and compute the elements M_{ij} of the posterior correlation matrix $\mathbf{M}$ by

$$M_{ij} = \frac{C_{ij}}{\sqrt{C_{ii}C_{jj}}} \tag{3.4}$$

where C_{ij} is an element of the posterior covariance matrix $\mathbf{C}$. The matrix $\mathbf{C}$ is calculated from the ensemble of accepted solutions m_g by

$$\mathbf{C} = \frac{1}{M}\sum_{j=1}^{M}(m_j^g - \langle m_g \rangle)(m_j^g - \langle m_g \rangle)^T \tag{3.5}$$

where M is number of models within the ensemble and

$$\langle m^g \rangle = \frac{1}{M}\sum_{j=1}^{M} m_j^g \tag{3.6}$$

By analyzing changes in $\mathbf{M}$ during the inversion procedure (i.e., ensemble generation) allows us to evaluate the representativeness of the ensemble (Sen & Stoffa [1995]). If no significant variations in $\mathbf{M}$ are detected when new models are added to the ensemble, we assume that the ensemble is representative and allows for reliable posterior statistical analyses. For our inversion problem, we found that an ensemble consisting of 100 models characterized by an acceptable data fit can typically be regarded as representative. Because the found empirical distributions of the model parameters are typically not following a normal distribution, we use robust statistical measures to analyze the distributions in more detail. For our synthetic and field examples, we compute the median, the 5th to 95th percentile, and the 25th to 75th percentile to characterize the central tendency and the spread of the underlying parameter distributions. In addition, the matrix $\mathbf{M}$ (equation 3.4) can be used to analyze correlations between the individual model parameters providing further insights into the formulated inverse problem and employed model parameterization, respectively.

3.6 Synthetic Examples

In this section, we test and evaluate the proposed workflow using synthetic examples. We generate synthetic traveltime data sets simulating traveltimes from reflected events as observed in GPR CMP surveys and invert these data using our PSO based inversion procedure. Furthermore, such synthetic examples allow us to analyze ensemble characteristics and uncertainties which can be expected

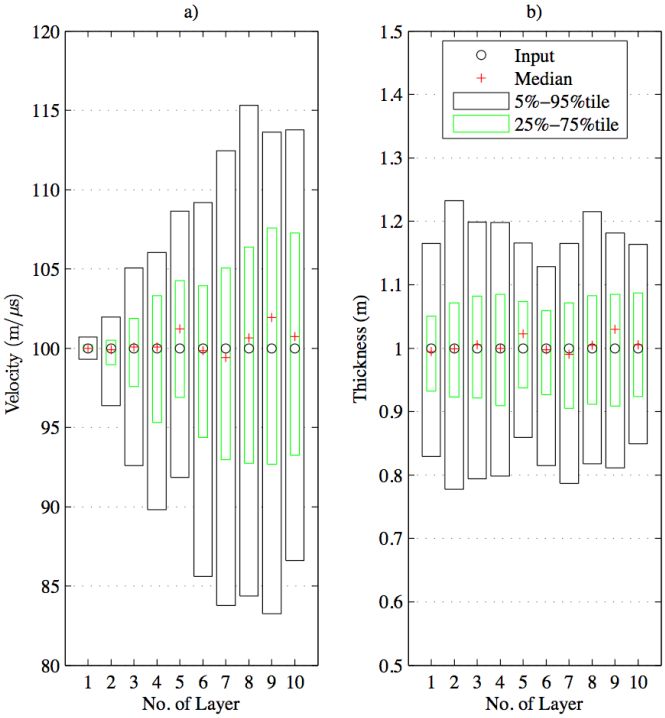

Figure 3.3: Results of globally inverting a synthetic reflection traveltime data set (example 1) including a comparison to the input model parameters. For (a) layer velocities and (b) layer thicknesses the median, the 25th to 75th, and the 5th to 95th percentile calculated from the ensemble of models are shown. Layer number increases with increasing depth; i.e., number one represents the uppermost layer.

for typical CMP data sets recorded across typical subsurface environments.

Example 1

The first synthetic example represents a CMP survey recorded with a trace spacing of 0.1 m and maximum offset of 15 m across a ten-layer case where each layer is characterized by a constant interval velocity of 100 m/μs and a thickness of 1 m (i.e., the deepest layer boundary is found at 10 m depth). With this model we want to investigate depth dependent model characteristics which might be related to decreasing moveout with increasing interface depth for a fixed CMP geometry. The results of globally inverting the corresponding noise-free traveltime data set are presented in Fig. 3.3. For thiscase thicknesses varies between 0.5 to 1.5 m and velocities varies between 0.08 to 0.12 m/μs, as PSO search space limits. We show the median, the 25th to 75th, and the 5th to 95th percentile calculated from

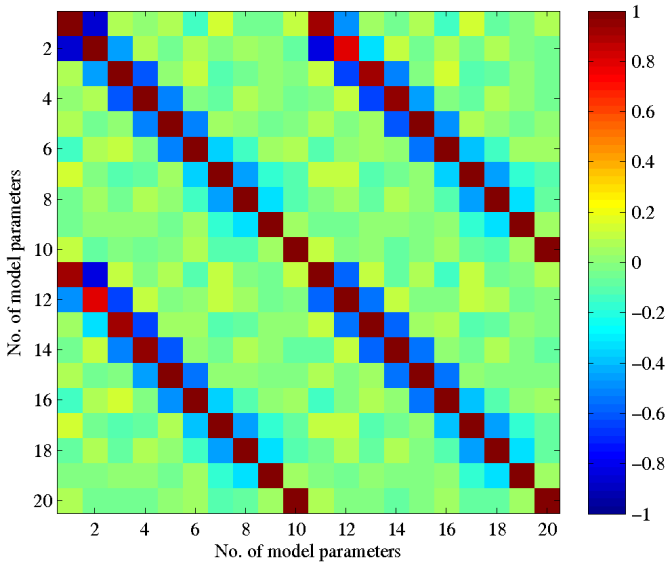

Figure 3.4: Model parameter correlation matrix calculated from the final ensemble of accepted models. Model parameters 1-10 correspond to the thicknesses of layers 1- 10 while parameters 11-20 represent the corresponding layer velocities.

the ensemble of model parameter distributions (interval velocity and thickness of layers number one to ten where layer number one corresponds to the uppermost layer) and compare it to the corresponding input values. The input values of velocity and thickness are well recovered by the median values of the parameter distributions (maximum discrepancies <2%). In Fig. 3.3a, the 25th to 75th and the 5th to 95th percentile values indicate maximum uncertainties of ∼7% and ∼15%, respectively, with a trend of increasing uncertainty with increasing depth (i.e., increasing layer number). For the thicknesses (Fig. 3.3b), we observe no characteristic trend with depth and the 25th to 75th and the 5th to 95th percentile values indicate uncertainties of ∼5-8% and ∼13-22%, respectively. The observation of increasing uncertainties in velocity with increasing depth can be related to the lower moveout observed for the deeper reflection events in comparison to shallow reflections at the same offset; i.e., shallow events are more sensitive to a certain variation in velocity than deeper events.

In Fig. 3.4, we show the posterior correlation matrix calculated from the final ensemble of accepted solutions. This matrix can be used to analyze the interdependence between different model parameters. In Fig. 3.4, model parameters one to ten correspond to the layer thicknesses of layer number one to ten while param-

eters eleven to twenty represent the corresponding layer velocities. We observe high positive correlations between the thickness and the velocity of a specific layer while high negative correlations are observed between thickness and velocity of a specific layer and the thicknesses and velocities of the neighboring layers. These observations illustrate that the uncertainties associated with the corresponding pairs of model parameters are highly correlated and anticorrelated, respectively, and that the corresponding parameters can not be independently resolved by the data set; i.e., only some linear combination of the parameters are resolved Tarantola [2005]. For example, due to the high positive correlations (close to one) between layer thickness and velocity we can not expect to accurately resolve both parameters for a specific layer; i.e., if one of the parameters is estimated too high or to low this can be easily compensated by increasing or decreasing the other corresponding parameter (e.g., layer five in Fig. 3.3). Thus, there is an inherent nonuniqueness in the formulated inverse problem which we have to be aware of when analyzing the inversion results. Our experience with a number of different synthetic and field CMP data sets shows that we always observe similar patterns and correlations in the resulting posterior correlation matrices and, thus, these matrices will not be shown for the following examples.

Example 2

Our second synthetic example simulates a rather typical hydrogeological situation where a shallow groundwater table results in a sharp velocity decrease. In such situations, we might be interested in resolving rather small velocity variations in the water saturated zone which, for example, could be interpreted in terms of porosity variations. Therefore, the input five-layer velocity model comprises a 2 m thick top layer with a velocity of 100 m/μs followed by a sequence of four 2 m thick layers characterized by velocities of 50 m/μs and 60 m/μs, respectively. The CMP survey geometry is identical to the first example; i.e., the trace spacing is 0.1 m and the maximum offset is 15 m. This second synthetic example was achieved with PSO parameter boundaries for the unsaturated first layer from 0.08 m/ns to 0.15 m/ns and for the saturated deeper layers from 0.09 m/ns to 0.04 m/ns, thickness range was kept in the range 0.2 m to 10 m for all layers.

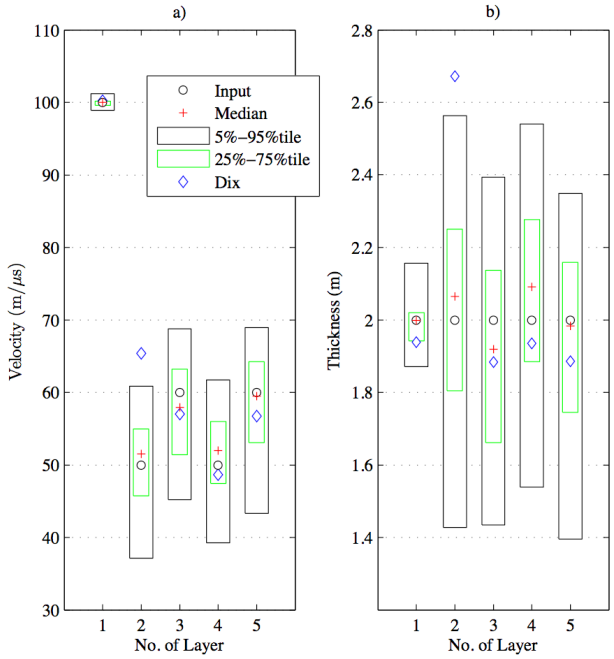

Figure 3.5: Results of globally inverting a synthetic reflection traveltime data set (example 2) including a comparison to the input model parameters and the results of NMO based analysis relying on Dix's equation. For (a) layer velocities and (b) layer thicknesses the median, the 25th to 75th, and the 5th to 95th percentile calculated from the ensemble of models are shown. Layer number increases with increasing depth; i.e., number one represents the uppermost layer.

Thus we adapted search space boundaries, to ground water table expectation, for faster convergence and for more sensitivity for velocities changes between deeper layer in the water saturated zone and we will proceeded similar with the field example.

The results of globally inverting the corresponding noise-free traveltime data set are presented in Fig. 3.5, where we visualize the median, the 25th to 75th, and the 5th to 95th percentile calculated from the final ensemble of model parameters. The input and the achieved medians of the results are indicated in the figures with circles and cross symbols, respectively. Comparing the input model parameters to the median layer velocities and thicknesses from our PSO based inversion illustrates that the input model is accurately reconstructed (maximum discrepancies <5 %) including the velocity variations in the saturated zone (layers two to five). However, the 25th to 75th and the 5th to 95th percentile values indicate uncertainties in the underlying parameter distributions in the order of 10% and 20%, respectively. While the velocity of the first layer is well resolved,

the estimated uncertainties for the velocities of layers two to four indicate reduced confidence in resolving this alternating sequence with velocity contrasts of 10 m/μs. For comparison, we also show the results of NMO based spectral velocity analysis including a transformation into interval velocity using Dix's equation (blue symbols in Fig. 3.5). Although this analysis provides an impression on subsurface velocity variations which can be used to aid traveltime picking and defining a reasonable parameter constraints for fast convergence of the global inversion. The sharp velocity contrast between layers 1 and 2 causes an overestimation of the parameters of layer 2 in the order of 30%, which clearly illustrates the limitation of NMO based velocity analyses.
In conclusion, the discussed and further synthetic examples (not shown here) demonstrate that our PSO based global inversion is a feasible tool to reconstruct 1D velocity models from typical CMP traveltime data even in the presence of sharp velocity contrasts. Furthermore, our approach provides reliable estimates of uncertainty, which, for example, show the challenge in resolving minor velocity variations underneath a shallow groundwater table using surface-based CMP data.

3.7 Field Example

To demonstrate the applicability of our global inversion approach to field data, we use it to invert reflection traveltimes manually picked from a CMP data set recorded at a well constrained test site in Horstwalde, Germany. This site has been installed by the University of Potsdam and the German Federal Institute for Materials Research and Testing (BAM). As known from a variety of available borehole, direct-push, and geophysical data, the shallow geology is characterized by layered sequences of sand and gravel dominated glaciofluvial deposits showing only minor inclusions of clay, lignite, and organic material (Linder *et al.* [2010]; Schmelzbach *et al.* [2011]; Tronicke *et al.* [2012]). Here, we focus on a single GPR CMP data set recorded close to borehole B1/09, where different borehole and direct-push logs are available (Tronicke *et al.* [2012]). The data were recorded using 100 MHz antennae, a sampling interval of 0.1 ns, minimum and maximum source-receiver offsets of 0.4 m and 14.7 m, respectively, and stepwise offset incre-

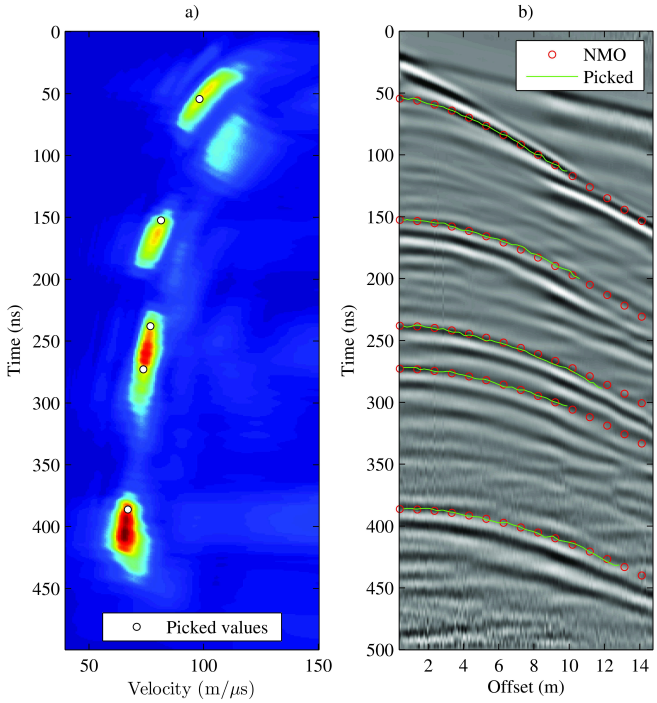

Figure 3.6: CMP field data example recorded at the Horstwalde test site, Germany. (a) NMO based velocity spectrum calculated from (b) the processed CMP data gather. In (a), yellow to red colors indicate maximum coherency values. In (b), the hyperbolic NMO events calculated using equation 3.1 and the picked values from (a) are indicated by red symbols while the green lines represent the traveltimes picked in the raw data section (not shown) which are used as input for our global inversion scheme.

ments of 0.1 m.

In Fig. 3.6, we present the CMP data section after amplitude scaling and bandpass filtering as well as the result of NMO based spectral velocity analysis calculated using the un-normalized cross-correlation as coherency measure. Five reflection events can be clearly identified by their hyperbolic moveout in the data section (Fig. 3.6b) and by the corresponding maximum values in the velocity spectrum (Fig. 3.6a). Inverting the picked values from the velocity spectrum using Dix's equation provides a first impression on subsurface velocity variations (blue symbols in Fig. 3.7).

From this analysis, we learn that the first reflection characterizes the transition from unsaturated to water saturated sediments while the deeper reflections are associated with sedimentary structures in the saturated zone. While the unsaturated sediments up to a depth of ∼3 m are characterized by velocities of ∼100 m/μs, the results of NMO based analysis indicate velocities of ∼60 m/μs

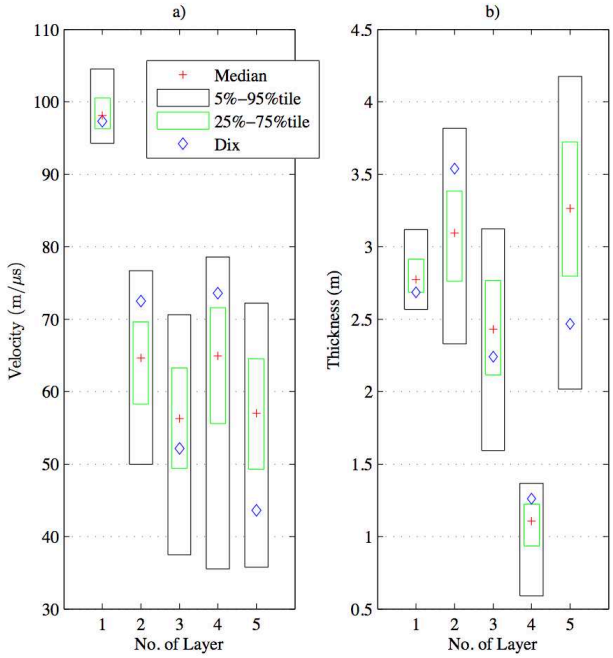

Figure 3.7: Results of globally inverting reflection traveltimes from the field data set including a comparison to the results of NMO based analysis relying on Dix's equation. For (a) layer velocities and (b) layer thicknesses the median, the 25th to 75th, and the 5th to 95th percentile calculated from the ensemble of models are shown. Layer number increases with increasing depth; i.e., number one represents the uppermost layer.

for the saturated sediments up to a depth of ∼12 m. Guided by the results of NMO based analysis we have manually picked the arrival times of the identified reflection events (Fig. 3.6b) in the raw data section (not shown). Furthermore, we have used the NMO based velocity model to constrain the model space in our global inversion approach to reasonable values of the individual model parameter. In Fig. 3.7, we illustrate the results of globally inverting the reflection traveltime data set. We show the median, the 25th to 75th, and the 5th to 95th percentile calculated from the ensemble of model parameter distributions (interval velocity and thickness of layers number one to five where layer number one corresponds to the uppermost layer) and also compare these values to the result of NMO based analysis. Comparable to our second synthetic example, the velocity and the thickness of the first layer are well resolved and we observe only minor differences between the results of global inversion and NMO based analysis. The thickness of the first layer is also in excellent agreement with the depth of the groundwater table measured during our GPR measurements at a depth of 2.73 m with a water level meter in the borehole. Also similar to our synthetic exam-

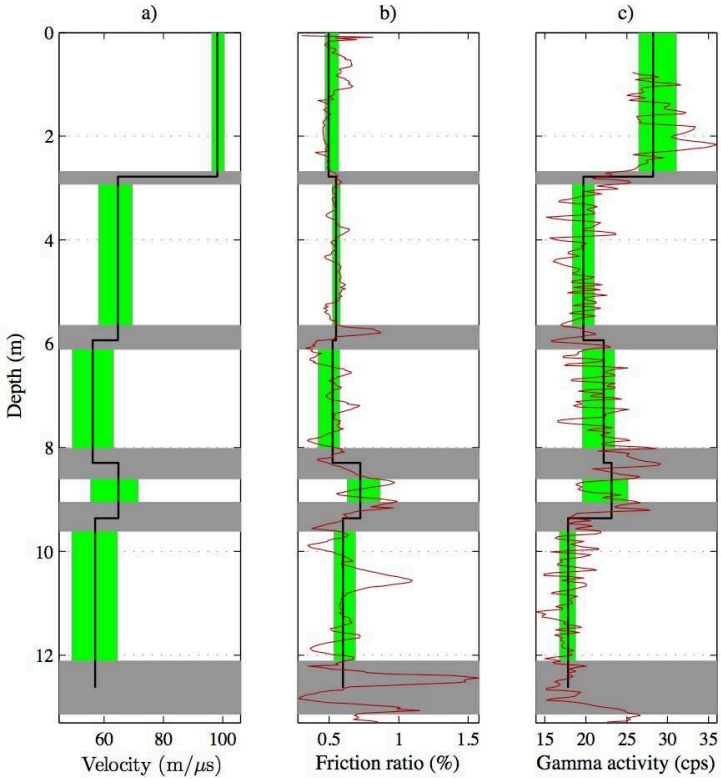

Figure 3.8: Comparison of global inversion results of the field data example to selected logs available at the CMP location at the test site. (a) CMP derived layer velocities as a function of depth, (b) friction ratio as function of depth as calculated from CPT logging data, and (c) natural gamma activity as derived from borehole GR logging data. In (a) to (c), gray boxes indicate depth uncertainties as estimated by the 25th to 75th percentile values from the global inversion result (Fig. 3.7). In (a), the green boxes indicate velocity uncertainties as estimated by the 25th to 75th percentile values from the global inversion result (Fig. 3.7), while in (b) and (c) the green boxes characterize the variability (25th to 75th percentile) of friction ratio and gamma activity, respectively, calculated from the logging data in the depth intervals defined by the median model in (a).

ple, we notice increased uncertainties in the saturated zone (layers 2 to 5) and some significant differences (up to ∼30%) between the global inversion result and the NMO based analysis. Again, these discrepancies are associated with the assumptions inherent in NMO based approaches; i.e., small offset-to-depth ratios and small velocity gradients across layer boundaries. Uncertainties of PSO are widened in contrast to the shown synthetic examples, what indicates the quality of the picked traveltimes, in terms of noise, sampling precision and offset errors.

To further check the consistency of our derived velocity model including the derived estimates of uncertainty (Fig. 3.8a) with independent data, we compare it to two selected direct-push and borehole logs (Fig. 3.8b and 3.8c). The shown friction ratio log was measured using a standard cone-penetration test tool and is

indicative for different soil types (Lunne *et al.* [1997]). The log of natural gamma-ray (GR) activity was recorded with a constant logging speed using a standard borehole tool measuring activity in counts per second (cps). For each of the layers identified by our global traveltime inversion procedure, we have calculated the median and the 25th to 75th percentile values to characterize the central tendency and the variability of the two logging parameters within individual layers. In doing so, we basically upscale the core and logging data to the spatial scale of the structures imaged by our CMP data set. When comparing the parameter-depth models in Fig. 3.8, we see that the imaged velocity variations and depths of the interfaces, respectively, largely correspond to compositional changes indicated by the logging data. For example, for the GR data (Fig. 3.8c) in the saturated zone (below depths of ∼3 m) we notice increasing GR median and 25th to 75th percentile values with depth (layers 2 to 4) while the lowermost layer (layer 5) is characterized by minimum median values and minimum variability. As similar observation can be made for the friction ratio log (Fig. 3.8b), we conclude that the derived 1D GPR velocity model is largely consistent with independent logging data.

3.8 Conclusion

In GPR surveying, CMP surveys are routinely employed to determine 1D velocity models collected at selected locations across a field site. We have presented a global inversion approach based on PSO to analyze reflection traveltimes observed in such CMP data sets. As our approach employs an accurate forward modeling routine which accounts for refraction effects, our methodology avoids the inherent assumptions of NMO based velocity analysis and, thus, provides more accurate velocity estimates than these standard analysis tools. Furthermore, our inversion approach can be used to generate an ensemble of acceptable solutions. Analyzing a representative ensemble allows for analyzing the interdependence between different model parameters. The observed correlations between layer thicknesses and velocities within individual layers as well as with neighboring layers illustrate the fundamental limitations of deriving accurate velocity estimates from a single CMP gather. From the generated ensemble of solutions, we also calculate different

statistical measure to characterize the central tendency as well as the variability of the individual model parameters. For our synthetic and field examples, we have used the median, the 25th to 75th, and the 5th to 95th percentile to characterize the underlying parameter distributions and to provide reliable estimates of uncertainty. We found that great changes of velocity, such as those associated with a shallow groundwater table, decrease our ability to accurately resolve the model parameters for deeper layers. Because our PSO based inversion approach is easy to implement, needs less parameter adjustments, and provides faster convergence compared with other more common global optimization approaches (e.g., simulated annealing methods), we believe that the presented methodology is a feasible and powerful tool to analyze GPR CMP data and allows practitioners and researchers to evaluate the uncertainties of CMP derived velocity models.

Chapter 4

Vertical radar profiling: combined analysis of traveltimes, amplitudes, and reflections

Jens Tronicke and Göran Hamann
Submitted to Geophysics, November 15, 2013

4.1 Abstract

Vertical radar profiling (VRP) is a single-borehole geophysical technique, where the receiver antenna is located within a borehole while the transmitter antenna is placed at one or various offsets from the borehole. Today, VRP surveying is primarily used to derive 1D velocity models by inverting the arrival times of direct waves. Using field data collected at a well-constrained test site in Germany, we present a VRP workflow relying on the analysis of direct-arrival traveltimes and amplitudes as well as on imaging reflection events. To invert our VRP traveltime data, we use a global inversion strategy resulting in an ensemble of acceptable velocity models and, thus, allows us to appraise uncertainty issues in the estimated velocities as well as in porosity models derived via petrophysical translations. In addition to traveltime inversion, the analysis of direct-wave amplitudes and reflection events provides further valuable information regarding subsurface properties

and architecture. The employed VRP amplitude pre-processing and inversion procedures are adapted from crosshole ground-penetrating radar (GPR) attenuation tomography and result in an attenuation model, which can be used to estimate variations in electrical resistivity. Our VRP reflection imaging approach relies on corridor stacking, which is a well-established processing sequence in vertical seismic profiling. The resulting reflection image outlines bounding layers and can be directly compared to surface-based GPR reflection profiling. In our case study, the results of combined analysis of VRP, traveltimes, amplitudes, and reflections are consistent with independent core and borehole logs as well as GPR reflection profiles, which enables us to derive a high-resolution hydrostratigraphic model as needed, for example, to understand and model groundwater flow and transport.

4.2 Indroduction

Ground-penetrating radar (GPR) is a widely used geophysical technique to investigate the shallow subsurface. Most GPR surveys are employed using surface-based antenna configurations to collect common-offset reflection profiles (Davis & Annan [1989]; Jol [2009b]). Although such reflection profiles can provide valuable information regarding subsurface structures and architecture (e.g., Schmelzbach *et al.* [2011]), they usually not provide direct information on subsurface material properties such as dielectric or hydrological parameter values. In addition, for migration, topographic correction, and time-to-depth conversion of GPR reflection data, information regarding GPR velocities is required (Cassidy [2009b]). Typically, common-midpoint (CMP) surveys are used to obtain the velocity information required for processing surface-based reflection data. Such CMP-derived velocity estimates, which typically rely on a normal moveout (NMO) based analysis strategy, have also been used for a more quantitative characterization of the subsurface (e.g., to estimate water content; Greaves et al., 1996). However, it is well known that the resolution capabilities of such CMP-based velocity estimates are limited and that these estimates are often characterized by high uncertainties (Tillard & Dubois [1995]; Hamann *et al.* [2013]).

As an alternative to CMP surveying, borehole-based GPR techniques have been

proposed because we generally can expect an increased resolution compared to surface- based techniques. For example, in environmental and hydrological applications crosshole GPR tomography is increasingly used because the resulting tomographic images allow for a detailed characterization of the subsurface between pairs of boreholes (Binley *et al.* [2001]; Allumbaugh *et al.* [2002]; Tronicke *et al.* [2002]; Tronicke *et al.* [2004]; Becht *et al.* [2004]; Clement & Barrash [2006]; Gloaguen *et al.* [2007]; Looms *et al.* [2008]). However, in many near-surface environments successful application of crosshole imaging requires closely spaced boreholes with lateral distances of $\sim$ 10 m or less. In addition, the resolution of the inverted tomographic parameter models depends on the geometry of the experiment, the employed inversion strategy, and on the true subsurface parameter variations to be imaged (e.g., Rector & Washbourne [1994]; Day-Lewis *et al.* [2005]). In crosshole traveltime tomography, we generally expect the best resolution in the central part of the model and poorer resolution paired with high uncertainties in the reconstructed parameter values close to the boreholes. This often hinders the development of site- specific petrophysical models linking, for example, tomographic properties with other material properties such as porosity or hydraulic conductivity as derived, for example, from logging data (Day-Lewis *et al.* [2005]).

In contrast to crosshole GPR surveying, vertical radar profiling (VRP) is a single-borehole technique to investigate the subsurface close to one borehole (Knoll [1996]). The VRP technique can be employed for reflection imaging (Zhou & Sato [2000]; Böniger *et al.* [2006]) and might also be considered for 1D attenuation tomography. However, today it is primarily used to derive 1D velocity models by inverting the traveltimes of direct arrivals typically employing a linearized inversion scheme. Within the past decade, a number of successful applications indicate the potential of the method, especially, to obtain high-resolution velocity models in the vicinity of a borehole. Such velocity models have been used to process and calibrate surface-based GPR reflection data and also to estimate hydrological and engineering material properties (Knoll & Clement [1999]; Murray *et al.* [2000]; Hammon *et al.* [2002]; Pringle *et al.* [2003]; Cassiani *et al.* [2004]; Böniger *et al.* [2006]; Spillmann *et al.* [2006]; Cassiani *et al.* [2008]; Harbi. & McMechan [2011]; Schmelzbach *et al.* [2011]; Vignoli *et al.* [2012]; Igel *et al.* [2013]).

In this study, we want to promote a more profound analysis of VRP data. In addition to inverting direct-arrival traveltimes using a global optimization approach, our strategy includes the inversion of direct-arrival amplitudes as well as VRP reflection imaging. Thereby, we obtain a 1D velocity model including some quantitative estimates of uncertainty, an attenuation model primarily reflecting variations in electrical resistivity, and a reflection image enhancing our understanding of subsurface architecture. By using field data from a well constrained test in Germany, we illustrate the benefit of such an advanced analysis strategy, which includes improved abilities to develop a site-specific petrophysical understanding and linking borehole data to surface GPR reflection data. In the following, we present our methodology by reviewing some important VRP data characteristics, by introducing our traveltime and amplitude inversion approaches, and by providing details regarding the employed reflection imaging approach. After that, we analyze VRP field data collected within a shallow sedimentary aquifer to improve our hydrological understanding of the system. As our field data base also includes surface GPR reflection data, natural gamma activity logs, electrical conductivity logs, and grain size information obtained by sieve analysis of core material, we can compare our VRP results to independent data and develop an integrated analysis strategy to characterize subsurface architecture and material properties in detail.

4.3 Methodology

4.3.1 Vertical radar profiling (VRP)

In VRP surveying, the transmitter antenna is placed at one or several fixed offsets from the borehole on the ground and the receiver antenna is lowered down a borehole (Fig. 4.1a). Thus, VRP is conceptually similar to the better-known vertical seismic profiling (VSP) technique (Hardage [2000]). However, as pointed out and analyzed in detail by Tronicke & Knoll [2005], there are some differences to VSP, which have to be considered when acquiring and analyzing VRP data. First, in addition to direct and reflected events we have to consider waves critically refracted at the earth surface (Fig. 4.1). These refracted waves can be a

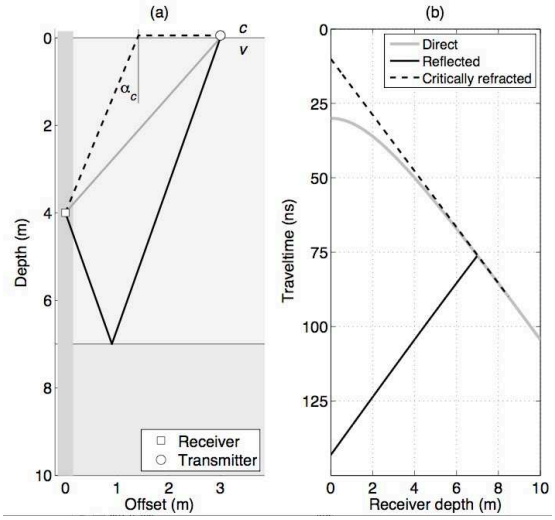

Figure 4.1: (a) Sketch illustrating VRP survey geometry (transmitter antenna at ground surface and receiver antenna in a borehole) and major travelpaths of direct, reflected, and critically refracted events. (b) Traveltime curves for direct, reflected, and critically refracted events. In (a), α_c is the critical angle at the groundair interface and c and v are GPR velocities in air and in a homogenous, isotropic subsurface. Both the travelpaths in (a) and the traveltime curves in (b) are calculated using a subsurface velocity of 0.1 m/ns and a horizontal reflecting interface at 7.0 m depth (modified after Tronicke & Knoll [2005]).

major limiting factor in VRP surveying because they are likely to interfere with the direct arrivals (as demonstrated by the example in Fig. 4.1b) and, thus, reduce the reliability of picking direct-arrival traveltimes and amplitudes. To avoid recording critically refracted waves, relatively short transmitter-borehole offsets are required. Second, we have to consider the influence of the radiation patterns of typical VRP antenna configurations on data quality. Typically, the transmitting antenna is oriented radially from the borehole resulting in a co-polarized antenna configuration. Tronicke & Knoll [2005] analyzed the resulting co-polarized VRP radiation patterns by numerical modeling and by combining the analytical far-field patterns of an infinitesimal horizontal dipole with that of an infinitesimal vertical dipole. They found minimum amplitude sensitivity for near-vertical ray paths and best signal-to- noise ratios for medium to far offsets between the transmitter and the borehole. Thus, there is a trade-off between the quest to record data with optimum data quality and the requirement to avoid waves critically refracted at the earth's surface. As a consequence, when acquiring VRP data at a given field site, multiple lateral offsets should be recorded to ensure optimum data quality and information content.

4.3.2 Traveltime inversion

Today, VRP data are primarily used to derive 1D velocity models close to a borehole by inverting the traveltimes of direct arrivals. Traveltime picking is usually performed in a manual or semi-automated fashion after minor data processing typically including time-zero corrections, dc bias removal, careful bandpass filtering, as well as amplitude scaling and balancing (e.g., Clement & Knoll [2006]). Traveltime inversion is typically performed using some kind of regularized, linearized inversion scheme (e.g., Cassiani *et al.* [2004]; Tronicke & Knoll [2005]; Clement & Knoll [2006]; Vignoli *et al.* [2012]); i.e., a local optimization approach is used to iteratively modify a user-specified initial model and smoothness (or other) regularizations are used to stabilize the inversion. The model parameterization usually relies on constant velocity layers with fixed layer thicknesses typically in the order of a few decimeters. Often, these inversion approaches also involve the assumption of straight ray paths which, comparable VSP data, might however be critical if major velocity contrasts are present and medium to far offset data are included in the inversion (e.g., Schuster *et al.* [1988]; Moret *et al.* [2004]).

In this study, we use a different approach for traveltime inversion. Our approach relies on combining an efficient global optimization algorithm known as particle swarm optimization (PSO; Kennedy & Eberhart [1995]) with a forward modeling procedure based on a fast marching eikonal solver, which has proven to be efficient and accurate also in the presence of sharp velocity contrasts (Sethian [1996]; Fomel [1997b]; Sethian & Popovici [1999]). Compared to linearized (local) inversion approaches, the chosen PSO- based global optimization approach allows for generating results independent of the starting model and for exploring the model space in more detail, which in turn provides a better chance to find the global minimum (Sen & Stoffa [1995]). Furthermore, such global approaches enable us to generate an ensemble of models that explain the data equally well and, thus, can be used to assess uncertainty and nonuniqueness issues in the formulated inverse problem. As a detailed description of PSO and its application to inverse geophysical problems is beyond the scope of this paper, interested readers are referred to the literature where a number of recent studies provide

details regarding implementation and illustrate a variety of possible geophysical applications (Shaw & Srivastava [2007]; Fernández Martínez *et al.* [2010]; Monteiro Santos [2010]; Tronicke *et al.* [2012]; Wilken & Rabbel [2012]; Hamann *et al.* [2013]). Here, we employ the PSO-based traveltime inversion approach described in detail by Tronicke *et al.* [2012]. This approach has been originally developed to invert traveltime data from crosshole seismic experiments but can easily be modified to invert other traveltime data sets such as those derived from VRP surveying.

For inverting our VRP traveltime data, we use a model parameterization relying on a fixed number of constant velocity layers describing a 1D velocity model around the borehole. After some initial parameter testing, we found that 19 constant-velocity layers with variable thicknesses (resulting in 37 model parameter) provide enough flexibility to explain our VRP traveltime data set. We also found that this parameterization provides more flexibility and more stable results compared to a model parameterization relying on constant-thickness layers. Further parameter tests were performed to select the PSO parameters number of particles and number of iterations. Here, we found that a swarm consisting of 50 particles and 300 iterations are sufficient to fit our traveltime data. Within the optimization procedure, we use the root-mean-square (rms) error between calculated and measured traveltimes as objective function, i.e., to evaluate the fitness of the current model. Using this strategy, we repeatedly inverted our data set using different seeds of the random number generator to obtain an ensemble of 210 velocity models explaining our data equally well.

4.3.3 Amplitude inversion

In different applications of crosshole GPR, ray-based amplitude inversion (attenuation tomography) has proven to be a valuable tool to image subsurface features not detectable by travel time tomography alone (e.g., Olsson *et al.* [1992]; Valle *et al.* [1999]; Peterson [2001]; Zhou & Fullagar [2001]; Chen *et al.* [2001]; Tronicke *et al.* [2004]; Paasche *et al.* [2006]). However, to the best of our knowledge attenuation tomography has yet not been applied to VRP data, although crosshole and VRP surveying are conceptually identical and the same physical principles

apply. As noted by Tronicke *et al.* [2004], the most important limitation of GPR attenuation tomography is clearly rooted in its inherent assumption of weak heterogeneity, which implies negligible ray bending, no scattering, reflection or refraction effects, and largely undistorted full-space antenna radiation patterns. As these assumptions are rarely fulfilled, the absolute values of the inferred electrical conductivity may differ substantially from the actual values, but the method has nevertheless been proven to be useful and reliable for outlining the larger- scale conductivity structure as well as for constraining relative changes in conductivity (Holliger *et al.* [2001]).

Here, we invert maximum first-cycle amplitudes picked from one selected common transmitter gathers using a linearized inversion approach under the assumption of straight ray paths to obtain a first-order guess of the attenuation and electrical resistivity structure, respectively. Prior to inversion, we correct the picked amplitudes for geometrical spreading, the source strength (estimated amplitude of transmitted wavelet), and the angular sensitivity of the transmitting and receiving antenna (assuming a co-polarized VRP radiation pattern; Tronicke & Knoll [2005]). This data pre-processing follows the standard data reduction procedure known from crosshole GPR attenuation tomography (Olsson *et al.* [1992]; Holliger *et al.* [2001]; Peterson [2001]; Zhou & Fullagar [2001]). The result of inversion is a 1D model of the attenuation of electromagnetic waves, which can be used to estimate electrical resistivity.

4.3.4 Reflection imaging

In addition to inverting direct arrival traveltimes and amplitudes, we may also analyze primary reflections recorded in VRP data as up-going events; i.e., the taveltime of these events decreases with increasing receiver depth (see also Fig. 4.1). Although the principles and the basic processing flows for VRP reflection imaging can largely be adapted from VSP surveying (Böniger *et al.* [2006]), reflection events are often ignored in VRP applications. Here, we use a basic processing flow well known from VSP reflection imaging (e.g., Hardage [2000]) to obtain a 1D reflection image from a single offset data gather. In this flow, after aligning the data (flattening on picked first arrival times) and amplitude scaling, the up-

and down-going wavefields are separated using median filtering or other wave separation techniques such as $f-k$ or Karhunen-Loève filtering. The separated up-going events are shifted back using the doubled first-arrival times resulting in a section where the up-going events are imaged as a function of two-way traveltime (comparable to surface GPR reflection data). Finally, a so-called corridor stack is performed; i.e., the traces are summed in a user-specified corridor placed immediately behind the first arrivals. In doing so, a narrow corridor focusing on reflected signals just behind the direct arrivals helps to suppress multiple reflections. The resulting corridor stack is a single-trace VRP reflection section outlining subsurface boundary layers close to the borehole, which can be used as a direct link to surface-based GPR reflection data.

4.4 Field data

4.4.1 Site description and borehole data

VRP and surface-based GPR reflection data have been acquired at the Horstwalde test site, which is located ∼30 km south of Berlin, Germany, and covers area of ∼70×80 m. The site has been installed by the University of Potsdam in cooperation with the Federal Institute for Materials Research and Testing (BAM) and the Helmholtz Center for Environmental Research (UFZ) to develop techniques for characterizing near- surface sedimentary environments (Tronicke *et al.* [2012]). As known from various boreholes, direct-push soundings, and geophysical surveys, the local, near-surface geology is dominated by layered sequences of mainly sand- and gravel-dominated glaciofluvial material (Linder *et al.* [2010]; Schmelzbach *et al.* [2011]; Tronicke *et al.* [2012]).
In this study, we focus on one ∼18 m deep, PVC-cased borehole in the southern part of test site, where, as known from water leveling, the groundwater table was located at a depth of ∼2.75 m during the time of our VRP and GPR surveys.

Furthermore, the results of sieve analyses of core material are available (Fig. 4.2a) and the borehole has been logged using standard geophysical borehole tools including a deviation (DEV), a natural gamma ray (GR), and an induction tool (IND). From the DEV log (not shown here), we know that the borehole is almost

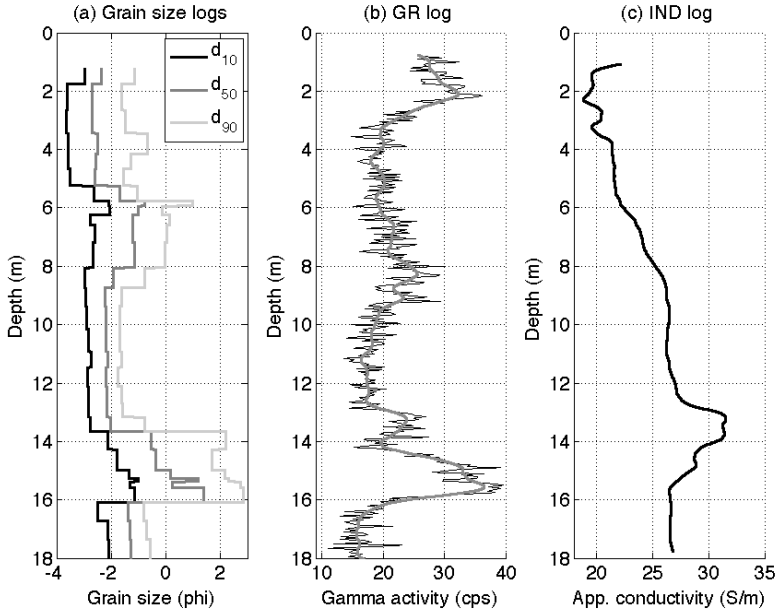

Figure 4.2: Available borehole data at our field site. (a) Characteristic grain sizes d_{10}, d_{50}, and d_{90} derived from sieve analyses of core material, (b) natural gamma activity, and (c) apparent electrical conductivity recorded using standard gamma ray (GR) and induction (IND) tools. In (a), the characteristic grain sizes are plotted in phi-units, where $\mathsf{d(phi)} = -log_2[\mathsf{d(mm)}]$ (e.g., Schön [1998]). In (b), GR raw (black line) and smoothed data (gray line) are shown to highlight major parameter variations.

vertical because the maximum total deviations from verticality are ∼0.1 m. The GR and IND logs (Fig. 4.2b and Fig. 4.2c) measuring natural gamma activity and apparent electrical conductivity, respectively, are standard tools to explore sedimentary units around a borehole (Hearst *et al.* [2000]). Our GR and IND logs as well as the results of grain size analyses indicate different sedimentary units varying in physical properties and composition, respectively. Later on, we use these data to evaluate and to interpret the results of VRP and GPR surveying in more detail.

4.4.2 VRP data

VRP data have been acquired employing two dipole borehole antennas with a nominal center frequency of 100 MHz. The dominant frequencies of the data recorded using a sampling interval of 0.19 ns and 16 vertical stacks were ∼80 MHz. Following the recommendations of Tronicke & Knoll [2005], we recorded multi-offset data with borehole offsets ranging between 1.5 m and 12.0 m with a receiver

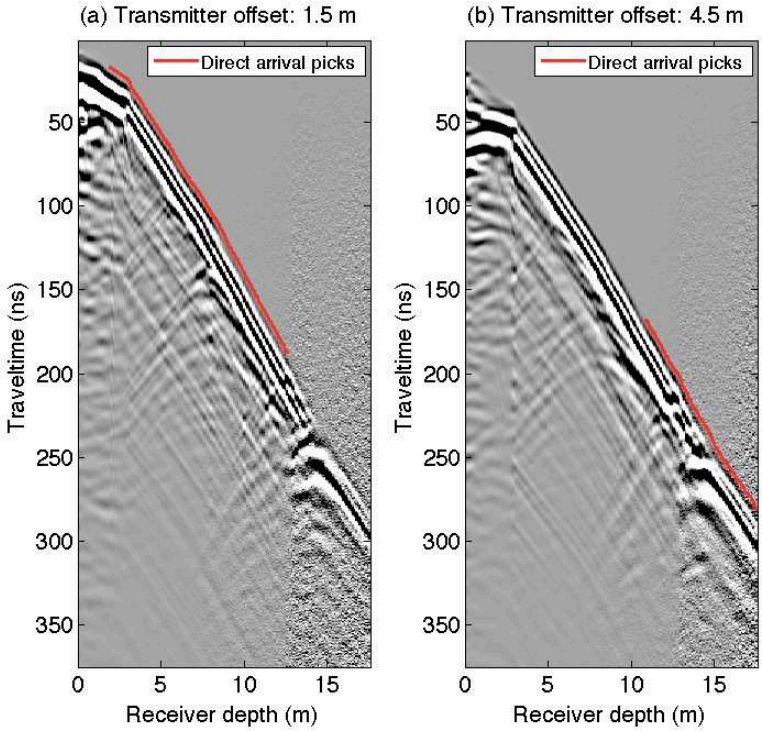

Figure 4.3: Two common transmitter gathers of the Horstwalde VRP field data set recorded at transmitter offsets of (a) 1.5 m and (b) 4.5 m. Offsets are measured between the borehole head and the feedpoint of the antenna. Overlain red curves show picked traveltimes of direct arrivals used as input data for traveltime inversion. The groundwater table measured by water leveling is at a depth of ∼2.75 m and related to a distinct change in the slope of first arrivals. In both transmitter gathers, also numerous reflected (up-going) events can be recognized (see also Fig. 4.1). Both gathers are plotted using the same amplitude scaling.

station spacing in the borehole of 0.1 m.

For traveltime inversion, we restrict our analyses to two common transmitter gathers recorded at offsets of 1.5 m and 4.5 m because the quality of these rather near- offset data gathers allows us to reliably pick traveltimes across the entire depth range of the borehole. In Fig. 4.3, these transmitter gathers are plotted after some fundamental processing together with the picked first arrival traveltimes. Processing included zero- time correction, gentle high-pass filtering (for DC removal and dewowing), amplitude scaling (using the scaling function $t_{1.2}$, where t is traveltime), and amplitude balancing (division of each trace by the root-mean-square amplitude value of the trace to account for amplitude decay with depth). In the 1.5 m offset gather, data quality allows for picking arrival times up to a depth of 12.6 m while in the 4.5 m gather we were able to pick

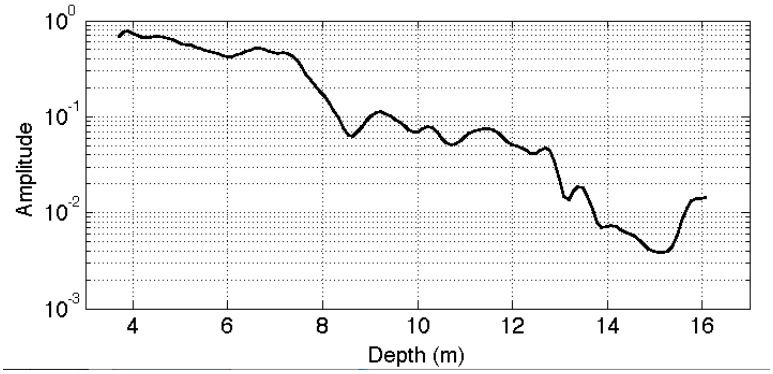

Figure 4.4: First arrival maximum-cycle amplitudes picked from the 1.5 m offset VRP transmitter gather (Fig. 4.2a). Plotted amplitudes are corrected for geometrical spreading, source strength, and the angular sensitivity of the transmitting and receiving antenna.

arrival times up to the maximum receiver depth of 17.6 m. We excluded picks from traces recorded at depths <1.9 m (1.5 m offset) and <10.9 m (4.5 m offset), because in the corresponding depth ranges critically refracted arrivals are likely to interfere with the direct arrivals (see also Tronicke & Knoll [2005]). The time picks visualized in Fig. 4.3 are the input data for our global traveltime inversion approach outlined above; i.e., from these data we calculate an ensemble of possible solutions (1D velocity models) explaining our traveltime data equally well.

To extract further information regarding subsurface properties and architecture from our VRP data set, we also analyze direct-arrival amplitudes and primary reflection events. For the amplitude inversion, we focus on the 1.5 m offset gather (Fig. 4.3a). For receiver depths between 3.4 m and 16 m, amplitudes were picked after applying a gentle bandpass filter (passband between 50 and 225 MHz) to the raw data. As the groundwater table (located at a depth of ~2.75 m) causes major distortions of the recorded signals, we restrict our analysis to traces recorded in the saturated zone. In Fig. 4.4, we show the picked amplitudes after geometrical spreading, source strength, and radiation pattern corrections. Characteristic changes in the slope of this plot already indicate different regimes of amplitude losses which can be related to changes in electrical conductivity in the corresponding depth intervals. To quantify attenuation and to estimate changes in electrical resistivity, respectively, we invert the plotted amplitude values using the inversion strategy outline above.

For reflection imaging, we also focus on the 1.5 m offset gather (Fig. 4.3a), where

a number of reflection events are clearly visible as up-going events over the entire depth range. Using a standard VSP corridor stack processing flow (as discussed above) with a corridor window length of 95 ns, allows us to derive a single-trace reflection image in the immediate vicinity of the borehole. The resulting VRP derived reflection image can be compared to surface-based GPR reflection data and, thus, provides a direct link between borehole- and surface-based geophysical surveying.

4.4.3 Surface-based GPR data

In addition to borehole-based geophysical data, also surface-based GPR reflection data are available. These constant-offset 2D GPR data have been recorded employing a kinematic surveying strategy (relying on the combination of a standard GPR instrument with an auto-tracking total station; Böniger & Tronicke [2010]), using a sampling interval of 0.2 ns, and standard dipole antennas with a nominal center frequency of 100 MHz. The data are processed applying a standard flow including dewow and bandpass filtering, amplitude scaling (relying on a combination of a t_2 and an exponential scaling function), and $f-k$ filtering applied to suppress steep events associated with the tails of diffraction hyperbolas caused by buried pipes and other near-surface scatterers. Finally, the data are migrated using a velocity model as derived from VRP data analysis. In Fig. 4.5, we show the processed data. The profile illustrates that the subsurface around the borehole is characterized by horizontal to sub-horizontal layering with some major, continuous reflection events at ∼50 ns, ∼150 ns, ∼230 ns, and ∼370 ns.

4.5 Results and interpretation

4.5.1 Velocity models

In Fig. 4.6, we show the results of globally inverting our VRP traveltime data (Fig. 4.6) and compare them to one selected independent borehole log (GR log). Before analyzing these results in more detail, we evaluate the chosen model parameterization and the representativeness of the final ensemble by performing an

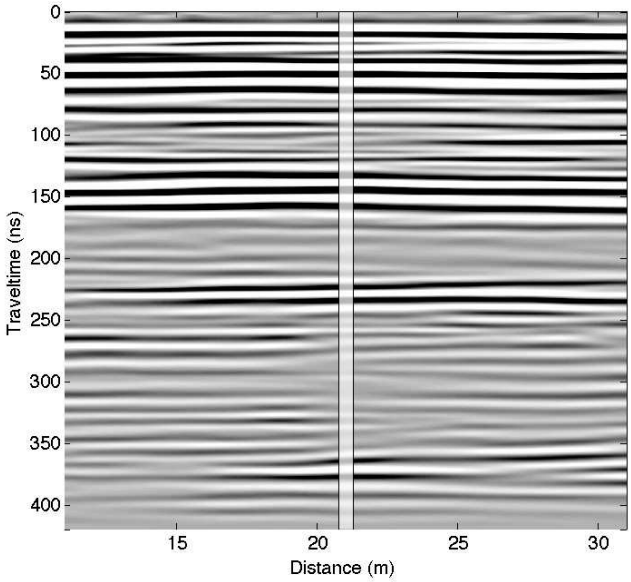

Figure 4.5: Processed 2D GPR profile recorded using a pair of 100 MHz antenna. The transparent rectangle in the center of the profile indicates the position of the borehole where borehole logs (Fig. 4.2) and VRP data (Fig. 4.3) are available.

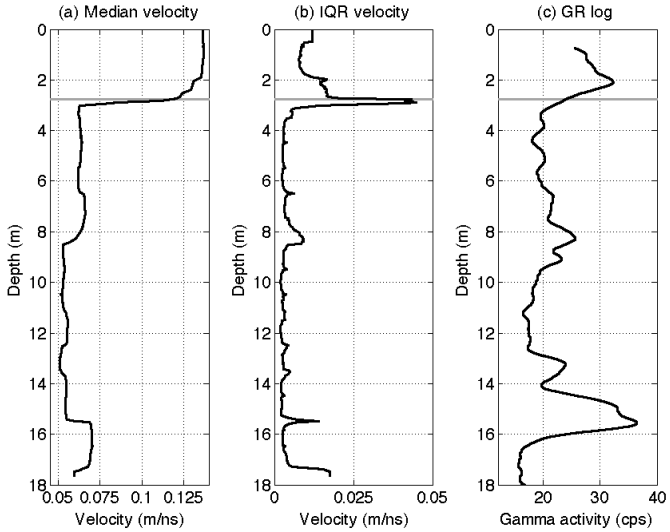

Figure 4.6: Results of globally inverting VRP traveltime data. (a) Median velocity and (b) interquartile range model both calculated from the final ensemble consisting of 210 1D velocity models. (c) Smoothed natural gamma activity log (Fig. 4.2b) for comparison. In (a), (b), and (c), the gray horizontal lines indicate the position of the groundwater table as measured by water leveling in the borehole.

a posteriori correlation analysis of the model parameters following Sen & Stoffa [1995]. In Fig. 4.7a, we illustrate the posterior correlation matrix ($\mathbf{P}$) of the model parameters calculated from the final ensemble consisting of 210 velocity

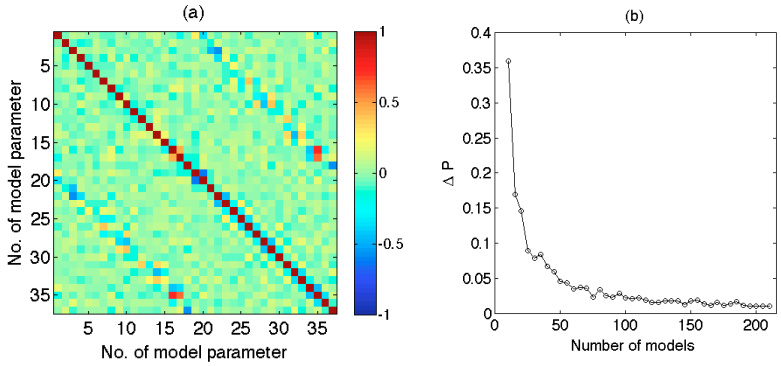

Figure 4.7: (a) Posterior model parameter correlation matrix calculated from the final ensemble consisting of 210 velocity models. Parameters 1 to 18 correspond to depths of interfaces and 19 to 37 to layer velocities. (b) Standard deviation of the differences of correlation matrices (ΔP) when increasing the number of models. Symbols indicate computed differences each time five new models are added to the ensemble.

models. Here, values close to unity, indicate that the corresponding model parameters are strongly correlated and nearly linearly dependent, whereas values close to zero indicate weak linear dependencies. Some higher absolute values in **P** (between ∼0.3 and ∼0.6) are observed between the velocities of neighboring layers (higher values around the main diagonal for parameters 19 to 37) as well as between the depths of interfaces and the velocities of neighboring layers (diagonal patterns parallel to the main diagonal in Fig. 4.7a). This indicates that the corresponding model parameters are not fully resolved; i.e., we only resolve some linear combinations of these parameters and we have to be aware of some nonuniqueness in our results. To evaluate the representativeness of our final ensemble, we analyze differences in **P** at different stages of the ensemble generation. In Fig. 4.7b, we show the standard deviations of the calculated differences each time five models are added to the ensemble. In this plot, the convergence to a low value indicates that only minor variations in the correlation matrix are expected when further models are added to the ensemble. Thus, we assume that our final ensemble is representative and allows for reliable posterior statistical analyses.

In Fig. 4.6a and Fig. 4.6b, we show the median and the interquartile range (IQR) calculated from the generated ensemble of 210 velocity models. These two robust statistical measures are used to reduce the ensemble information to two statistical parameters characterizing the central tendency and the spread of the underlying velocity distributions. The median velocity model (Fig. 4.6a) shows

velocity variations between ∼0.06 m/ns (for the water-saturated sediments) and ∼0.13 m/ns (for the unsaturated sediments). The groundwater table is associated with a sharp decrease in velocity at a depth of ∼2.8 m, which corresponds well to the depth of 2.75 m as measured by water leveling in the borehole. In the saturated zone, further characteristic velocity variations between ∼0.05 m/ns and ∼0.07 m/ns are evident. When comparing these variations to the available borehole logs (Fig. 4.2 and Fig. 4.6c), we notice that the derived velocity variations largely coincide with characteristic changes in grain size, apparent conductivity, and gamma activity. This indicates that the inverted GPR velocities reflect changes in the composition and the physical properties of the sediments, respectively. The IQR of the velocity ensemble (Fig. 4.6b) can be interpreted as an estimate of uncertainty; i.e., increased IQR values identify depth ranges where we have lower confidence in the inverted velocity values. This plot illustrates that maximum uncertainties are found around the groundwater table and the average uncertainties in the unsaturated zone are higher than in the saturated zone (∼0.012 m/ns compared to ∼0.003 m/ns). Focusing on the saturated zone, we further recognize that all major velocity variations (associated with bounding surfaces) show local maxima in the IQR values, which provides some insights into resolution capabilities of our data set. In conclusion, our global traveltime inversion approach results in detailed information regarding subsurface velocity variations including quantitative estimates of uncertainty. In the following, we use the entire ensemble of velocity models in a petrophysical translation framework, which allows us to evaluate the uncertainties in estimated porosities.

4.5.2 Porosity estimation

In hydrological applications, one major purpose of GPR surveying is to estimate water content and porosity for the unsaturated and saturated zone, respectively. Generally, this is done by employing a two-step procedure. First, under the assumption of low-loss, non-magnetic media GPR velocities v are converted to relative permittivity ε_r values using

$$\varepsilon_r = \frac{c^2}{v^2}, \tag{4.1}$$

where c is the electromagnetic velocity in free space. Second, water content or porosity are estimated from ε_r values using an appropriate petrophysical translation. A number the of different petrophysical models have been proposed in the literature (for a recent review see Steelman & Endres [2011]). Here, we use two of the most commonly applied relationships to estimate porosity in the water-saturated zone; i.e., the empirical equation of Topp *et al.* [1980] and the complex refractive index model (CRIM; Wharton & Best [1980]). For a fully saturated medium, Topp's equation can be written as

$$\Phi = 5.3 \times 10^{-2} + 2.92 \times 10^{-2}\varepsilon - 5.5^{-4}\varepsilon^2 + 4.3^{-6}\varepsilon^3, \tag{4.2}$$

where Φ is the porosity of the medium. For a two-phase system consisting of a solid and a water phase, the CRIM model reduces to

$$\Phi = \frac{\sqrt{\varepsilon_r - \varepsilon_r^m}}{\varepsilon_r^w + \varepsilon_r^m}, \tag{4.3}$$

where ε_r^m and ε_r^w are the relative permittivity values of the dry matrix and water, respectively. While equation 4.2 assumes that changes in permittivity are only related to changes in the amount of water, equation 4.3 explicitly considers the permittivity of the matrix material.

To estimate Φ from VRP velocity, we use the entire ensemble of possible velocity models found by our global inversion approach; i.e., each velocity model is translated using the above outlined procedure resulting in an ensemble of possible porosity distributions. While equation 4.2 is a unique translation, we have to specify an appropriate value when using equation 4.3. At our field site, we may use $\varepsilon_r^m = 4.6$, which is a typically used value for clay-free sand and gravel deposits (e.g., Knoll & Clement [1999]). However, due to changes in the mineralogical composition or minor fractions of clay ε_r^m may vary. To investigate the impact of uncertainties in a priori specifying ε_r^m , we also translate our velocity models using a reasonable range of possible ε_r^m values ($3 < \varepsilon_r^m < 6$; e.g., Cassidy [2009a]). We generate an ensemble of 1000 porosity models where, for each porosity model, we randomly select one of the 210 velocity models and combine it with a randomly selected ε_r^m value. In this procedure, both sets of random

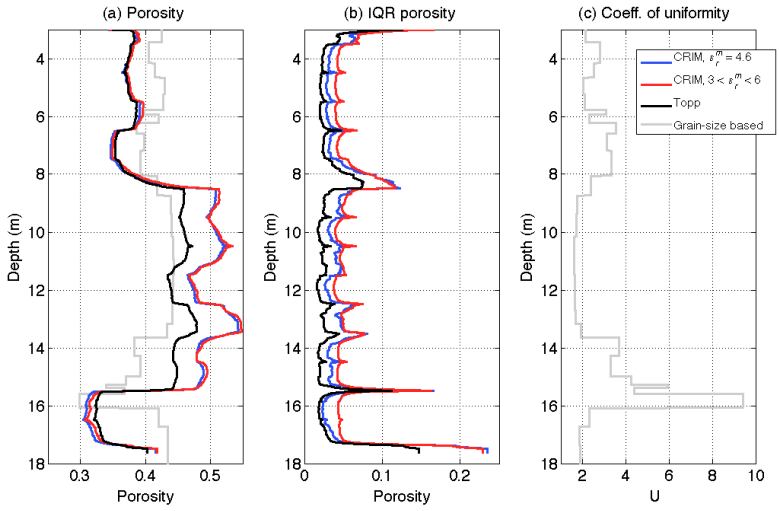

Figure 4.8: Results of estimating porosity for the saturated zone from the VRP velocity model ensemble using different petrophysical models and comparison to independent grain-size based data. (a) Median porosity and (b) interquartile range (IQR) models calculated from the final ensemble of porosity models estimated using the CRIM model (with a fixed ε_r^m value and a variable range of ε_r^m values) and the model of Topp *et al.* [1980]. (c) Coefficient of uniformity ($U = \mathsf{d}_{60}$ / d_{10}) representing grain size data (Fig. 2a) for comparison. In (a), a grain-size based estimate of porosity (gray line) is shown for comparison (calculated after Vukovic & Soro [1992]).

numbers are drawn independently from a uniform distribution. The results of porosity estimation are shown in Fig. 4.8.

In Fig. 4.8a and Fig. 4.8b, we show the median models and the IQR values calculated from the generated ensembles consisting of 210 (Topp and CRIM with $\varepsilon_r^m = 4.6$) and 1000 (CRIM with $3 < \varepsilon_r^m < 6$) porosity models, respectively. All median models indicate the same structures; i.e., a layered subsurface with major porosity variations (> 0.15) at depths of $\sim$8 m and $\sim$15.5 m, which corresponds to areas of major parameter variations also found in the core and logging data (Fig. 4.2). A comparison of the absolute values estimated with equations (4.2) and (4.3) illustrates a good agreement in the lower porosity units (up to $\sim$8 m and below $\sim$15.5 m), while major discrepancies up to $\sim$0.06 are found in the high porosity unit between $\sim$8 m and $\sim$15.5 m. Here, maximum porosities predicted by the CRIM model (>0.5) seem to overestimate porosity. Similar observations have been reported in the literature (e.g., Loeffler & Bano [2004]) and might be related to the fact that the CRIM model relies only on the volume fractions of the constituents without accounting for the geometry of the grains and the pore space, respectively (Endres & Knight [1992]). The IQR porosity values (Fig. 4.8b) can

again be interpreted as estimates of uncertainty. The observed variations are similar to those observed for the IQR velocity values (Fig. 4.6b), where local maxima are found across layer boundaries. When comparing the different petrophysical translations, we notice that the mean uncertainties for Topp's equation (∼0.030) are lower compared to the CRIM-based estimates showing mean IQR values of ∼0.046 (for $\varepsilon_r^m = 4.6$) and ∼0.055 (for $3 < \varepsilon_r^m < 6$). The differences in uncertainty between the two CRIM-based porosity estimates are related to the a priori guesses of ε_r^m , where a fixed ε_r^m = value reduces the degrees of freedom in the petrophysical translation and, thus, results in decreased uncertainty estimates. For comparison, we also show the coefficient of uniformity $U = \mathsf{d}_{60} \,/\, \mathsf{d}_{10}$ (Fig. 4.8c) calculated from the available grain size data (Fig. 4.2a). The higher U the more poorly sorted the sediment is and, thus, we expect decreasing porosity Φ with increasing U. Based on literature data, Vukovic & Soro [1992] developed the empirical relationship $\Phi = 0.255(1 + 0.83)U$, which can be used to roughly estimate Φ from U (gray line in Fig. 4.8a). When comparing this grain-size based estimate of Φ and also Fig. 4.8c with our VRP based models of Φ, we notice an at least qualitative good agreement although the range of the grain-size based Φ values is lower and some major discrepancies are found at depths >∼13 m. Here, we have to consider that the used empirical relationship of Vukovic & Soro [1992] only accounts for variations in the characteristic grain sizes d_{10} and d_{60} and ignores other controlling factors such as grain packing, grain shape, or compaction. In conclusion, our VRP velocity ensemble allows for deriving detailed porosity models including quantitative estimates of uncertainty which are consistent with the available background information from coring and logging.

4.5.3 Attenuation and electrical resistivity

In Fig. 4.9, we show the results of inverting our VRP amplitude data (Fig. 4.4) and compare them to the IND borehole log. Inverted attenuation values (Fig. 4.9a) range between ∼0.12 m^{-1} (in the unsaturated zone) and ∼0.56 m^{-1} (in the saturated zone), which is consistent with literature values reported for sandy sediments (e.g., Cassidy [2009a]). In the following, we restrict our analyses to the saturated zone where amplitude data have been picked. Comparing attenuation

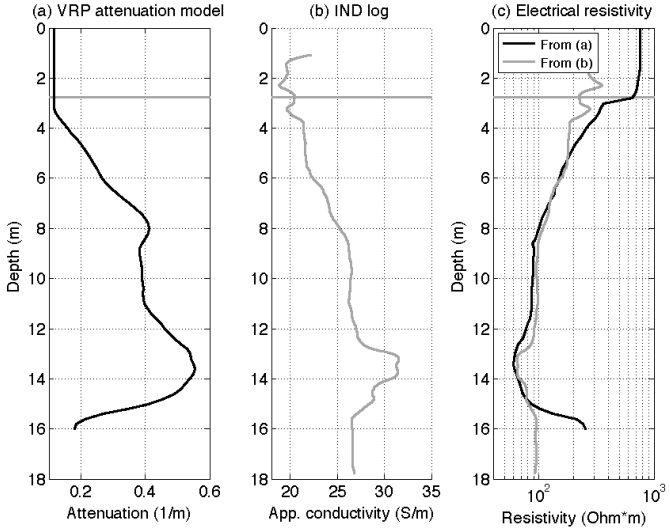

Figure 4.9: (a) 1D attenuation model obtained from inverting VRP amplitudes (Fig. 4.4), (b) apparent electrical conductivity as obtained by induction logging (Fig. 4.2c), and (c) electrical resistivity estimated from (a) and (b). In (a) to (c), the gray horizontal lines indicate the position of the groundwater table as measured by water leveling in the borehole. Note, that apparent conductivity values from (b) have been shifted by minus 16 mS/m before translation to be in the same resistivity range (below the groundwater table) as the resistivity values estimated from VRP results.

to apparent conductivities from the IND log (Fig. 4.9b) illustrates a consistent behavior; e.g., increasing attenuation is paired with increasing conductivities and maximum attenuation is found in depth intervals of maximum conductivity. Under the assumption of low loss and non-magnetic media, attenuation α can be approximated by

$$\alpha = \frac{194.5}{\rho\sqrt{\varepsilon_r}}, \tag{4.4}$$

where ρ is the electrical resistivity (Davis & Annan [1989]). Using equation (4.4), we estimate ρ from our VRP derived attenuation model and compare it to ρ values derived from IND apparent conductivities. It should be emphasized again that the VRP derived values rely on the inherent assumption of weak heterogeneity and, thus, we do not expect accurate estimates of ρ. Furthermore, the absolute values of IND apparent conductivity should be handled with care (e.g., because they depend on tool calibration). To ensure that both ρ estimates are in the same range (in the saturated zone), we subtracted 16 mS/m from the measured IND values before calculating the reciprocal of IND conductivity. The resulting resistivity models (Fig. 4.8c) are in good agreement because they

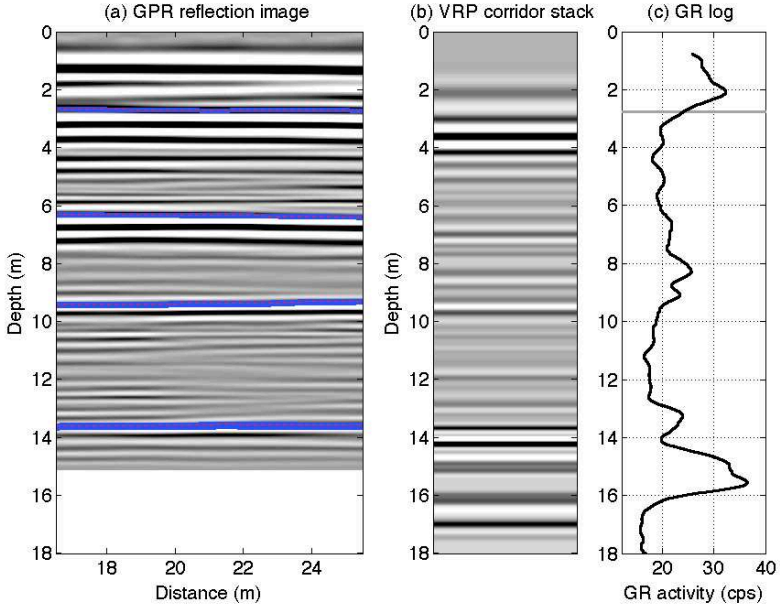

Figure 4.10: Results of reflection imaging after time-to-depth conversion using the median VRP velocity model (Fig. 4.6a). (a) GPR reflection profile around the VRP borehole located at a horizontal distance of 21 m (Fig. 4.5), (b) VRP corridor stack, and (c) smoothed natural gamma activity log (Fig. 4.2b) shown for comparison. In (c), the gray horizontal line indicates the position of the groundwater table as measured by water leveling in the borehole. In (a), the four sets of blue curves represent time-to- depth conversions for four selected reflections using the entire ensemble of VRP velocity models while the dashed red lines represent the conversion using the median model (Fig. 4.6a).

show the same relative resistivity variations. Thus, we can conclude that VRP amplitude inversion can be used for outlining the larger-scale resistivity structure and for constraining relative changes in resistivity, respectively.

4.5.4 Reflection imaging

In Fig. 4.10, we show the surface-based GPR reflection image (Fig. 4.5) and the VRP corridor stack (single-trace reflection image at the borehole) and compare these images to one selected independent borehole log (*GR* log). The reflection images are depth converted using the median velocity model shown in Fig. 4.6a. First, we want to evaluate the influence of the velocity model on time-to-depth conversion using four distinct, continuous reflection events picked in the GPR time section (Fig. 4.5). In Fig. 4.10a, the results of converting the time picks using the VRP median model are illustrated by red lines, while the results using the entire ensemble of 210 velocity models are represented by the four sets of blue

lines. Comparing all of these depth estimates illustrates maximum differences of ∼0.15 m, which demonstrates the consistency and representativeness of the velocity ensemble and the median model, respectively, and also illustrates that only minor uncertainties in depth imaging are expected.
Comparing the reflection images in Fig. 4.10a and Fig. 4.10b demonstrates that both images outline similar subsurface structures. In addition to the four major continuous events highlighted in the surface data (Fig. 4.10a), also some minor, lower-amplitude reflections (such as those at depths of ∼4.5 m and ∼8 m) are found in both images. In addition, the VRP corridor stack shows reflection events at depths >15 m (i.e., beyond the penetration depth of our surface data), which can be explained by the shorter travel paths (lower attenuation) of VRP reflection events compared to the corresponding events in the surface data. When comparing Fig. 4.10a and Fig. 4.10b with the available borehole logs (Fig. 4.10 and Fig. 4.10c), we notice that the imaged structures largely coincide with characteristic changes in grain size, apparent conductivity, and gamma activity.

4.6 Integrated interpretation and discussion

Our VRP results (Fig. 4.6, Fig. 4.8, Fig. 4.9 and Fig. 4.10) can be interpreted in an integrated fashion to develop a detailed understanding of the subsurface in the vicinity of the borehole. While the VRP corridor stack (Fig. 4.10,b) depicts subsurface structures in terms of bounding surfaces, VRP derived estimates of GPR velocity, porosity, and electrical resistivity can be used (in combination with other available borehole data) to characterize the subsurface using a variety of physical properties. Here, we focus on interpreting the structures and parameters below the groundwater table (at depths >2.75 m) as needed for a hydrogeological characterization. In Fig. 4.11a to Fig. 4.11e, we compile our VRP results and compare them to a grain-size based hydraulic conductivity estimate and the available GR log (Fig. 4.11f and Fig. 4.11g). To roughly estimate hydraulic conductivity k_f from our grain-size data, we employ the empirical model $k_f = 0.0045 log_10(500/U)\ \mathsf{d}_1 0^2$ (Beyer [1964]), which, in hydrogeology, represents one popular approach to roughly estimate k_f from grain size data (e.g., Vienken & Dietrich [2011]).

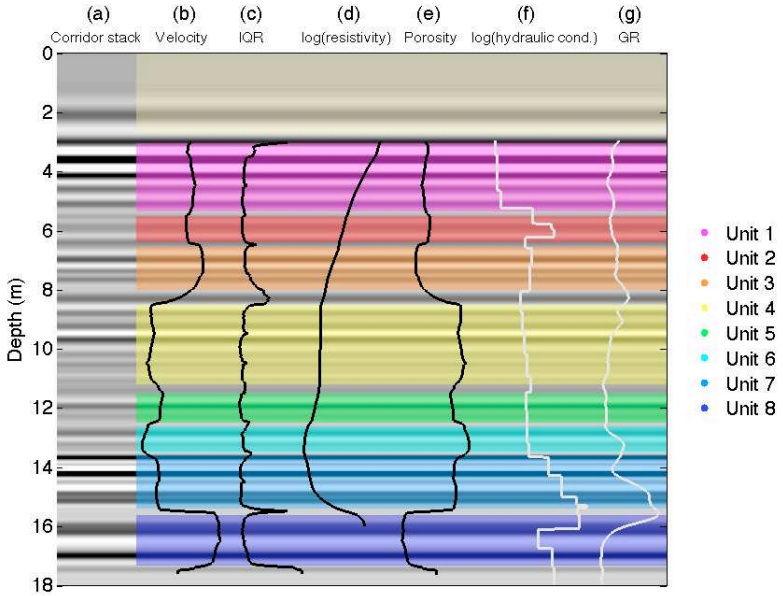

Figure 4.11: Integrated interpretation of VRP results (color coded units 1 to 8) and comparison to selected independent logs for the water-saturated zone (depths >2.75 m). (a) VRP corridor stack (Fig. 4.10b), (b) VRP median velocity model (Fig. 4.6a) including (c) IQR uncertainty estimate (Fig. 4.6b), (d) VRP resistivity model (Fig. 4.9c), (e) VRP median porosity model (calculated using Topp's equation; Fig. 4.8a), (f) hydraulic conductivity estimated from grain-size data (Fig. 4.2a), and (g) smoothed natural gamma activity log (Fig. 4.2b). Parameter models plotted using black lines (b-e) represent VRP derived parameters while gray lines (f-g) refer to independent data logs.

Using our VRP results (including VRP derived parameter models and uncertainty estimates; Fig. 4.11a to Fig. 4.11e), we interpret eight characteristic units (Fig. 4.11h). As illustrated, these units are characterized by distinct parameter combinations and can be distinguished by major changes in VRP derived parameters and reflection events, respectively. For example, units 1 to 3, are characterized by steadily decreasing electrical resistivities paired with changing layer velocities and porosities (ranging from ∼0.061 m/ns to ∼0.066 m/ns and ∼0.35 to ∼0.39, respectively), while the underlying unit 4 is characterized by almost constant resistivities and only minor fluctuation in velocity and porosity. Here, we notice, that the reflection event at a depth of ∼9.5 m is not associated with a major change in velocity, resistivity or porosity. This event, which is also recognized in the surface-based reflection data (Fig. 4.10a), might be related to a thin layer beyond the resolution capabilities of our traveltime and amplitude VRP data. When interpreting the depth ranges of the individual units (Fig. 4.10), we also consider the available uncertainty estimates; i.e., depth intervals

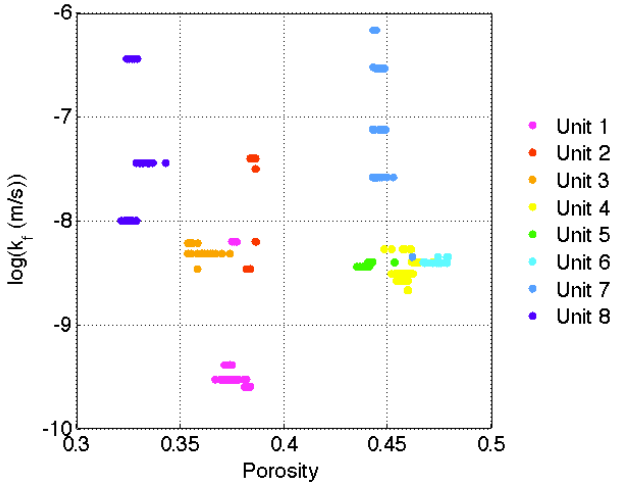

Figure 4.12: Crossplot of porosity versus hydraulic conductivity k_f for the interpreted units (Fig. 11). Porosities are derived from the VRP results (median porosity model calculated using Topp's equation; Fig. 8a) and k_f values are estimated using the empirical model of Beyer [1964]. Color coding corresponds to Fig. 4.11.

between individual units, which show increased IQR values for velocity (and also porosity, Fig. 4.8b) are excluded from the interpretation. In these areas, we have low confidence in our results and can not identify accurately the depths of the corresponding bounding surface.

In Fig. 4.12, we analyze the hydrogeological relevance of the interpreted units in more detail. The shown cross-plot of VRP derived porosity Φ versus hydraulic conductivity k_f illustrates that variations in the grain-size based k_f values are around four orders of magnitude and that we can not expect a general, unique relation between Φ and k_f (e.g., a linear relation between $log(k_f)$ and Φ) at our field site. However, we notice that the interpreted units are characterized by distinct combinations of Φ and k_f. Thus, our VRP based interpretation may serve as a hydrostratigraphic zonation at the borehole location. Furthermore, we can interpret our surface based GPR data considering this zonation. Such an interpretation is shown in Fig. 4.13, where we develop a 2D hydrostratigraphic model around the borehole by extrapolating the borehole-based interpretation on the basis of the structures imaged by surface-based GPR. In doing so, we realize the importance of our VRP results to interpret the rather complex GPR reflection patterns in view of a detailed and meaningful hydrostratigraphic model.

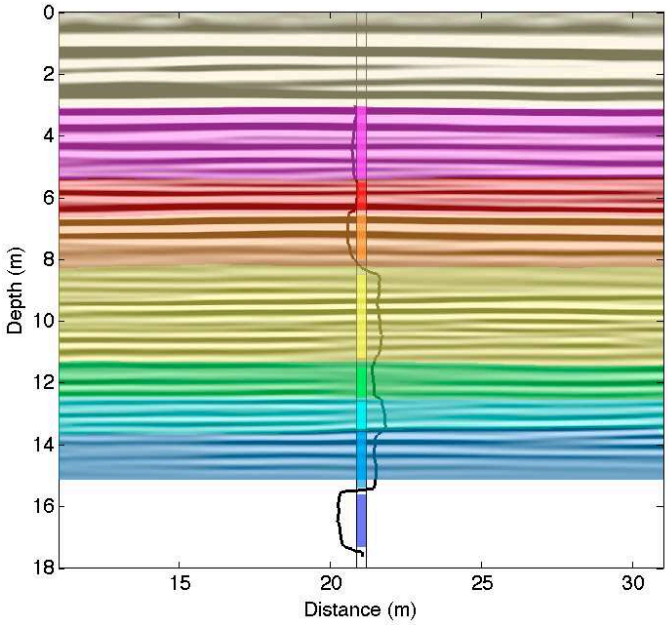

Figure 4.13: Hydrostratigraphic interpretation of processed GPR reflection data (Fig. 4.5) based on the integrated interpretation of VRP results (Fig. 4.11). The borehole is located at a horizontal distance of 21 m the where we also show the units interpreted from VRP results (Fig. 4.11) as well as the VRP median porosity model (Fig. 4.8a). Color coding corresponds to Fig. 4.11 and Fig. 4.12.

4.7 Conclusions

Using field data from a well-constrained test site, we demonstrated the potential of VRP surveying in view of developing a detailed understanding of subsurface architecture and properties. We presented a workflow combining the analysis of VRP traveltimes, amplitudes, and reflections. Inversion of traveltimes and amplitudes allows us to derive models of velocity and attenuation, which can be used to estimate further material properties such as porosity and electrical resistivity. Analyzing VRP reflection events using a standard corridor-stack processing flow adapted from VSP imaging, allows for generating a single-trace reflection image, which highlights bounding surfaces in the studied sedimentary aquifer. Our case study illustrates the benefit of our workflow in view of developing a detailed and meaningful hydrogeological model and interpreting our surface-based GPR reflection profile. All presented VRP based results are consistent with independent core, logging, and surface-based GPR data, which stresses the value of VRP surveying; especially, at field sites where no borehole logs and coring data

are available. As the employed inversion and processing approaches are readily available, the outlined data acquisition, inversion, processing, and interpretation approaches can be easily implemented in near-surface geophysical surveying whenever boreholes are available. In conclusion, this study demonstrates that more than a single velocity profile can be extracted from VRP data and that the derived VRP results can play an important role in linking borehole and surface-based geophysical data sets. Thus, we expect increasing interest and effort of researchers and practitioners towards the usage of VRP surveys and towards the integration of VRP results into multi-method site-characterization studies.

Chapter 5

Thesis Discussion

This chapter is a final discussion related to the entire content of all manuscripts presented in this work and interconnects their individual results to the overall topic of this thesis: Ground-penetrating radar wave velocities and their uncertainties. Different methods are developed and applied to GPR ground waves and reflected waves as measured with CMP data gathers (second and third chapter), and direct waves from VRP data gathers (fourth chapter) to derive subsurface velocity models including robust estimates of uncertainty.

In the three manuscripts (chapter 2-4), velocities are derived with statistical methods and a global optimization method (swarm intelligence; PSO). Semi automated velocity analysis methods are introduced, as variations, combinations and extensions of existing statistical methods to simplify geophysicists work. Thus in the second chapter (surface-based GPR), the statistical coherency measure of semblances is computed between waveforms across data gathers which are corrected with a moveout operation to detect velocity. In the third and fourth chapter global optimization approaches are introduced and successfully used for GPR velocity analysis. In all three published studies, more correct velocities with quantitative uncertainties achieved with statistical methods from distributions are the answer to open research question. Consequently, we give an answer beyond the common understanding of GPR subsurface velocities as discrete values because results are presented as distributions. The resulting distributions will involve information of continues spatial property changes of subsurface. Thus, continues spatial material changes will be reflected in higher uncertainties in all three studies. The

discussions about uncertainties in geophysics continues, but we suggest new practical and robust approaches to do it more quantitatively and objectively.
As it is shown in Figure 1.6 and Figure 1.7 petrophysical laws have different results due to the use of variable formulas and parameters (Jackson *et al.* [1978],Jacobsen & Schjønning [1993], Malicki *et al.* [1996]). In contrast to common calibration of empirical relationships with additional site specific soil sampling the presented quantitative velocity distributions is proposed to be used to optimize petrophysical relationships and further soil information can be extracted (e.g. clay content), as it has been outlined in the integrated interpretation in chapter five. Enhancements of effective medium approximations Sen [1984] with variable shaped grain packings and resulting water and air volumes may be improved with the presented reliable velocities to give the desired understanding of subsurface parameter changes and soil compositions.
Bellow I integrate the presented work into the currant state of the knowledge of the subject of GPR velocity determination. For environmental, archaeological, engineering, and geological applications, GPR is promoted as the adequate tool to image near- surface environments (e.g., Jol [2009b]). GPR surveying combines the advantages of point measurements and remote sensing technologies (e.g., Hillel [1998], Allred *et al.* [2008]), but the resulting increased field data amount is often announced as major limitation and, thus, fast analysis (like ours) of GPR data gathers is needed. To image subsurface structures accurate GPR velocities and uncertainties are required, for migration routines (Greaves *et al.* [1996]; Tillard & Dubois [1995]) and for time-to-depth conversions and elevation corrections (Annan [2005]; Cassidy [2009b]). To obtain velocities from GPR CO gathers isolated objects in the subsurface are needed (e.g., Moore *et al.* [1999]; Bradford & Harper [2005]; Porsani & Sauck [2007]; Schmelzbach *et al.* [2011]), thus we use CMP and VRP.
Multi-offset reflection profiling or common midpoint (CMP) profiling are used to achieve velocity models with methods often adapted from seismic data processing (e.g., Greaves *et al.* [1996]; Brosten *et al.* [2009]; Turesson [2007]; Booth *et al.* [2010]); (Greaves *et al.* [1996]; Cai & McMechan [1999]; Pipan *et al.* [1999]; Becht *et al.* [2006]; Bradford *et al.* [2009]), with critical consequences (chapter 2). Analysis of CMP data is often performed with reflection seismic processing tools

based on the normal-moveout (NMO) model (e.g., spectral velocity analysis; Yilmaz [2001]) assuming small offset-to-depth ratios, small velocity gradients, and plane horizontal reflectors (Al-Chalabi [1973]), what is often not the case in GPR applications. Such CMP-derived velocity estimates have been used for a straight forward characterization of the subsurface and to estimate water content (Greaves *et al.* [1996]). Various studies have elaborated different sources of errors of these velocity estimates for GPR (e.g., Tillard & Dubois [1995]; Jacob & Hermance [2004]; Becht *et al.* [2006]; Booth *et al.* [2010]; Booth *et al.* [2011]) and for seismic processing (e.g., Taner & Koehler [1969]; Levin [1971]; Hajnal & Sereda [1981]; Alkhalifah [1997]; Leparoux *et al.* [2001]; Bradford [2006]). Alternatively, Harper & Bradford [2003] used the least-squares inversion method of Zelt & Smith [1992] to achieve a 1D velocity model from reflection traveltimes, with strong relations of the results to an initial model. Consequently, traveltimes are inverted with swarm intelligence algorithms (PSO) introduced by Kennedy & Eberhart [1995] to solve global optimization problems in various applications (Poli [2008]) and in geophysics (Shaw & Srivastava [2007]; Fernández Martínez *et al.* [2010]; Monteiro Santos [2010]; Tronicke *et al.* [2012]; Wilken & Rabbel [2012]). For this work PSO is combined with a fast marching eikonal solver (Sethian [1996]; Fomel [1997a]; Sethian & Popovici [1999]). What is only a ray-tracing approaches in contrast to FDTD Giannopoulos [2005], but sufficient fast for required high amount model generation for PSO. We only consider planar layer models to demonstrate feasibility of PSO.

Direct ground wave (DGW) velocity can be estimated for the uppermost soil layer from the steepness of manually fitted straight line through interpreted ground wave arrivals in CMP data gathers (e.g., Huisman *et al.* [2001]; Huisman *et al.* [2003]; Galagedara *et al.* [2005a]; Steelman & Endres [2010]). For this problem we developed and succeeded with the application of an objective, reproducible and fast method based on moveout semblance analysis. The presented method is not able to detect ground wave events in the case of perturbing phenomena, like interferences with other waves (shallow reflected, lateral, critically refracted and air) and dispersive behavior of material (Grote *et al.* [2010]); Galagedara *et al.* [2005b]; Yi & Endres [2006] and van der Kruk *et al.* [2009]).

Crosshole imaging (Binley *et al.* [2001]; Allumbaugh *et al.* [2002]; Tronicke *et al.*

[2002]; Tronicke *et al.* [2004]; Becht *et al.* [2004]; Clement & Barrash [2006]; Gloaguen *et al.* [2007]; Looms *et al.* [2008]) requires typically small lateral distances of boreholes ($\sim 10\,\mathrm{m}$). The best resolution can be expected in the center between the boreholes (e.g., Rector & Washbourne [1994]; Day-Lewis *et al.* [2005]) which hinders the linking of petrophysical models to material properties derived from logging data form the boreholes.

Thus, we analysis vertical radar profiling data which can provide more information about subsurface velocity variations in the vicinity of a borehole (Knoll [1996]). Furthermore, we use VRP technique in Chapter 5 for reflection imaging (Zhou & Sato [2000]; Böniger *et al.* [2006]) and 1D attenuation tomography, what can not be done with crosshole imaging. In contrast to linearized inversion schemes of direct traveltimes of VRP (Knoll & Clement [1999]; Murray *et al.* [2000]; Hammon *et al.* [2002]; Pringle *et al.* [2003]; Cassiani *et al.* [2004]; Böniger *et al.* [2006]; Spillmann *et al.* [2006]; Cassiani *et al.* [2008]; Harbi. & McMechan [2011]; Schmelzbach *et al.* [2011]; Vignoli *et al.* [2012]; Igel *et al.* [2013]). we use PSO, to be independent from initial parameter models, be able to achieve multiple solutions and to generate representative ensembles of solutions.

Many hydrological applications require detailed information about spatial and temporal variations of soil water content and it has been shown that GPR surveying is highly efficient to monitor soil water content at the field scale (e.g. Huisman *et al.* [2003]). We developed precise and fast methods to derive velocities from GPR to enhance the estimation of water content, porosity or other soil parameters (e.g.,Topp *et al.* [1980]; Heimovaara *et al.* [1994]; Greaves *et al.* [1996]; Van Overmeeren *et al.* [1997]; Huisman *et al.* [2003a]; Tronicke *et al.* [2004]; Steelman & Endres [2012]; Hamann *et al.* [2013]). The permittivities in volumetric mixing models introduced in the petrophysical relationships, normally taken from soil probing, or literature, may be optimized with the velocities determined with presented methods to obtain information of the dry matrix.

Chapter 6

Overall Summary and Conclusions

All three proposed methods are tested on synthetic data examples to evaluate influence of different kind of waves and antenna setups on the accuracy of estimated wave velocities and subsequent soil water content estimates from established petrophysical relationships. Furthermore, successful analysis of field data are presented from different test sites in Canada and Germany to observe spatial and temporal soil moisture variations. A comparison between our velocity estimates and independent data shows good agreement, which illustrates that the proposed methods for velocity analysis are feasible tools to analyze velocities from GPR data gathers in objective and reproducible ways.

The second chapter (first manuscript) deals with the examination of a direct ground wave (DGW) velocity analysis approach based on velocity spectra computed using a linear moveout model (LMO). The use of such an approach is reasonable because velocity spectra analyses are well established for reflection hyperbola detection using the normal moveout method (NMO). The LMO based spectral velocity analysis method is proposed to estimate DGW velocities from multi-offset GPR data. In contrast, common practice is typically based on manually fitting DGW arrivals, our method represents an objective and reproducible approach of DGW velocity analysis. Furthermore, it can be used to quantify uncertainties in determining DGW velocities by measuring the width of the maxima

in the calculated velocity spectra. This allows us to analyze uncertainties related to survey design and subsurface conditions. The results from synthetic models have demonstrated that the DGW velocity and their uncertainty determination depends on the real subsurface velocity distribution, the antenna frequency, the offset range and the maximum offset used in the analysis. Typical surveying parameters and signal frequencies, resulted in relative errors in velocities of more than 5%, resulting from the evaluation of corresponding uncertainties from peak widths at 90% of maximal coherence value in velocity spectra. Thus, I point out that this method allows a more objective and reproducible analysis of DGW velocity in contrast to common practice, which is largely based on manually fitting DGW arrivals. This is of major importance for field applications and has to be considered when DGW velocities are translated into water content. The results from synthetic data indicated additionally that the relative error in water content increases exponentially with decreasing water content when Topp's equation is used under the assumption of low loss soil conditions. To demonstrate the applicability of our approach to real data, LMO based velocity spectra have been calculated for field data collected across a silt loam soil at a well-constrained field site in Canada. It was shown, that the estimated velocities produce shows similar water content results compared to the common analysis practice. With this proposed processing sequence the spectral velocity analyses can be performed in a largely automated and reproducible manner. This automated procedure allows the effective analysis of large data sets which is of great value, especially, for long-term monitoring experiments. The comparability of the results to manual analyses of the available CMP gathers illustrates that the detected velocity values and seasonal variations are reasonable. Because of eliminating the influence of a manual data analysis procedure, the spectral velocity method is a rather objective tool to derive and analyze DGW velocities including quantitative uncertainties. This is supported by a similar behavior of derived velocity uncertainties from spectral analyses of field and synthetic data gathers, where comparable tendencies are observable under varying soil velocities, antenna frequencies, and maximum antenna offsets. Thus, the feasibility of deriving ground wave velocities from CMP gathers is improved, and the proposed strategy can be readily applied in various GPR application including the time-lapse monitoring

of soil water content.

For processing of GPR common offset data, CMP surveys are often acquired to obtain 1D velocity models at selected locations across a field site. For such CMP application a global inversion approach based on particle swarm optimizarions (PSO) is proposed to analyze reflection traveltimes using a layer-based model parametrization. The developed global inversion strategy employs a forward modeling routine which accounts refraction effects and, thus, avoids the inherent assumptions of NMO based velocity analysis. The velocities show different results to conventional technique because we avoid the small offset approximation. In contrast to local (linearized) inversion approaches, the used global optimization approach generates results independent of an initial model, allows for a lager model space and the algorithm to converge to multiple solutions of an ill-posed problem. Furthermore, such global approaches enable us to generate a representative ensemble of models that explain the data equally well and, thus, can be used to assess uncertainty and non-uniqueness issues in the formulated inverse problem. Such representative ensembles allow the analysis of the interdependency between different model parameters. Correlations are observed within neighboring parameters (layer thicknesses and velocities) which are the limitations to accurately estimate velocity and depth of the corresponding interface. Different statistics of the generated ensemble can be used to evaluate the tendency and the variability of the individual model parameters. The median, the 25th to 75th, and the 5th to 95th percentile of the parameter distributions are chosen after tests to characterize the resulting parameter distributions and to estimate reliable uncertainties. Decreasing velocities with increasing depth, which, for example, are typical for GPR CMP gathers recorded across the groundwater table, decrease the accuracy of the model parameters for deeper layers. PSO based inversion approaches are easy to implement, needs minimal effort of parameter tuning, and provide faster convergence compared with other global optimization approaches (e.g., simulated annealing methods). Thus, the presented methodology is promoted as a feasible and powerful instrument to analyze GPR CMP data. Furthermore, such approaches allow for a quantitative evaluation of uncertainties which is important for successful CO data processing and for establishing a reliable, meaningful and successful connection to borehole logging data. In the shown field data example

velocities values agree with structures from independent data such as direct push friction ratio and natural gamma activity borehole logging data.
The field study shown in the last chapter, demonstrates the possibility to develop a detailed understanding of subsurface architecture and properties from VRP surveying. The proposed workflow is a combination of the analysis of VRP traveltimes, amplitudes, and reflections. Inversion of traveltimes and amplitudes allows the derivation of models for velocity and attenuation, which can be used to estimate further material properties such as porosity and electrical resistivity. The global optimization approach of chapter three is modified to invert direct-arrival traveltimes from VRP surveys to continuous 1D velocity models including quantitative uncertainty estimates. Analyzing VRP reflection events using a standard corridor-stack processing flow adapted from VSP imaging, allows to obtain the reconstruction of a single-trace reflection image, which indicates sedimentary bounding surfaces in the studied saturated zone. This exemplary study illustrates the advantage of the proposed analysis and processing strategy concerning the development of a detailed and reliable hydrogeological model regarding the interpretation of surface-based GPR reflection profiles. All presented results from VRP data are comparable with independent borehole logging and surface-based GPR data, what motivates the use of VRP surveying as a valuable exploration tool even if no borehole logs and core data are available. Whenever boreholes are available the outlined data acquisition, inversion, processing, and interpretation approaches are an enhancement of geophysical surveying. Other parameter profiles than a single velocity model can be extracted from VRP data and derived VRP results can be the linkage of borehole and surface- based geophysical data sets. Hence, integration of VRP results into multi-method site-characterization studies and an increasing interest and effort of scientists and applicators towards the usage of VRP surveys is desired.
In this thesis, three methods are developed which show improved results for electromagnetic propagation velocities and their uncertainties from GPR data.
Comparison of results from tests on synthetic and real GPR field data to results of standard approaches for velocity and soil parameter estimations approve their accuracy. Velocities are subsequently usable for soil water content estimates with established petrophysical relationships. Field data are analyzed, from different

test sites in Canada and Germany to detect realistic variations of soil moisture and other parameters and, thus, our results underline the advantage of the three new presented strategies to investigate velocities from GPR data.

References

Al-Chalabi, M. (1973). Series approximation in velocity and traveltime computations. *Geophysical Prospecting*, **21**, 783–795. 32, 79

Alkhalifah, T. (1997). Velocity analyses using nonhyperbolic moveout in transversely isotropic media. *Geophysics*, **62**, 1839–1854. 32, 79

Allred, B., Daniels, J. & Ehsani, M. (2008). *Handbook of agricultural geophysics*. CRC Press. 1, 14, 78

Allumbaugh, D., Chang, P.Y., Paprocki, J., L.and Brainard, Glass, R. & Rautman, C. (2002). Estimating moisture contents in the vadose zone using cross borehole ground penetrating radar: a study of accuracy and repeatability. *Water Resources Research*, **38**, 1309. 53, 79

Annan, A. & Cosway, S. (1992). Ground penetrating radar survey design. In *AGEEP, Symposium on the Application of Geophysics to Engineering and Environmental Problems*, vol. 5, 329–352. 5

Annan, A.P. (2005). Ground-penetrating radar, near surface geophysics. *Butler D.K. SEG*, 357–438. 16, 31, 32, 34, 78

Annan, A.P. (2009). *Electromagnetic principles of ground penetrating radar*, vol. 1. Elsevier. 1

Aster, R., Borchers, B. & Thurber, C. (2013). Parameter estimation and inverse problems. *Academic Press*. 33

Becht, A., Tronicke, J., Dietrich, P. & E., A. (2004). Inversion strategy in crosshole georadar tomography using information of data subsets and residual analysis. *Geophysics*, **69**, 222–230. 53, 80

Becht, A., Appel, E. & Dietrich, P. (2006). Analysis of multi-offset GPR data: A case study in a coarse-grained gravel aquifer. *Near Surface Geophysics*, **4**, 227–240. 32, 33, 78, 79

Beyer, W. (1964). Zur Bestimmung der Wasserdurchlässigkeit von Kiesen und Sanden aus der Kornverteilungskurve. *Wasserwirtschaft Wassertechnik*, **14**, 165–168. 72, 74

Binley, A., Winship, P., Middleton, R., Pokar, M. & West, J. (2001). High-resolution characterization of vadose zone dynamics using cross-borehole radar. *Water Resources Research*, **37**, 2639–2652. 15, 32, 53, 79

Bjelm, L., Follin, S. & Svenssoni, C. (1982). A radar in geological subsurface investigation. *Bulletin of the International Association of Engineering Geology-Bulletin de l'Association Internationale de Géologie de l'Ingénieur*, **26**, 175–179. 3

Böniger, U. & Tronicke, J. (2010). On the potential of kinematic GPR surveying using a self-tracking total station: Evaluating system crosstalk and latency. *IEEE Transactions on Geoscience and Remote Sensing*, **48**, 3792–3798. 2, 63, 102

Böniger, U., Tronicke, J., Holliger, K. & Becht, A. (2006). Multi-offset vertical radar profiling for subsurface reflection imaging. *Journal of Environmental and Engineering Geophysics*, **11**, 289–298. 53, 58, 80

Booth, A., Linford, N., Clark, R. & Murray, T. (2008). Three-dimensional, multi-offset GPR imaging of archaeological targets. *Archaeological Prospection*, **15**, 1–20. 33

Booth, A., Clark, R., Hamilton, K. & Murray, T. (2010). Multi-offset ground penetrating radar methods to image buried foundations of a medieval

town wall, Great Yarmouth, UK. *Archaeological Prospection*, **17**, 103–116. 15, 32, 78, 79

Booth, A., Clark, R. & Murray, T. (2011). Influences on the resolution of gpr velocity analyses and a Monte Carlo simulation for establishing velocity precision. *Near Surface Geophysics*, **9**, 399–411. 17, 22, 32, 79

Bradford, J. (2006). Applying reflection tomography in the postmigration domain to multifold ground-penetrating radar data. *Geophysics*, **71**, K1–K8. 33, 79

Bradford, J. & Harper, J. (2005). Wave field migration as a tool for estimating spatially continuous radar velocity and water content in glaciers. *Geophysical Research Letters*, **32**, L08502. 32, 78

Bradford, J., Johnson, C., Brosten, T., McNamara, J. & Gooseff, M. (2007). Imaging thermal stratigraphy in freshwater lakes using georadar. *Geophysical Research Letters*, **34**. 102

Bradford, J., Nichols, J., Mikesell, D. & J., H. (2009). Continuous multi-fold acquisition and analysis of ground-penetrating radar data for improved characterization of glacier structure and water content. *Annals of Glaciology*, **50**, 1–9. 33, 78

Brosten, T., Bradford, J., McNamara, J., Gooseff, M., Zarnetske, J., Bowden, W. & Johnston, E. (2009). *Multi-offset GPR methods for hyporheic zone investigations. Near Surface Geophysics*, **7**, 247–257. 15, 78

Butler, D. (2005). *Near-surface geophysics*. Society of Exploration Geophysicists Tulsa. 2

Cai, J. & McMechan, G. (1999). 2-d ray-based tomography for velocity, layer shape, and attenuation from GPR data. *Geophysics*, **64**, 1579–1593. 33, 78

Cassiani, G., Strobbia, C. & Gallotti, L. (2004). Vertical radar profiles for the characterization of deep vadose zones. *Vadose Zone Journal*, **3**, 1093–1105. 32, 53, 56, 80

Cassiani, G., Fusi, N., Susanni, D. & Deiana, R. (2008). Vertical radar profiles for the assessment of landfill capping effectiveness. *Near Surface Geophysics*, **6**, 133–142. 53, 80

Cassidy, N. (2009a). Electrical and magnetic properties of rocks, soils and fluids (ed. h. jol h.). *Ground penetrating radar: theory and applications*, **Elsevier**, 41–72. 67, 69

Cassidy, N. (2009b). Ground penetrating radar data processing, modeling and analysis. *Ground penetrating radar: theory and applications, (ed. H. Jol)*, 141–172. 31, 52, 78

Chen, J., Hubbard, S. & Rubin, Y. (2001). Estimating hydraulic conductivity at the south oyster site from geophysical tomographic data using bayesian techniques based on the normal regression model. *Water Resources Research*, **37**, 1603–1613. 57

Clement, W.P. & Barrash, W. (2006). Crosshole radar tomography in a fluvial aquifer near Boise, Idaho. *Journal of Environmental and Engineering Geophysics*, **11**, 171–184. 53, 80

Clement, W.P. & Knoll, M. (2006). Traveltime inversion of vertical radar profiles. *Geophysics*, **71**, 3, K67–K76. 56

Clerk, M. & Kennedy, J. (2002). The particle swarm-explosion, stability, and convergence in a multidimensional complex space. *IEEE Transactions on Evolutionary Computation*, **6**, 58–73. 38

Conyers, L. & Goodman, D. (1997). *Ground-penetrating radar*. AltaMira Press. 1

Daniels, D.J. (2004). *Ground penetrating radar*. Institution of Electrical Engineers. 2

Davis, J. & Annan, A. (1989). Ground-penetrating radar for high-resolution mapping of soil and rock stratigraphy. *Geophysical prospecting*, **37**, 531–551. 31, 52, 70

Day-Lewis, F.D., Singha, K. & Binley, A. (2005). Applying petrophysical models to radar traveltime and electrical resistivity tomograms: Resolution-dependent limitations. *Journal of Geophysical Research*, **110**, B08206. 53, 80

Dix, C. (1955). Seismic velocities from surface measurements. *Geophysics*, **20**, 68–86. 34

Eberhart, R. & Shi, Y. (2000). Comparing inertia weights and constriction factors in particle swarm optimization. *Proceedings of the IEEE Congress on Evolutionary Computation*, 84–88. 38

Endres, A.L. & Knight, R.J. (1992). A theoretical assessment of the effect of microscopic fluid distribution on the dielectric response of partially saturated rocks. *Geophysical Prospecting*, **40**, 307–324. 68

Fernández Martínez, J., García Gonzalo, E., Fernández Álvarez, J., Kuzma, H. & Menéndez Pérez, C. (2010). PSO: A powerful algorithm to solve geophysical inverse problems-application to a 1D-DC resistivity case. *Journal of Applied Geophysics*, **71**, 13–25. 36, 39, 57, 79

Fliesbach, T. (2008). *Electrodynamik*. Spektrum, 5th edn. 2

Fomel, S. (1997a). A variational formulation of the fast marching eikonal solver. *Stanford Exploration Project*, **95**, 127–147. 11, 33, 35, 38, 79

Fomel, S. (1997b). A variational formulation of the fast marching eikonal solver. *SEP-95: Stanford Exploration Project*, 127–147. 56

Galagedara, L., Parkin, G., Redman, J., Von Bertoldi, P. & Endres, A. (2005a). Field studies of the gpr ground wave method for estimating soil water content during irrigation and drainage. *Journal of Hydrology*, **301**, 182–197. 15, 79

Galagedara, L., Redman, J., Parkin, G., Annan, A. & Endres, A. (2005b). Numerical modeling of GPR to determine the direct ground wave sampling depth. *Vadose Zone Journal*, **4**, 1096–1106. 16, 79

Gerwin, W., Raab, T., Biemelt, D., Bens, O. & Hüttl, R.F. (2009). The artificial water catchment 'chicken creek' as an observatory for critical zone processes and structures. *Hydrology and Earth System Sciences Discussions*, **6**, 1769–1795. 101

Gerwin, W., Schaaf, W., Biemelt, D., Elmer, M., Maurer, T. & Schneider, A. (2010). The artificial catchment Hühnerwasser (chicken creek): Construction and initial properties. *Ecosystem development*, **1**, 4–50. 101

Giannopoulos, A. (2005). Modelling ground penetrating radar by gprmax. *Construction and building materials*, **19**, 755–762. 4, 5, 7, 79

Gloaguen, E., Marcotte, D., Giroux, D., Dubreuil-Boisclair, C., Chouteau, M. & Aubertin, M. (2007). Stochastic borehole radar velocity and attenuation tomographies using cokriging and cosimulation. *Journal of Applied Geophysics*, **62**, 141–157. 53, 80

Greaves, R., Lesmes, D., Lee, J. & Toksöz, M. (1996). Velocity variations and water content estimated from multioffset, ground penetrating radar. *Geophysics*, **61**, 683–695. 11, 15, 31, 33, 78, 79, 80

Grote, K., Crist, T. & Nickel, C. (2010). Experimental estimation of the GPR ground wave sampling depth. *Water Resources Resources*, **46**, W10520. 15, 16, 79

Hajnal, Z. & Sereda, I. (1981). Maximum uncertainty of interval velocity estimates. *Geophysics*, **46**, 1543–1547. 32, 79

Hamann, G., Tronicke, J., Steelman, C. & Endres, A. (2013). Spectral velocity analysis for determination of ground wave velocities and their uncertainties in multi-offset GPR data. *Near Surface Geophysics*, **11**, 167–176. 31, 52, 57, 80

Hammon, W.S., Zeng, X., Corbeanu, R.M. & McMechan, G.A. (2002). Estimation of the spatial distribution of fluid permeability from surface and tomographic GPR data and core, with a 2-D example from the Ferron Sandstone, Utah. *Geophysics*, **67**, 1505–1515. 53, 80

Harbi., H. & McMechan, G.A. (2011). Modeling 3D porosity and permeability from GPR data in the Ellenburger Dolomite, central Texas. *Geophysics*, **76**, J35–J46. 53, 80

Hardage, B.A. (2000). *Handbook of Geophysical Exploration*, chap. Vertical Seismic Profiling, Principles. Pergamon. 54, 58

Harper, J. & Bradford, J. (2003). Snow stratigraphy over a uniform depositional surface: spatial variability and measurement tools. *Cold Regions Science and Technology*, **37**, 289–298. 32, 79

Hearst, J.R., Nelson, P.H. & Paillett, F.L. (2000). *A handbook for geophysicists, geologists and engineers*, chap. Well logging for physical properties. John Wiley & Sons. 60

Heimovaara, T., Bouten, W. & Verstraten, J. (1994). Frequency domain analysis of time-domain reflectometry waveforms: 2. a four component complex dielectric mixing model for soils. *Water Resources Research*. 15, 80

Hillel, D. (1998). *Environmental soil physics: Fundamentals, applications, and environmental considerations*. Academic press. 2, 14, 78

Holliger, K., Musil, M. & Maurer, H.R. (2001). Ray-based amplitude tomography for crosshole georadar data: a numerical assessment. *Journal of Applied Geophysics*, **47**, 285–298. 58

Huisman, J., Sperl, J., Bouten, W. & Berstraten, J. (2001). Soil water content measurements at different scales: accuracy of time domain reflectometry and ground penetrating radar. *Journal of Hydrology*, **245**, 48–58. 15, 79

Huisman, J., Snepvangers, J., Bouten, W. & Heuvelink, G. (2003). Monitoring temporal development of spatial soil water content variation: comparison of ground penetrating radar and time domain reflectometry. *Vadose Zone Journal*, **2**, 519–529. 14, 15, 79, 80

Huisman, J., Hubbard, S., J.D., R. & Annan, A. (2003a). Measuring soil water content with ground penetrating radar: a review. *Vadose Zone Journal*, **2**, 476–491. 31, 80

Igel, J., Günther, T. & Kuntzer, M. (2013). Ground-penetrating radar insight into a coastal aquifer: the freshwater lens of Borkum Island. *Hydrology and Earth System Sciences*, **17**, 519–531. 53, 80

Jackson, J. & Fox, R. (1999). Classical electrodynamics. *American Journal of Physics*, 237–513. 2

Jackson, P., Smith, D., Taylor, T. & Stanford, P. (1978). Resistivity-porosity-particle shape relationships for marine sands. *Geophysics*, **43**, 1250–1268. 78

Jacob, R. & Hermance, J. (2004). Assessing the precision of GPR velocity and vertical two-way travel time estimates. *Journal of Environmental and Engineering Geophysics*, **9**, 143–153. 32, 79

Jacobsen, O. & Schjønning, P. (1993). A laboratory calibration of time domain reflectometry for soil water measurement including effects of bulk density and texture. *Journal of Hydrology*, **151**, 147–157. 78

Jol, H. (2009a). Electromagnetic principles of ground penetrating radar. **1**. 1

Jol, H.M. (2009b). *Ground penetrating radar theory and applications*. Elsevier Science Limited. 2, 8, 31, 52, 78

Kennedy, J. & Eberhart, R. (1995). Particle swarm optimization. *Proceedings of the IEEE International Joint Conference on Neural Networks*, **4**, 1942–1948. 11, 36, 56, 79

Kleeberg, A., Herzog, C., Jordan, S. & Hupfer, M. (2010). *Initial development of the artificial catchment 'Chicken Creek' - monitoring program and survey 2005-2008, Ecosystem Development, 2*. Schaaf, W., Biemelt, D. und Hüttl, R.F. 102

Knight, R. & Endres, A. (2005). An introduction to rock physics principles for near-surface geophysics. *Near-surface geophysics*, 31–70. 9

Knödel, K., Krummel, H. & Lange, G. (2006). *Handbuch Zur Erkundung Des Untergrundes Von Deponien und Altlasten: Band 3: Geophysik*, vol. 3. Springer. 1, 2

Knoll, M. (1996). A petrophysical basis for ground penetrating radar and very early time electromagnetics: Electrical properties of sandy-clay mixtures. 9, 53, 80

Knoll, M.D. & Clement, W.P. (1999). Vertical radar profiling to determine dielectric constant, water content and porosity values at well locations. *11th Annual Symposium on the Application of Geophysics to Engineering and Environmental Problems*, **Environmental and Engineering Geophysical Society**, 821–830. 53, 67, 80

Lehner, G. (2006). *Elektromagnetische Feldtheorie: für Ingenieure und Physiker*. Springer DE. 2

Leparoux, D., Gibert, D. & P., C. (2001). Adaptation of prestack migration to multi-offset ground-penetrating radar (GPR) data. *Geophysical Prospecting*, **49**, 374–386. 33, 79

Levin, F. (1971). Apparent velocity from dipping interface reflections. *Geophysics*, **36**, 510–516. 32, 79

Linder, S., Paasche, H., Tronicke, J., Niederleithinger, E. & Vienken, T. (2010). Zonal cooperative inversion of crosshole p-wave, s-wave, and georadar traveltime data sets. *Journal of Applied Geophysics*, **72**, 254–262. 45, 59

Loeffler, O. & Bano, M. (2004). Ground penetrating radar measurements in a controlled vadose zone: influence of the water content:. *Vadose Zone Journal*, **3**, 1082–1092. 68

Looms, M.C., Jensen, K.H., Binley, A. & Nielsen, L. (2008). Monitoring unsaturated flow and transport using cross-borehole geophysical methods. *Vadose Zone Journal*, **7**, 227–237. 53, 80

Lunne, T., Robertson, P. & Powell, J. (1997). *Cone Penetration Testing in Practice*. Blackie Academic and Professional. 49

Malicki, M., Plagge, R. & Roth, C. (1996). Improving the calibration of dielectric TDR soil moisture determination taking into account the solid soil. *European Journal of Soil Science*, **47**, 357–366. 78

Maxwell, J. (1891). *A Treatise on Electricity and Magnetism*. London. 2

Menke, W. (1989). *Geophysical data analysis: discrete inverse theory*, vol. 45. Elsevier. 33

Miller, R., Bradford, J. & Holliger, K. (2010). *Advances in Near-surface Seismology and Ground-penetrating Radar*. 1

Monteiro Santos, F. (2010). Inversion of self-potential of idealized bodies' anomalies using particle swarm optimization. *Computers & Geosciences*, **36**, 1185–1190. 36, 57, 79

Moore, J., Pälli, A., Ludwig, F., Blatter, H., Jania, J., Gadek, B., Glowacki, P., Mochnacki, D. & Isaksson, E. (1999). High-resolution hydrothermal structure of hansbreen,spitsbergen, mapped by ground-penetrating radar. *Journal of Glaciology*, **45**, 524–532. 32, 78

Moorman, B. & Michel, F. (1997). Bathymetric mapping and sub-bottom profiling through lake ice with ground-penetrating radar. *Journal of Paleolimnology*, **18**, 61–73. 102

Moret, G.J.M., Clement, W.P., Knoll, M.D. & Barrash, W. (2004). Vsp traveltime inversion: Near-surface issues. *Geophysics*, **69**, 345–351. 56

Murray, T., Stuart, G.W., Fry, M., Gamble, N.H. & Crabtree, M.D. (2000). Englacial water distribution in a temperate glacier from surface and borehole radar velocity analysis. *Journal of Glaciology*, **46**, 389–398. 53, 80

Olsson, O., Falk, L., Forslund, O., Lundmark, L. & Sandberg, E. (1992). Borehole radar applied to the characterization of hydraulically conductive fracture zones in crystalline ROCK1. *Geophysical Prospecting*, **40**, 109–142. 5, 57, 58

Paasche, H., Tronicke, K.G.A.G., J.and Holliger & Maurer, H.R. (2006). Integration of diverse physical-property models: Subsurface zonation and petrophysical parameter estimation based on fuzzy c-means cluster analyses. *Geophysics*, **71, no. 3**, H33–H44. 57

Peterson, J.E. (2001). Pre-inversion corrections and analysis of radar tomographic data. *Journal of Environmental and Engineering Geophysics*, **6**, 1–18. 57, 58

Pipan, M., Baradello, L., Forte, E., Prizzon, A. & Finetti, I. (1999). 2D and 3D processing and interpretation of multi-fold ground penetrating radar data: a case history from an archaeological site. *Journal of Applied Geophysics*, **41**, 271–292. 33, 78

Poli, R. (2008). Analysis of the publications on the applications of particle swarm optimization. *Journal of Artificial Evolution and Applications*, **2008**, 1–10. 36, 79

Porsani, J. & Sauck, W. (2007). Ground-penetrating radar profiles over multiple steel tanks: Artifact removal through effective data processing. *Geophysics*, **72**, J77–J83. 32, 78

Pringle, J., Westerman, A., Clark, J., Guest, J., Ferguson, R. & Gardiner, A. (2003). *Ground penetrating radar in sediments*, vol. 211, chap. The use of vertical radar profiling (VRP) in GPR surveys of ancient sedimentary strata, 225–246. Geological Society, Special Publications, London. 53, 80

Rector, J.W. & Washbourne, J.K. (1994). Characterization of resolution and uniqueness in crosswell direct-arrival traveltime tomography using the fourier projection slice theorem. *Geophysics*, **59**, 1642–1649. 53, 80

Roth, C., Malicki, M. & Plagge, R. (1992). Empirical evaluation of the relationship between soil dielectric constant and volumetric water content as the basis for calibrating soil moisture measurements by TDR. *Journal of Soil Science*, **43**, 1–13. 9

Sambuelli, L. & Bava, S. (2011). Case study: A GPR survey on a morainic lake in northern Italy for bathymetry, water volume and sediment characterization. *Journal of Applied Geophysics*. 102

Schmelzbach, C., Tronicke, J. & Dietrich, P. (2011). Three-dimensional hydrostratigraphic models from ground-penetrating radar and direct-push data. *Journal of Hydrology*, **398**, 235–245. 11, 45, 52, 53, 59, 78, 80

Schneider, A., Gerke, H., Maurer, T., Seifert, S., Nenov, R. & Hüttl, R. (2011). Evaluation of remotely-sensed DEMs and modification based on plausibility rules and initial sediment budgets of an artificially-created catchment. *Earth Surface Processes and Landforms*. 102, 103

Schön, J.H. (1998). *Fundamentals and Principles of Petrophysics*, chap. Physical Properties of Rocks. Pergamon. 60

Schuster, G.T., Johnson, D.P. & Trentman, D.J. (1988). Numerical verification and extension of an analytic generalized inverse for common-depth-point and vertical seismic profile traveltime equations. *Geophysics*, **53**, 326–333. 56

Sen, M. & Stoffa, P. (1995). Global optimization methods in geophysical. 33, 39, 40, 56, 64

Sen, P. (1984). Grain shape effects on dielectric and electrical properties of rocks. *Geophysics*, **49**, 586–587. 10, 78

Sethian, J. (1996). A fast marching level set method for monotonically advancing fronts. *In: Proceedings of the National Academy of Sciences of USA*, **93**, 1591–1595. 11, 33, 35, 38, 56, 79

Sethian, J. & Popovici, A. (1999). 3-d traveltime computation using the fast marching method. *Geophysics*, **64**, 516–523. 11, 33, 35, 38, 56, 79

Shaw, R. & Srivastava, S. (2007). Particle swarm optimization: A new tool to invert geophysical data. *Geophysics*, **72**, F75–F83. 36, 57, 79

Sheriff, R. & Geldart, L. (1999). Exploration seismology, 2nd edition. 17

Spillmann, T., Maurer, H.R., Willenberg, H., Evans, K.F., Heincke, B. & Green, A.G. (2006). Characterization of an unstable rock mass based on bore-hole logs and diverse borehole radar data. *Journal of Applied Geophysics*, **61**, 16–38. 53, 80

Steelman, C. & Endres, A. (2009). Evolution of high-frequency ground-penetrating radar direct ground wave propagation during thin frozen soil layer development. *Cold Regions Science and Technology*, **57**, 116–122. 24

Steelman, C. & Endres, A. (2010). An examination of direct ground wave soil moisture monitoring over an annual cycle of soil conditions. *Water Resources Research*, **46**, W11533. 11, 16, 22, 24, 26, 79

Steelman, C. & Endres, A. (2011). Comparison of petrophysical relationships for soil moisture estimation using GPR ground waves. *Vadose Zone Journal*, **10**, 270–285. 8, 15, 67

Steelman, C. & Endres, A. (2012). Assessing vertical soil moisture dynamics using multi-frequency GPR common-midpoint soundings. *Journal of Hydrology*, **436-437**, 51–66. 31, 80

Stolt, R. (1978). Migration by fourier transform. *Geophysics*, **43**, 23–48. 103

Taner, M. & Koehler, F. (1969). Velocity spectra-digital computer derivation and applications of velocity functions. *Geophysics*, **34**, 859–881. 32, 34, 79

Tarantola, A. (2005). Inverse problem theory and methods for model parameter estimation. *Society for Industrial and Applied Mathematics.*. 43

Tillard, S. & Dubois, J. (1995). Analysis of GPR data: wave propagation velocity determination. *Journal of Applied Geophysics*, **33**, 77–91. 31, 32, 52, 78, 79

Topp, G., Davis, J. & Annan, A. (1980). Electromagnetic determination of soil water content: Measurements in coaxial transmission lines. *Water Resources Research*, **16**, 574–582. 9, 15, 67, 68, 80

Tronicke, J. & Knoll, M. (2005). Vertical radar profiling: Influence of survey geometry on first arrival traveltimes and amplitudes. *Journal of Applied Geophysics*, **57**, 179–191. 32, 54, 55, 56, 58, 60, 62

Tronicke, J., Dietrich, P., U., W. & E., A. (2002). Integrating GPR and crosshole radar tomography: A validation experiment in braided stream deposits. *Geophysics*, **67**, 1495–1504. 32, 53, 79

Tronicke, J., Holliger, K., W., B. & M.D., K. (2004). Multivariate analysis of crosshole georadar velocity and attenuation tomograms for aquifer zonation. *Water Resources Research*, **40**, WO1519. 31, 53, 57, 58, 80

Tronicke, J., Paasche, H. & Böniger, U. (2012). Crosshole traveltime tomography using particle swarm optimization: a near-surface field example. *Geophysics*, **77**, R19–R32. 36, 37, 39, 45, 57, 59, 79

Turesson, A. (2007). Comparative analysis of the multi-offset ground-penetrating radar and shear-wave reflection methods. *Journal of Environmental & Engineering Geophysics*, **12(2)**, 163–171. 15, 78

Valle, S., Zanzi, L. & Rocca, F. (1999). Radar tomography for NDT: Comparison of techniques. *Journal of Applied Geophysics*, **41**, 259–269. 57

van der Kruk, J., Steelman, C., Endres, A. & Vereecken, H. (2009). Dispersion inversion of electromagnetic pulse propagation within freezing and thawing soil waveguides. *Geophysical Research Letters*, **36**, L18503. 16, 26, 79

Van Overmeeren, R., Sariowan, S. & Gehrels, J. (1997). Ground penetrating radar for determining volumetric soil water content; results of comparative measurements at two test sites. *Journal of Hydrology*, **197**, 316–338. 31, 80

Vereecken, H., Binley, A., Cassiani, G., Revil, A. & Titov, K. (2006). *Applied hydrogeophysics*. Springer. 1, 14

Vienken, T. & Dietrich, P. (2011). Field evaluation of methods for determining hydraulic conductivity from grain size data. *Journal of Hydrology*, **400**, 58–71. 72

Vignoli, G., Deiana, R. & Cassiani, G. (2012). Focused inversion of vertical radar profile (VRP) traveltime data. *Geophysics*, **77**, H9–H18. 53, 56, 80

Vukovic, M. & Soro, A. (1992). Determination of hydraulic conductivity of porous media from grain-size composition. *Water Resources Publications*. 68, 69

Wharton, R.N., R. P.and Rau & Best, D.L. (1980). Electromagnetic propagation logging: Advances in technique and interpretation. In *Pap. 9267. Annual Technical Conference, SPE.*. 9, 67

Wilken, D. & Rabbel, W. (2012). On the application of particle swarm optimization strategies on scholte-wave inversion. *Geophysical Journal International*, **190**, 580–594. 37, 57, 79

Yi, M. & Endres, A. (2006). Application of f-k analysis to multi-offset gpr direct wave measurements for water content: a modeling study. In *Proceedings of the 11th international conference on ground penetrating radar, paper hyd.2.*. 16, 79

Yilmaz, Ö. (2001). *Seismic data analysis: processing, inversion, and interpretation of seismic data*. 10, SEG Books. 5, 16, 17, 31, 32, 34, 79

Zelt, C. & Smith, R. (1992). Seismic traveltime inversion for 2-D crustal velocity structure. *Geophysical Journal International*, **108**, 16–34. 33, 79

Zhou, B. & Fullagar, P.K. (2001). Delineation of sulphide ore-zones by borehole radar tomography at Hellyer Mine, Australia. *Journal of Applied Geophysics*, **47**, 261–269. 57, 58

Zhou, H. & Sato, M. (2000). Application of vertical radar profiling technique to Sendai Castle. *Geophysics*, **65**, 533–539. 5, 53, 80

Appendix: Estimating sedimentary deposition in an artificial lake using 3D ground-penetrating radar

Göran Hamann, Jens Tronicke and Micheal Weber
18th European Meeting on Environmental and Engineering Geophysics EAGE-NSG, 2012

Introduction

In 2004 and 2005, the artificial water catchment Hühnerwasser ("chicken creek") was established in the post-mining landscape of the opencast mine Welzow-Süd in Germany Gerwin *et al.* [2010]. Until today, numerous research groups use this catchment as a field laboratory to study structures and processes of the initial development phase of an ecosystem. The catchment covers an area of ca. 6 ha with maximum elevation changes around 15 m (Fig. 1) and has been shaped to form an inclined basin. The uppermost subsurface layers are ca. 3-4 m thick, consist of sandy material and are underlain by a ca. 1-2 m thick clay layer acting as a hydrological barrier. In the lowermost part of the site, an artificial lake covering an area of ca. 0.6 ha and an original maximum depth of about three meters was established to study the water balance of the entire system including surface runoff and subsurface discharge Gerwin *et al.* [2009]. Furthermore, investigating

and monitoring lake-bottom topography is used to quantify the sedimentary input and, thus, to study fluvial erosion processes in the catchment Schneider *et al.* [2011]. In 2008, first attempts to quantify the sedimentary input have been made by point measurements of water depths using rods and shallow drillings Kleeberg *et al.* [2010] observing a maximum lake depth of ca. 2.4 m and a sedimentation rate of ca. 1280 m^3 in the period of August 2005 to October 2008.
Ground-penetrating radar (GPR) is a widley used geophysical technique to explore sedimentary environments also underneath water bodies [e.g., Bradford *et al.*, 2007; Moorman & Michel, 1997; Sambuelli & Bava, 2011]. In this study, we use 3D GPR surveying across the artificial lake in the Hühnerwasser catchment to investigate lake bottom topography and sedimentary structures beneath the water body. Using a repetitive surveying strategy (i.e., two 3D surveys recorded in two consecutive winters), we also evaluate the potential of the GPR technique to monitor the evolution of sedimentary structures in detail. In the following, we first describe our 3D GPR data acquisition and processing strategy. Then, we discuss the processed GPR images and interpret them in terms of the relevant sedimentary structures. This also includes a comparison between the two 3D data sets collected at different times including a GPR derived estimate of sedimentation rate.

Data acquisition and processing

In February 2011 and 2012, we have collected two 3D GPR data sets across the artificial lake at the *Hühnerwasser* catchment to study the feasibility of the GPR technique to image subsurface structures relevant for analyzing fluvial erosion processes within the catchment. During our surveys, the lake was frozen (ice thickness ca. 10 cm) and, thus, we were able to employ a conventional GPR surveying approach based on cart-mounted 100 MHz antennae and a combination of the GPR instrument with a self-tracking total station (Böniger & Tronicke [2010]), to achieve accurate positioning of measured traces. We applied a standard processing flow including de-wow filtering, time-zero corrections, band-pass filtering, exponential amplitude scaling and migration. After applying this processing sequence, the raw data were stacked and interpolated on to a 0.125 ×

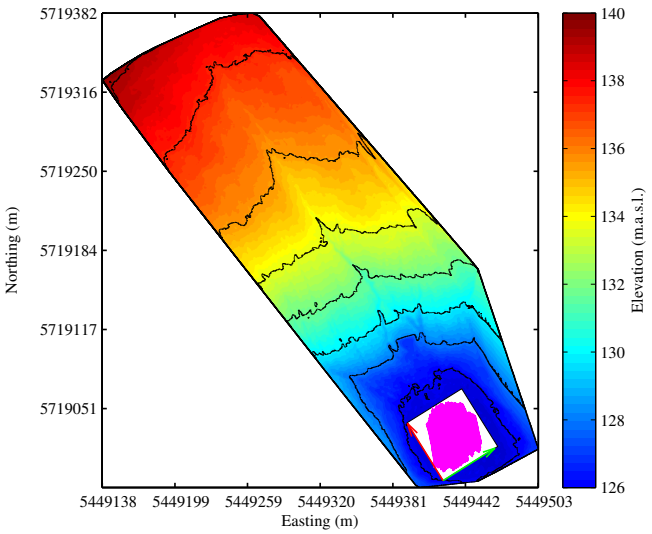

Figure 1: Digital elevation model from Schneider *et al.* [2011] of the *Hühnerwasser* catchment illustrating erosion structures three years after construction phase. Magenta area indicates the survey from 2012. Vectors represent the grid applied to GPR survey, green in northeast direction (inline) and red in northwest direction (crossline).

0.125 m grid (indicated with vectors and white rectangel in Fig. 1) using a natural neighbor based interpolation scheme. For migration, we used a 3D Stolt migration algorythm [Stolt, 1978] with a constant velocity of 0.04 m/ns. This velocity value has been chosen because it provided the best migration results for our data sets. The migrated data are shown in Fig. 2 and Fig. 3. Fig. 2 illustrates a part of the migrated data in terms of a crossline section extracted from the data cube recorded in 2012. Some minor migration artifacts are visible (e.g., between 0 and 10 m distance between 0 and 100 ns). These artifacts are related to minor velocity errors introduced by not explicitely considering the 2D nature of the velocity field (ice, water body, saturated sediments). However, for the purpose of this study migration using a constant velocity of 0.04 m/ns is sufficient as it provides well-focused images of the target sedimentary structures. To visualize the lake bottom the picked traveltimes of events reflected at the lake bottom were interpolated (Fig. 4). The difference of the traveltimes between two different years was used to calculate the sedimentation rate and to achive a map showing quantities in wave traveltimes proportional to spatial lake depth changes from sedimentation (Fig. 5).

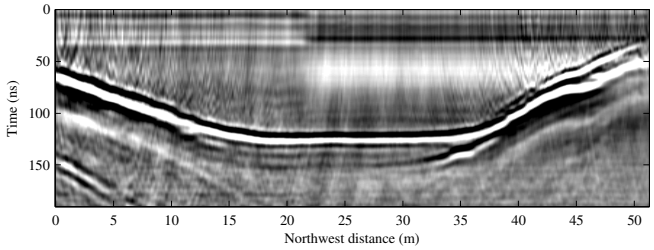

Figure 2: Typical crossline section extracted from the GPR data cube recorded in 2012. Clear reflections are visible from the lake bottom, from sedimentary structures beneath the lake bottom (e.g., at 20-35 m and ca. 140 ns) and in the area of the alluvial fan (between 60-100 ns and 40-50 m). Amplitudes changes at 21 m caused by different ice conditions during two days of measurements.

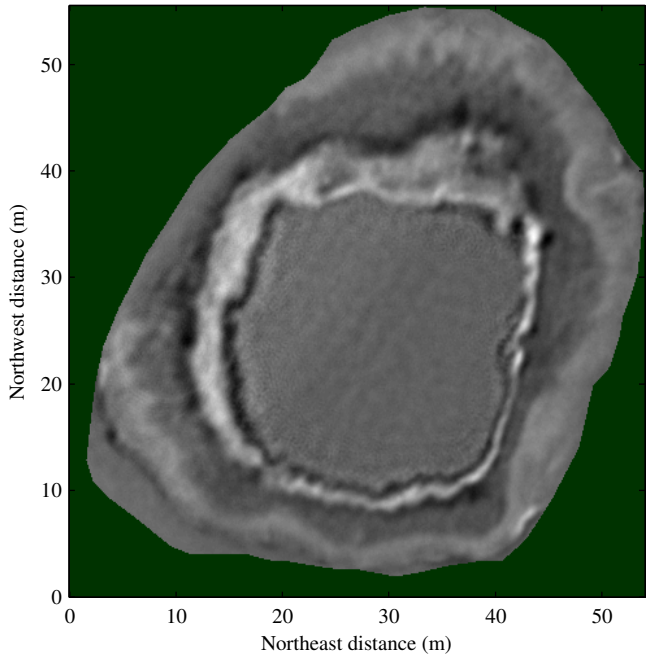

Figure 3: Migrated timeslice at 100 ns extracted from the GPR data cube recorded in 2012. Showing a circular structure with a diameter of ca.30 m from reflections at the lake bottom and structures beneath the lake bottom in the area of the alluvial fan (between 20-40 m northeast distance and 35-45 m northwest distance).

Results and interpretation

The final processed data are visualized in Fig. 2 and Fig. 3. In Fig. 2, we show a crossline section extracted at 29 m of the northeast distance from the data cube from 2012, with clear reflections from the lake bottom, from sedimentary structures beneath the lake bottom (e.g., at 20-35 m and ca. 140 ns) and in the area of the alluvial fan (between 60-100 ns and 40-50 m). This data were collected within

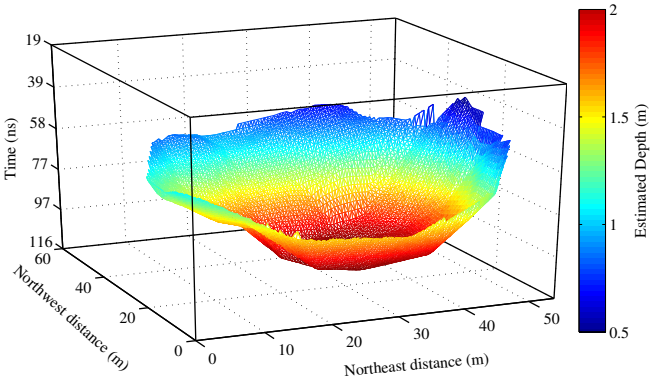

Figure 4: Picked and triangulated traveltimes of events reflected at the lake bottom of the Hühnerwasser lake in 2011. Colorcoding represents lake bottom dephts calculated with a constant velocity of 0.038 m/ns.

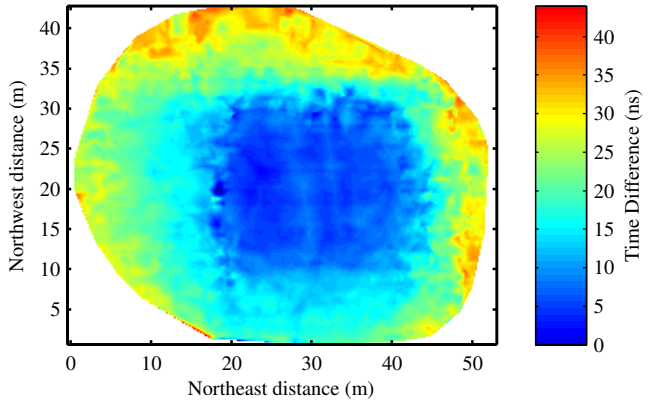

Figure 5: Map of sedimentation rate derived from the difference of picked and triangulated traveltimes of events reflected at the lake bottom of the Hühnerwasser lake from the years of 2011 and 2012. Highest sedimentation rates are visible at the alluvial fan (at 35 m of northwest distance).

two days under different snow and ice condition (freezing/melting), what results in amplitude changes and different ringing character (at ca. 21 m and at times up to ca. 45 ns). A time slice extracted at 100 ns from the cube recorded in 2012 is shown in Fig. 3 . This slice indicates that the lake bottom reflection can be followed throughout the entire data cube (circular structure with a diameter of ca. 30 m). The structure visible around 20-40 m northeast distance and around 40 m northwest distance is interpreted as alluvial fan deposits associated with fluvial sedimentary input into the lake.

In addition to detailed 3D images of sedimentary structures, our GPR data allow to quantify the amount of deposited material and sedimentation rates, respec-

tively, by picking the lake bottom reflection in both 3D data sets and subtracting the resulting traveltime maps from each other. In Fig. 4, the picked and triangulated traveltimes of events reflected at lake bottom are shown exemplary for the year 2011. Fig. 5 shows the traveltime differences (2011 minus 2012). Minimum differences are observed in the central part of the lake whereas maximum values are found at edges of the lake, especially, in the northwest part of the lake, where maximum sedimentary input associated with fluvial erosion from the catchment occures. Assuming a velocity of 0.038 m/ns, we estimate a difference of ca. 0.8 m between the lake bottom in 2011 and 2012. In a similar manner, we can estimate the total volume of sediment input for one year to be ca. 394 m^3.

Conclusions

We have collected 3D GPR data across the artificial lake at the Hühnerwasser field laboratory. Our GPR data provide detailed images of the lake bottom topography and sedimentary structures beneath the water body. Furthermore, repetitive surveys in February 2011 and 2012 can be used to visualize changes in lake bottom topography associated with sedimentary input. Our findings are in reasonable agreement with previous studies based on point measurements and, thus, we conclude that the GPR technique is capable to provide important data to study and understand erosional processes at the Hühnerwasser field laboratory.